Capillary phenomena and instabilities in driven miscible liquids and soft solids

Alessandro Carbonaro

THÈSE POUR OBTENIR LE GRADE DE DOCTEUR DE L'UNIVERSITE DE MONTPELLIER

En Physique

École doctorale : Information, Structures, Systèmes

Unité de recherche : Laboratoire Charles Coulomb

Capillary phenomena and instabilities in driven miscible liquids and soft solids

Présentée par Alessandro Carbonaro

Le 19/11/2020

Sous la direction de Domenico Truzzolillo et Luca Cipelletti

Devant le jury composé de

Domenico Truzzolillo, Chargé de Recherche, CNRS	Directeur de thèse
Lucio Isa, Professeur, ETH Zurich	Rapporteur
Isabelle Cantat, Professeur, Université de Rennes 1	Rapportrice
Howard A. Stone, Professeur, Princeton University	Examinateur
Laura Casanellas Vilageliu, Maître de Conférence, Université de Montpellier	Examinatrice
Manouk Abkarian, Directeur de Recherche, CNRS	Président du jury
Luca Cipelletti, Professeur, Université de Montpellier	Co-directeur de thèse, Invité

UNIVERSITÉ DE MONTPELLIER

Contents

Chapter 1

Introduction

"God made the bulk; the surface was invented by the devil."

W. Pauli

There is a place in Belgrade where the Danube makes a turn, merging its waters with those of the Sava river. The difference in colour between the two balkan rivers gave birth to the story that their waters do not actually mix, and that the two rivers flow one close to the other instead of becoming one: the separation between the green waters of the Danube and the darker ones of the Sava is visible long after their meeting point. Setting aside the legendary aspect of this tale, how would it be possible for water not to mix with water? And what actually happens when two fluids mix?

When two different liquids are brought in contact, the compositional change characterising their interface locally induces a stress anisotropy, with the result that the molecules feel a net force opposing the formation of new interface. This general description captures the character of surface tension between immiscible fluids. Indeed, we all have the experience that some liquids mix well while some others tend to remain separate, such as oil and vinegar when one wants to dress a salad. We also know that this changes when mustard is added to the two liquids, allowing the cook to form an emulsion. Mustard acts as an emulsifier for the two normally immiscible fluids by reducing the interfacial tension between oil and vinegar. This is an everyday-life example of the importance of interfacial tension, which constitutes an indispensable background for understanding phenomena ranging from salad dressing to soap bubbles, oil recovery, biological life, and many others.

By contrast, capillary phenomena between miscible fluids constitute a much less explored and settled topic. From a thermodynamic point of view, when two fluids interdiffuse interfacial tension cannot exist, since the equilibrium state of the system corresponds to a homogeneous mixture. Nevertheless, as early as in 1901, the physicist and mathematician D. Korteweg postulated that the out-of-equilibrium compositional change in the interfacial region could induce stresses acting as an equilibrium interfacial tension [1], before diffusion brings the system to its final mixed state. In the case of the Danube and Sava rivers, such transient *Korteweg stresses* should affect the region immediately after the confluence, arising from compositional differences in the water. But does such an *effective interfacial*

Figure 1.1: The confluence of the Danube and the Sava rivers in Belgrade, as seen from the Belgrade fortress of Kalemegdan.

tension actually exist, and what would be the difference with respect to the conventional thermodynamic quantity that we usually refer to as to the "interfacial tension"? These questions are not settled yet and are still actively investigated. Furthermore, their interest is not purely academic. In spite of its transient character, the presence of an effective interfacial tension (EIT) would be important for many practical applications, from multiphase polymer flows during industrial processes [2], to the motion of magma in the Earth's mantle in geophysics [3], where gradients in minerals concentration or in temperature exist.

In this thesis we present an experimental work aiming at measuring and understanding the effective interfacial tension between miscible molecular fluids. It is thus important to start with an overview of the state of the art.

1.1 Interfacial tension at equilibrium

Interfacial tension is a well understood quantity for interfaces between two different phases or substances at equilibrium, such as oil and vinegar in our salad dressing example. It is generally treated in literature following one of two possible approaches, namely a mechanic or a thermodynamic approach. Here we briefly recall the two approaches, in order to introduce the subtle difference between interfacial tension and surface free energy.

According to Shuttleworth [4], the mechanical description of surface tension dates back to 1629, when Cabeo first introduced it [5]. It can be simply understood by considering a water and soap film suspended between two walls of a frame. If one of the walls can move, an external force is necessary to maintain it fixed, since the soap film has the tendency to reduce its area, pulling on the wall itself. In this framework, the surface tension of the film is simply given by the force $\vec{\mathbf{F}}$ per unit length which is required to maintain the frame wall

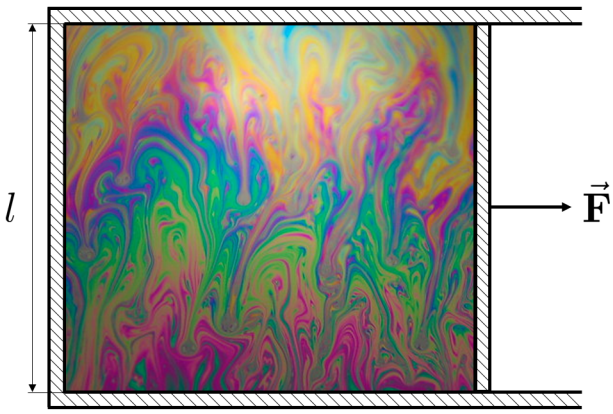

Figure 1.2: Scheme of a soap film suspended in a frame, whose right wall can slide. A force $\vec{\mathbf{F}}$ is required to maintain the wall fixed, balancing the one applied by the film.

in its position:

$$\Gamma = \frac{\left|\vec{\mathbf{F}}\right|}{l}\,, \tag{1.1}$$

where l is the length of the wall (Fig. 1.2). The film behaves indeed as if it was an elastic membrane under the action of a tension, the surface tension. The same happens for the interface between two immiscible liquids, which, due to the different molecular interactions between molecules of the two species, opposes deformations. From a thermodynamic perspective, one could think to describe this phenomenon by considering that an energy is associated to the interface, and define the interfacial tension as the free energy per unit area. This last assumption would be correct for simple immiscible liquids and for the soap film if the motion of the wall is much slower than the time needed for soap molecules to diffuse to the surface, but it is not correct in general. Indeed, following Shuttleworth [4], it is worth stressing that interfacial tension and interfacial energy are in general different. As we will detail it in Sec. 6.2, the difference between the two quantities can be immediately understood for the case of crystals. In particular, the surface free energy F_s is the work per unit area required to create an interface in a state of mechanical equilibrium, such as in cleaving a crystal. On the contrary, following the mechanical definition of Eq. 1.1, interfacial tension is the tangential stress per unit area needed to deform the surface (or to prevent retraction, such as for the soap film of Fig. 1.2). If we imagine stretching the surface of a crystal, the interatomic distance will change, introducing a dependence of the surface energy on the deformation state of the material. Taking into account this dependence, the relation between surface tension and surface free energy is given by [4]:

$$\Gamma = F_s + A\left(\frac{\partial F_s}{\partial A}\right)\,. \tag{1.2}$$

Equation 1.2 will be important in Chapter 4 and in Sec. 6.2, and it highlights that even in the equilibrium case care is needed to properly define interfacial tension.

1.2 Non-equilibrium Effective Interfacial Tension: state of the art

Korteweg postulated the existence of an effective interfacial tension between miscible fluids from a mechanical perspective [1], but one can recast his conclusions in thermodynamic terms following Cahn and Hilliard [6]. Given the non-equilibrium character of miscible interfaces, standard equilibrium thermodynamics cannot be applied. Nevertheless, one can assume local equilibrium and expand the free energy F of the system in powers of the concentration gradient $\nabla\varphi$, with φ the spatial-dependent concentration of one of the two fluids:

$$F = \int_V f(\varphi, \nabla\varphi)dv = \int_V \{f_0(\varphi) + \frac{1}{2}k(\varphi)(\nabla\varphi)^2 + \mathcal{O}[(\nabla\varphi)^4]\}dv\,. \tag{1.3}$$

Note that here F is the total free energy of the system, $f_0(\varphi)$ is the free energy per unit volume of a homogeneous mixture with concentration φ, and V the volume of the system. k is the Korteweg parameter, which can in principle depend on the concentration. It is worth noting that the expansion cannot contain odd power terms, since the latter would change sign upon inversion of the coordinate system. The effective interfacial tension Γ_e is then defined as

$$\Gamma_e = \frac{\partial F}{\partial A}\,. \tag{1.4}$$

We will discuss in Sec. 6.2 the consequence of a possible dependence of the surface-specific free energy on the surface area itself. The simple case of a flat interface in the xy plane yields [6]:

$$\Gamma_e = \int_{-\frac{\delta}{2}}^{+\frac{\delta}{2}} k(\varphi)(\nabla\varphi)^2 dz\,, \tag{1.5}$$

where δ is the interface thickness; the factor $\frac{1}{2}$ in Eq. 1.3 disappears taking into account the contribution of $f_0(\varphi)$ [6]. When the concentration gradient is small enough to be approximated by a linear function across the interface, and neglecting the dependence of k on φ, Eq. 1.5 can be written as

$$\Gamma_e = k\frac{(\Delta\varphi)^2}{\delta}\,. \tag{1.6}$$

Here $\Delta\varphi = \varphi_1 - \varphi_2$ is the concentration difference between the two bulk fluids. Clearly, the EIT decreases over time and becomes negligible as diffusion smears out the interface. Nevertheless, it can be important at short times and for slowly diffusing systems, such as in the case of polymers or complex fluids [7].

In recent years experimental and theoretical effort has been devoted to the study of Korteweg stresses [7–15]. On the experimental side, the most recent works leverage on the analysis of the shape of threads and drops [10–12], on light scattering experiments characterizing capillary waves [13, 14], and on hydrodynamic instabilities [7, 15]. All these experimental techniques have been applied to a variety of systems, notably miscible fluids both close and far from a critical point, and complex fluids. Despite this effort, there is no general consensus on capillary phenomena in the miscible case, as we shall detail below.

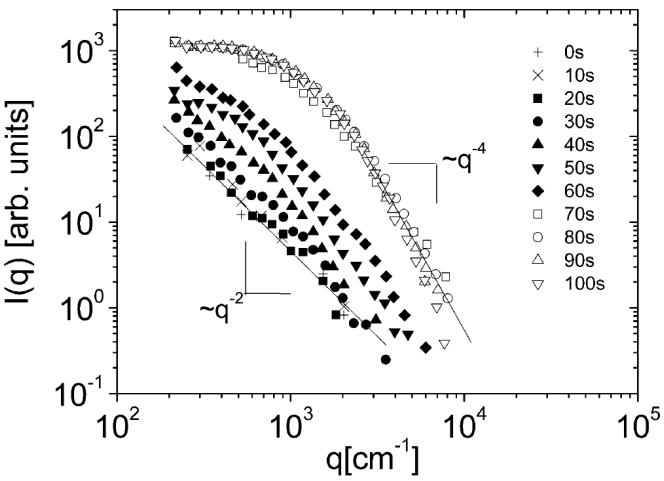

Figure 1.3: Scattered intensity as a function of the scattering vector, measured over time after a critical mixture of aniline and cyclohexane was brought in the coexistence region. Adapted from Ref. [16].

Among the works on Korteweg stresses, many of the most important ones investigated the case of near-critical mixtures. The reason for this is that such mixtures offer a simple way to form a well-defined interface between the two phases when brought to the two-phase region of their phase diagram. The two well-separated phases can subsequently be made miscible by means of a sudden change in temperature. This is a way to attain miscibility, but still finely controlling the initial state of the system. Cicuta and coworkers [13] used this approach in a paramount work investigating the EIT between near-critical mixtures. In particular, they measured by means of light scattering the non-equilibrium fluctuations at the interface between the two phases of a near-critical aniline-cyclohexane mixture. They considered separately the contributions to the small-angle scattered intensity coming from the interfacial (i.e. capillary waves) and bulk fluctuations. These two contributions can indeed be resolved, since they give rise to two different dependencies of the intensity on the scattering vector q ($I \sim q^{-2}$ and $I \sim q^{-4}$, respectively). Remarkably, the authors observed that shortly after the mixture was brought in the coexistence region the scattered intensity was still dominated by the interfacial contribution, which faded with time as diffusion smeared out the interface. Figure 1.3 reports the time evolution of the scattered intensity as a function of q, shortly after the system was brought in the coexistence region: over time, the intensity signal evolves from a q^{-2} to a q^{-4}-dependence, demonstrating that at short time capillary waves are present at the interface.

A different set of measurements on near-critical mixtures were performed by Pojman and coworkers by means of Spinning Drop Tensiometry (SDT) [10]. As we will detail in Sec. 2.1, a spinning drop tensiometer consists in a glass capillary filled with liquid, which is set in rotation after the injection of a drop of a second, less dense liquid. Inspecting the shape of the drop at a given angular velocity allows for measuring the interfacial tension

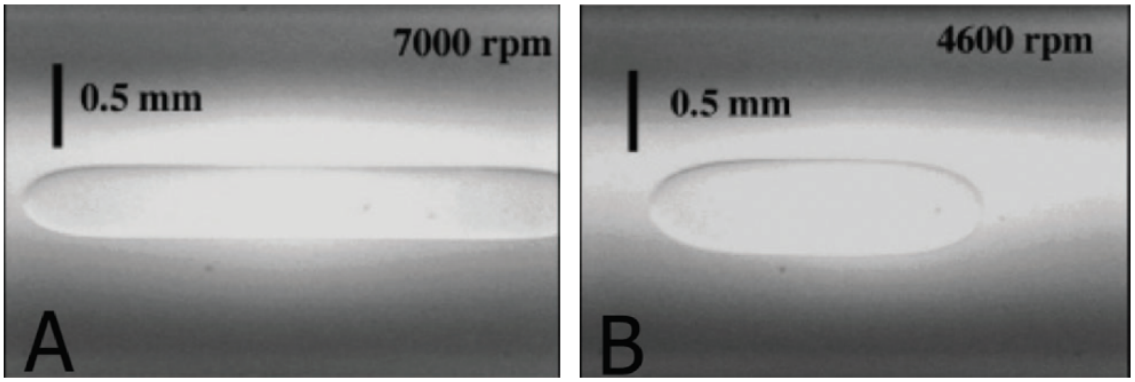

Figure 1.4: Retraction of an IBA-rich drop spinning in a miscible IBA-poor background upon reduction of the rotational speed. Adapted from Ref. [16].

between the two fluids. This technique has gained popularity in recent years [10, 17, 18] due to its ease of use and because it is suitable to measure particularly low values of the interfacial tensions (10^{-3} - 10^{-2} mN/m [19,20]). Pojman and coworkers [10] exploited SDT to perform a series of very accurate experiments on the EIT between the two miscible phases of a near-critical water/isobutyric acid (IBA) mixture. One of the main results of their work is the fact that the spinning drop retracted upon reduction of the rotational speed of the capillary, as shown in Fig. 1.4. This is a clear demonstration that a positive EIT existed between the two phases. Furthermore, the analysis of the drop shape allowed for measuring a value of 0.03 ± 0.02 mN/m, with the large uncertainty on the EIT coming from the one on the imposed temperature jump. Despite the difficulty in extracting a precise value for the tension between the two fluids, the drop retraction showed in this work is a remarkable evidence for the presence of an EIT. Together with the work by Cicuta et al. [13], the work by the group of Pojman [10] showed the existence of an EIT for near-critical mixtures. On the other hand, the topic is less settled for the case of miscible fluids far from a critical point, such as water and ethanol or glycerol.

The better understood case of non-critical, miscible liquids is that of complex fluids, such as colloidal suspensions in contact with their solvent, or polymer suspensions. A thorough investigation of the EIT in such a case was provided by Truzzolillo and coworkers [7], who exploited hydrodynamic instabilities to characterize capillary phenomena at miscible interfaces. In particular, they investigated the development of the Saffman-Taylor instability at miscible interfaces. This "viscous fingering" instability arises when a less dense fluid is injected in a more dense one. This is often achieved with a radial geometry in a Hele-Shaw cell. In such experiments, the more viscous fluid is contained between two close plates, and the less viscous one in injected from a small orifice, and expands radially. Interestingly, the interface between the two fluids can become unstable and develop a finger-like pattern, with the number of fingers depending on the viscosities of the two fluids, on the injection rate and on the interfacial tension. Figure 1.5a shows an example of such an unstable pattern. The analysis of the fingering pattern allowed for measuring the effective interfacial tension between miscible complex fluids, namely colloidal suspensions displaced by their own sol-

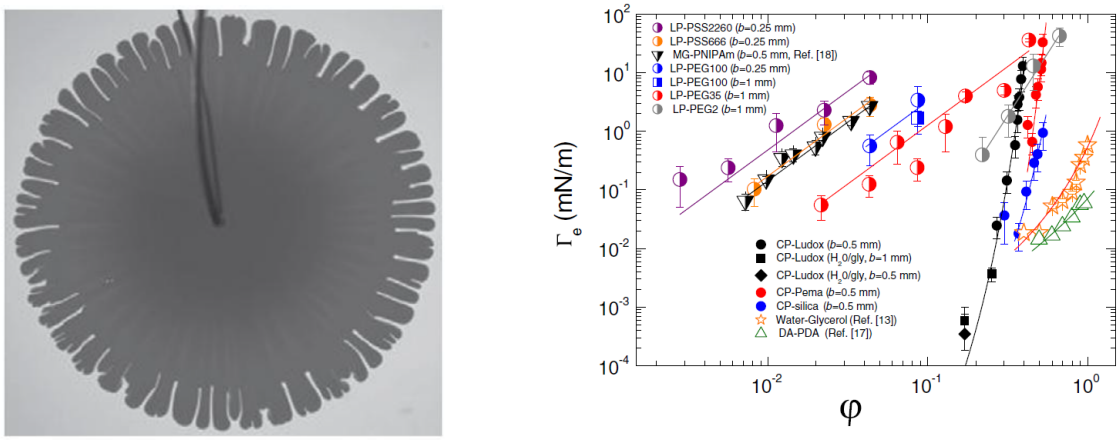

(a) (b)

Figure 1.5: (a) Image of the Saffman-Taylor instability in a radial geometry. Adapted from Ref. [21]. (b) Effective interfacial tension between water and glycerol, and DA-PDA (empty symbols), measured with spinning drop tensiometry, between colloidal suspensions and their solvent (full symbols) and for solutions of linear polymers (semifilled symbols), measured from viscous fingering experiments. Solid lines are power-law fits with an exponent 2 for the case of polymer solutions, and fits of the refined model presented in [7] in all other cases. Adapted from Ref. [7].

vent and solutions of linear polymers [7]. Furthermore, by varying the concentration of the colloidal particles and polymer in the samples, the authors investigated the dependence of Korteweg stresses on the concentration φ. Their results are reported in Fig. 1.5b, where the authors show that the EIT increases with φ^2 in the case of solutions of linear polymers, in agreement with Eq. 1.6, where Γ_e depends linearly on $(\Delta\varphi)^2$. On the contrary, colloidal suspensions in contact with their solvent do not show the same dependence, and additional terms are needed in Eq. 1.5 to account for the concentration dependence.

Regardless of the exact dependence of the EIT on φ, the work by Truzzolillo and coworkers provides clear evidence of the existence of Korteweg stresses in complex fluids. It is worth stressing that for such a system diffusion can be extremely slow, depending on the properties of the colloidal particles ans polymer suspensions. Hence, Korteweg stresses remain important for several seconds after the two fluids are brought into contact, before diffusion smears out the interface. On the other hand, for simple miscible fluids Korteweg stresses are expected to decay much faster, making their experimental characterisation much more complicated. As a consequence, for simple miscible liquids the value and the very existence of the EIT is still debated, and no general consensus has been reached.

The analysis of hydrodynamic instabilities such as the Saffman-Taylor one would in principle provide an interesting tool to investigate simple fluids, since the instability often develops milliseconds after the liquids are brought into contact. Indeed, the study of hydrodynamic instabilities has gained importance in recent years as a tool to investigate fluid-fluid interfaces and the interfacial tension in particular. Stability analysis constitutes a fundamental and general problem of fluid mechanics, but since interfacial tension plays a big role in determining stability, it has become an established way to indirectly characterize interfacial phenomena. Maybe the clearest example of the intimate relation between interfacial tension and stability is the Rayleigh-Plateau instability [22, 23]. In Rayleigh-Plateau instability, interfacial tension causes a fluid jet to break in smaller droplets in order to reduce its surface area and the associated free energy cost. Such a phenomenon can be observed in a variety of practical examples, from ink jet printing to the dripping of water from a faucet. In other cases, interfacial tension can contribute to stabilizing the interface, such as in the Faraday instability, in which two stratified fluid layers are subject to an oscillatory forcing and can develop ripples at their interface [24, 25]. Regardless of the particular character of capillary phenomena in the instability under consideration, it is clear that the importance of surface stresses on stability makes this an interesting way to investigate interfacial tension in the first place. Furthermore, when the two fluid layers are miscible, the study of hydrodynamic instabilities offers the possibility to set the degree of mixing: in the case of parallel coflow of two fluids in a channel, for instance, the degree of mixing depends on the distance travelled downstream. By observing the stability of such an interface always at the same position, one can rule out the time dependency of the interface due to diffusion.

Despite the promising aspects of the study of hydrodynamic instabilities for simple fluids interfaces, Paterson [26] and more recently Bischofberger and coworkers [27] investigated the EIT between water and glycerol by means of viscous fingering, but could not measure any effect of Korteweg stresses, asserting that the instability pattern was dominated by viscous

dissipation. Remarkably, spinning drop tensiometry measurements on the same system yielded a value of 0.58 mN/m [28]. However, the latter experiments suffer from different flaws which we will try to elucidate later [11]. This example shows that literature data on such simple miscible fluids are conflicting, sometimes even by the same authors [28, 29]. Furthermore, Zoltowski et al. [17] performed a series of SDT experiments on drops of dodecyl acrilate in poly(dodecyl acrilate), but they could not clearly measure an EIT. While for complex fluids interfaces can remain sharp over time, in simple miscible liquids diffusion constitutes a major difficulty in measuring the EIT, which is expected to decay very rapidly over time. This is the general picture in which our work settles. In this framework, this thesis intends to shed light on Korteweg stresses between simple miscible liquids, and propose a new experimental method to characterise the EIT.

There is a further aspect worth discussing before tackling the problem of EIT between simple miscible liquids. The absence of consensus in the literature on the nature of Korteweg stresses [27–29] stems mainly from the plethora of different experimental results obtained with various techniques. Therefore, it is not clear under which conditions the EIT behaves as an equilibrium interfacial tension, and it becomes crucial to tackle this problem from different viewpoints. As an example, one still unsettled question is whether or not Korteweg stresses are present in absence of an imposed deformation of the interface, or only when the latter is, for instance, stretched. We will try to discuss this problem in Sec. 6.2. On the experimental side, exploiting different techniques is of fundamental importance for understanding the intimate nature of Korteweg stresses. Therefore, in this work we will study Korteweg stresses from two different perspectives. In particular, we will try to reduce the confusion on the subject by proposing a new method to measure extremely low values of interfacial tension using a spinning drop tensiometer, and will introduce the study of the stability in miscible viscosity-stratified coflow as a second, independent tool to tackle the problem.

1.3 Outline of the thesis

The two main parts of this thesis reflect the two approaches chosen to study the EIT. Since for simple miscible fluids diffusion represents a major problem when performing static experiments, we first characterize the possibility of carrying out dynamical measurements in a spinning drop tensiometer. In particular, instead of looking at the equilibrium shapes of drops at a given rotational frequency, we measure their elongation dynamics after a sudden jump in angular velocity. The dynamics of drops spinning in both miscible and immiscible backgrounds are presented in Chapter 2 and in [11]. Remarkably, drops spinning in a miscible background do not always maintain an ellipsoidal shape, and for sufficiently low interfacial tension they develop a so-called “dumbbell” shape, with two large heads connected by a thinner central body. In Chapter 3 we exploit the time evolution of such shapes to measure ultra-low values of interfacial tensions in SDT experiments. In particular, we analyze the prototypical case of water and glycerol, solving the controversy arising from conflicting literature values for the EIT in this system [30]. To conclude our spinning drop tensiometry analysis, in Chapter 4 we demonstrate that SDT can have a much wider application range than liquid drops, and that it can be used to measure simultaneously the

interfacial tension and the elastic modulus of soft elastic beads. In particular, we discuss the difference between interfacial tension and surface free energy for the case of amorphous materials, namely polyacrylamide beads in contact with fluorinated oil [31].

As already stated, the lack of understanding of Korteweg stresses requires different experimental techniques to be employed. In Chapter 5 we discuss from a theoretical and experimental point of view the stability of parallel channel coflow in a microfluidic device, which can be used to study the EIT from a different perspective.

Finally, Chapter 6 collects some general conclusions and perspectives of this work, notably discussing the importance of an imposed deformation of the interface on the presence of Korteweg stresses, and the conditions under which the latter behave alike an equilibrium interfacial tension. On the experimental side, one possibility to investigate the effect of the EIT in absence of imposed deformation would be to perform drop retraction experiments in SDT, where the rotation of the capillary is suddenly arrested. However, such an experiment cannot be performed on Earth due to buoyancy, which would quickly bring the drop out of the axis of the SDT capillary after the rotation is stopped, hampering the measurement of the drop dynamics. Therefore, in Sec. 6.2 we discuss a series of experiments to be performed in microgravity conditions during the parabolic flight campaign organized by CNES (Centre Nationale d'Études Spatiales) at the end of September 2020, to investigate the intimate nature of Korteweg stresses.

Part I

Spinning Drop Tensiometry

Chapter 2

Spinning drops dynamics in miscible and immiscible environments

Liquid droplets represent a model system to study phenomena whose relevant length scales range from laboratory to geophysical ones. Nevertheless, their dynamics under different conditions are not always well established, especially when the interfacial tension Γ can be neglected. In the present chapter, we present our results on the elongation dynamics of spinning drops which are subject to a centripetal forcing, both in presence and absence of Γ, recently published in [11].

2.1 Spinning drop tensiometry

Over the years, several experimental techniques were developed to measure interfacial tension. Some examples are the Wilhelmy plate technique [32], the Langmuir trough [33], and the analysis of the shape of pendant [34] and sessile drops [35]. All these techniques differ for their sensitivity, presence or absence of an imposed external field, and relevance to specific systems, such as liquid-vapour, liquid-solid or liquid-liquid interfaces. In particular for the investigation of the latter, one specific technique which allows measuring very low values of Γ (10^{-3} - 10^{-2} mN/m [19, 20]) through a fine control of the forcing imposed on the interface is spinning drop tensiometry (SDT). This is a technique which was initially conceived by Vonnegut [36] to measure interfacial tension between immiscible fluids, and was later developed by Princen et al. [37], Torza et al. [38], and Joseph et al. [39]. In an SDT experiment, a drop of a given fluid is injected in a denser background fluid in a cylindrical capillary. When the capillary is set in rotation, the drop elongates on the axis of the capillary due to the centripetal forcing, and the observation of its shape allows measuring the interfacial tension between the background and the drop fluid.

Two types of experiments are possible with an SDT apparatus. The first and most commonly used one leverages the original idea by Vonnegut, and implies measuring the

equilibrium shape that the drop attains at a given rotational speed, when spinning in an immiscible background. In such case, the equilibrium shape of the drop is simply dictated by a balance of the centripetal forcing and surface tension: in order to obtain the equilibrium shape of the drop, it is sufficient to compute the total energy of the drop and minimize it. When the drop is sufficiently elongated, it can be approximately described as a cylinder of radius r and length l, with hemispherical endcaps (Fig. 2.1). The surface contribution to

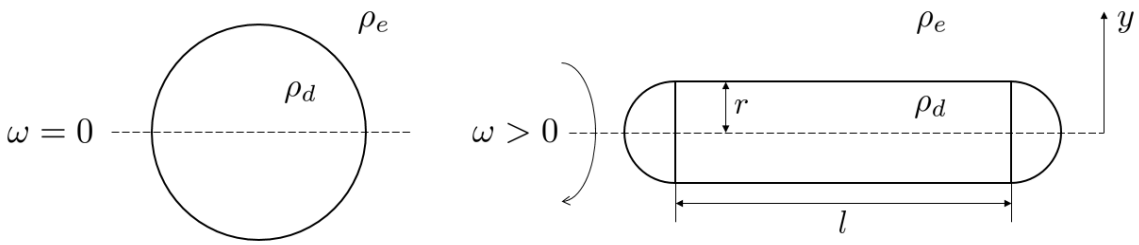

Figure 2.1: Scheme of the principle of spinning drop tensiometry: when the capillary is spun, the drop elongates on the rotation axis.

the energy of the drop is then

$$E_s = \Gamma(2\pi r l + 4\pi r^2)\,, \tag{2.1}$$

where Γ is the interfacial tension between the drop and the background fluid. By contrast, the energy of the drop associated to rotation can be obtained by integrating over the drop volume the pressure difference $p = \frac{\Delta\rho\omega^2 y^2}{2}$ between the drop and the external fluid:

$$E_r = \int_V p dv = \frac{\Delta\rho\omega^2}{2}\int_0^r y^2\left[2\pi l y + 4\pi y\sqrt{r^2 - y^2}\right] dy\,, \tag{2.2}$$

where $\Delta\rho = \rho_e - \rho_d$ is the density difference between the external background fluid and the drop fluid and ω is the rotational speed. By differentiating the total energy $E = E_s + E_r$ with respect to r, one obtains for the interfacial tension:

$$\Gamma = \frac{\Delta\rho\omega^2 r^3}{4}\left(1 + \frac{2r}{3l}\right)\,. \tag{2.3}$$

Equation 2.3 defines the drop shape at equilibrium, and allows measuring Γ from the known values of ω, $\Delta\rho$, l and r. In the case $l \gg r$, it is sufficient to measure only the drop radius, and not its length, from the direct visualization of the spinning drop, since Eq. 2.3 becomes:

$$\Gamma = \frac{\Delta\rho\omega^2 r^3}{4}\,. \tag{2.4}$$

Equation 2.4 is called the Vonnegut equation [36]. Even though one single experiment at a given rotational speed would be sufficient to measure the interfacial tension, it is more accurate to measure the equilibrium radius of the drop in a series of experiments at various

ω in order to extract Γ from the linear fit of $r^2(\omega^{-3})$. On the contrary, if the drop is not sufficiently elongated ($l \sim r$), Eq. 2.4 does not hold, and the interfacial tension has to be inferred from a fit of the curved surface of the drop by means of the Young-Laplace equation [40].

A second strategy to perform an SDT experiment aiming at measuring Γ involves the characterization of the drop dymamics after a sudden jump of the imposed centripetal forcing. This approach is much less explored though it offers one major advantage when systems with ultralow interfacial tension are concerned: it does not require attaining a stationary state. For this reason, it is viable even in the case of miscible fluids, for which the equilibrium state is a homogeneous mixture of the fluids in the capillary. This method was initially introduced by Patterson et al. [41] and theoretically investigated by Hu and Joseph [42], and Stone and Bush [43], and is the one that we adopt in [11]. In the case of drops spinning in an immiscible reservoir, the elongation (or retraction) dynamics follow an exponential decay as they go towards the equilibrium shape dictated by the value of the rotational speed after the jump, with a characteristic time given by [43]:

$$\tau = \frac{\eta_e a}{\Gamma} f(\lambda)\,. \tag{2.5}$$

Here η_e is the viscosity of the background fluid, a the radius of the undeformed (e.g. at rest) drop, $\lambda = \eta_d/\eta_e$ the viscosity contrast, with η_d the viscosity of the drop fluid, and $f(\lambda) = \frac{(3+2\lambda)(16+19\lambda)}{40(1+\lambda)}$. Even though Eq. 2.5 was derived for the limit of small deformations of nearly-spherical drops, we show in [11] that it captures well the dynamics of more elongated drops as well.

On the other hand, drops that are miscible with their background and for which surface tension is negligible elongate indefinitely following a power law dynamics, as we shall show in [11] for one specific couple of fluids with a low concentration mismatch (namely, a drop of 5% wt/wt H_2O-glycerol mixture spinning in a reservoir of pure glycerol). In particular, in the case of low viscosity ratios between the drop and background fluids, the elongation dynamics of drops with negligible interfacial tension follows:

$$l(t) \simeq \left(\frac{\Delta\rho\omega^2 V^{3/2}}{\eta_e}\right)^{2/5} t^{2/5}\,, \tag{2.6}$$

where V is the drop volume. No stationary state is reached, and the drops elongate indefinitely.

2.1.1 Experimental set-up

All SDT experiments have been performed with a Krüss spinning drop tensiometer, as detailed in [11, 30], at rates of rotation sufficiently high so that buoyancy could be neglected. Indeed, when the capillary is not spun sufficiently rapidly, gravity can push the drop out of the rotation axis, hampering the correct measurement of the drop shape. Currie and Van Nieuwkoop [44] characterised experimentally the critical rotation speed ω_c for which buoyancy becomes negligible. For the case of a butanol drop spinning in water, they observed SDT measurements to be accurate for angular velocities $\omega > \omega_c = 5000$ rpm. Currie

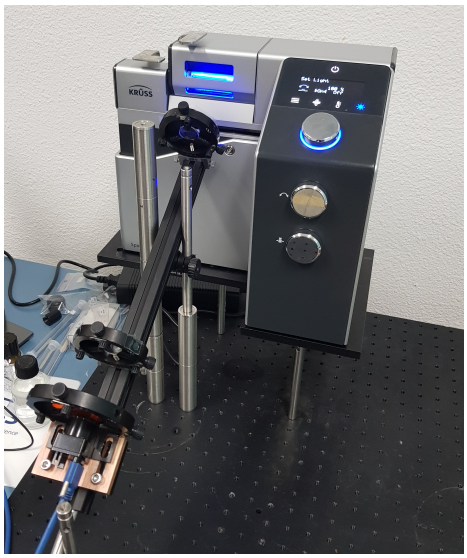

Figure 2.2: Image of the SDT apparatus used for the experiments, with the system of cylindrical lenses used as an objective assembled in front of the SDT rotation chamber.

and Van Nieuwkoop developed a hydrodynamic model which allowed them rationalizing the effect of buoyancy [44]. They found that the drop displacement from the rotation axis can be written as:

$$d = \frac{2\sqrt{2}}{3} \frac{g}{\omega^2} \frac{\Delta\rho}{\rho} , \tag{2.7}$$

where g is the gravitational acceleration, ρ the density of the background fluid, and $\Delta\rho$ the density difference between the drop and the background fluids. Moreover, d is independent on the drop volume. For a drop of butanol in water, this leads to a displacement from the axis of about 5 µm at 5000 rpm. Therefore, in order to set ourselves in the same operating conditions of Currie and Van Nieuwkoop, to estimate a critical angular velocity ω_c when performing our SDT experiments we calculate the rotation speed that corresponds to a displacement of $d = 5\,\mu\text{m}$ using Eq. 2.7. It is worth noting that the 5 µm threshold is also lower than the experimental resolution with which we determine the drop radius. For the case of a drop of pure water spinning in pure glycerol, $\omega_c \simeq 6000$ rpm.

Consequently, all experiments were performed with rates of rotation ranging from 6000 rpm to 15000 rpm, accurate to 1%. Temperature was set to 25.0 ± 0.5°C using a temperature-controlled air flow. For low values of interfacial tension, drops in an SDT experiment become very elongated and slender. Therefore, we use as an objective a system of two cylindrical lenses sharing the same optical axis to increase the imaging resolution. As detailed in [11, 30], the lenses expand the field of view in the vertical direction y and compress it in the horizontal direction x, with magnification $M_y = 0.3$ and $M_x = 3.36$, respectively. The different vertical and horizontal magnification allows us to follow the dynamics of very elongated drops, while increasing at the same time the resolution in the vertical direction, so as to be sensitive to small variations of the drop radius.

The SDT is equipped with a blue LED for illumination, with a dominant wavelength of 469 nm, and a CMOS camera for imaging. When the drop and the background fluids are immiscible, the former is easily visualized thanks to the difference in refractive index between the two fluids. On the contrary, for miscible drops the refractive index difference is not sufficient to unambiguously determine the drop boundary. Therefore, when performing experiments on miscible fluids we dissolved fluorescein in the drop fluid, at a concentration of 0.2 % wt/wt. Fluorescein strongly absorbs at the wavelength of the illuminating blue LED, thus allowing one to clearly visualize the dyed drops. For each experiment on miscible fluids, the drop was injected in the capillary, pre-filled with the background fluid, with a 1 µL syringe. Care was taken to avoid the presence of a tail of fluoresceinated drop fluid when the needle was extracted, by slightly pulling the syringe piston while removing the syringe to prevent the injection of additional fluid. The time between the drop injection and the beginning of rotation was about 10 - 15 s. By contrast, for experiments on immiscible fluids (silicone oil drops spinning in glycerol), the viscosity of the drop fluid was too high to allow injection. Consequently, a drop of silicone oil was directly deposited in the the capillary. The tensiometer capillary is closed on the two sides by a moving piston and a cap, respectively. In order to introduce silicone oil drops, we dipped the piston in silicone oil before inserting it in the capillary, which was then filled with glycerol. Subsequently, an isolated drop was obtained either exploiting viscous pinch off by slightly moving the piston with the capillary still open on the other side, or via Rayleigh-Plateau instability once the capillary was closed with the cap and spun in the tensiometer. After each experiment, both for miscible and immiscible fluids, the capillary was flushed and the background fluid replaced.

The possibility to clearly observe both miscible and immiscible drops and to follow their elongation dynamics up to very large aspect ratios allowed us to experimentally verify Eqs. (2.5-2.6). In particular, Eq. 2.5 was derived under the assumption of small deformations, but it proved to remain applicable over a much wider parameter range. On the contrary, when the interfacial tension between the drop and background fluids is negligible, no stationary state is attained. A more detailed discussion is presented in [11].

LANGMUIR Article
Cite This: *Langmuir* 2019, 35, 11330−11339 pubs.acs.org/Langmuir

Spinning Drop Dynamics in Miscible and Immiscible Environments

Alessandro Carbonaro, Luca Cipelletti, and Domenico Truzzolillo*

Laboratoire Charles Coulomb (L2C)UMR 5221, CNRS-Université de Montpellier, Montpellier, France

Supporting Information

ABSTRACT: We report on the extensional dynamics of spinning drops in miscible and immiscible background fluids following a rotational speed jump. Two radically different behaviors are observed. Drops in immiscible environments relax exponentially to their equilibrium shape, with a relaxation time that does not depend on the centrifugal force. We find an excellent quantitative agreement with the relaxation time predicted for quasi-spherical drops by Stone and Bush (*Q. Appl. Math.* **1996**, *54*, 551), while other models proposed in the literature fail to capture our data. By contrast, drops immersed in a miscible background fluid do not relax to a steady shape: they elongate indefinitely, their length following a power-law $l(t) \sim t^{2/5}$ in very good agreement with the dynamics predicted by Lister and Stone (*J. Fluid Mech.* **1996**, *317*, 275) for inviscid drops. Our results strongly suggest that low compositional gradients in miscible fluids do not give rise to an effective interfacial tension measurable by spinning drop tensiometry.

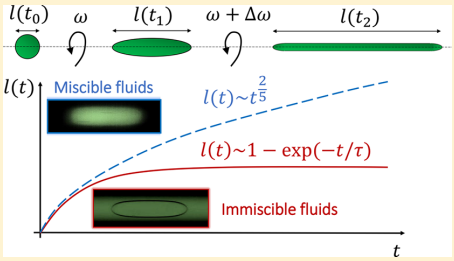

INTRODUCTION

Over the last century, liquid droplets have attracted the attention of physicists,[1] since they are fairly simple to study and control under different conditions, and because they represent a model system to understand the physics of phenomena occurring on different scales, ranging from laboratory[2,3] to astrophysical ones.[4] A droplet, for example, can spread out or ball up and spin depending on the interaction with the surface it lies on,[5] and its shape can be drastically modified by external fields[6] or when it is set in motion.[7,8] In particular, rotating droplets are among the most studied cases of liquids deformed by an external field as they are relevant in many situations: rotation plays a pivotal role on the structure and evolution of large-scale flows taking place in oceans, the atmosphere, and in the very body of planets and stars.[4,9]

Freely suspended droplets rotating at high speed tend to deform due to centrifugal forcing. Droplets change shape following a minimum energy principle, taking the lowest energy state for a given rotational frequency. This results in a series of nontrivial equilibrium shapes, strongly affected by surface tension.[3,10] The equilibrium shape of a weightless spinning droplet under the action of capillary forces was first discussed by Lord Rayleigh (1914).[1] He found a solution in which the bubble is a surface of revolution which meets the axis of rotation. If the angular speed is zero, then the bubble has a spherical form, while under the influence of rotation the sphere elongates along the rotation axis, and the oblateness increases upon increasing the angular velocity. However, more complicated shapes are obtained above a critical velocity that depends on interfacial tension and drop size, as shown by Hill et al.[3] for magnetically levitated water droplets. Magnetic levitation is indeed one appealing way to isolate and suspend single drops, however it is experimentally challenging, requiring the use of strong magnetic fields, especially for molecular fluids that display weak diamagnetic properties.

An alternative experimental configuration is that of a drop of liquid immersed in a denser background fluid, both confined in a horizontal cylindrical capillary. When the capillary is set in rotation, centrifugal forces confine the drop on the axis, avoiding any contact with the capillary wall. Furthermore, the shape of the drop is dictated by the balance between the centrifugal force and interfacial tension, allowing the latter to be measured. This is the principle of spinning drop tensiometry, originally introduced by Vonnegut[11] to measure interfacial tensions between immiscible fluids and further developed by Princen et al.,[12] Torza,[13] and Cayias et al.[14] Thanks to their work, spinning drop tensiometry (SDT) has become a versatile method, particularly well suited for measuring ultralow interfacial tensions (down to 10 μN/m). Such low tensions can occur, for example, in water−hydrocarbon−surfactant systems and are of considerable scientific interest as well as of great importance for industrial applications.

While the majority of works on spinning drops tensiometry focused on the equilibrium shape of the drops, several authors have characterized their relaxation after a jump in rotational speed, when suspended in an immiscible environment.[15−19] However, a general consensus on the mechanisms driving drop relaxation is still missing and different models have been proposed to capture the experimental behavior of Newtonian drops for both small and large deformations.[17−20] On the

Received: July 5, 2019
Revised: August 5, 2019
Published: August 12, 2019

DOI: 10.1021/acs.langmuir.9b02091
Langmuir 2019, 35, 11330−11339

experimental side, Joseph et al.[17] performed relaxation tests using polydimethylsiloxane ($\eta = 10^5$ mPa s) drops in glycerol, a system similar to that investigated in the present work, using a spinning drop tensiometer described in ref 21 at only one angular speed (ω = 3208 rpm). They found that the drop relaxes exponentially to its equilibrium shape. The same authors[17] reported a similar exponential relaxation for drops of polystyrene in poly(methyl methacrylate) (PMMA), drops of standard oil in water−glycerol mixtures[16] and drops of low-density polyethylene in PMMA.[22] In all cases, the value of the relaxation constant departed from that predicted theoretically by the same authors for largely deformed drops (see below eq 3). To summarize, several experiments suggest that largely deformed spinning drops in immiscible fluids relax exponentially toward an equilibrium shape after a jump of centrifugal forcing. However, a quantitative description of the relaxation time and a clear understanding of the relevant parameters that determine its value are still missing.

Research on drops in a miscible background fluid is less advanced. A full experimental characterization of drops showing pure extensional dynamics is missing: indeed, in most cases miscible drops also undergo a radial deformation due to secondary flows that set in a spinning capillary,[23] and this greatly complicates both measurements and modeling. P. Petitjeans[24] was the first to study fluids miscible in all proportions with SDT. In a series of measurements involving drops of water immersed in water−glycerol mixtures, he observed the stabilization of the drop radius after about 100 s for mixtures containing more than 40% glycerin mass fraction. By measuring the drop radius and using Vonnegut's formula (see below), he inferred the effective (transient) interfacial tension between the fluids. Similar measurements were performed by J. Pojman and co-workers,[25−28] who investigated the existence of an effective interfacial tension (EIT) between miscible fluids and discussed its importance, using (i) mixtures of Isobutyric acid and water close to their critical point and (ii) dodecyl acrylate drops in poly(dodecyl acrylate). They concluded that capillary forces are at work at the boundary between these fluids and quantified the EIT, again using Vonnegut's theory.

An important assumption in refs 24 and 26 is the fact that the drop reaches a quasi-equilibrium state or at least a steady state under rotation. Unfortunately, in these works the temporal evolution of the drop length is not reported: monitoring it would allow one to unambiguously ascertain the existence of such a steady state. Moreover, Pojman and co-workers observed the formation of dog-bone-shaped drops,[26] suggesting that secondary viscous flows may perturb the system. Such effect has been first pointed out by Manning et al.,[23] who discussed the role of secondary viscous flows in spinning drop tensiometry, underlining that they may lead to significant deviations with respect to the ideal case of Vonnegut's theory even for immiscible fluids, provided that the interfacial tensions is sufficiently low, $\Gamma \lesssim 10\ \mu$N/m.

In this work, we circumvent these difficulties and systematically investigate the temporal evolution of the drop length in SDT experiments that probe both immiscible and miscible systems, aiming in particular at detecting the existence of transient capillary forces at the interface between miscible fluids. Using a custom imaging setup, we follow the evolution of very elongated drops, assessing unambiguously whether or not a stationary state is reached. By focusing on the drop length, we furthermore avoid the complications inherent to the measurement of the drop radius, stemming from the curvature of the cylindrical capillary-air dioptre. Moreover, tracking the drop length of dyed viscous drops in miscible fluids, as those employed in this work, allows neglecting possible mismatches between the measured dye profiles and the concentration profiles of the drop fluid, arising from the difference in diffusivity between dye and fluid molecules. Indeed, the drop length evolves much faster than the width of the concentration gradient at the drop boundary, such that the measurement of the drop length is very precise. We compare the results of our experiments to existing theories for the stretching behavior of drops, for both the immiscible and miscible cases. We find that immiscible drops relax to their equilibrium shape exponentially, with a characteristic relaxation time τ independent of both the magnitude of the jump in ω and the equilibrium length of the drop. Our experiments therefore support the notion that for a given pair of fluids τ is an intrinsic property of the system, in excellent agreement with the prediction for small deformations of quasi-spherical drops by Stone and Bush.[20] The scenario for miscible fluids is strikingly different. We find that the drop shape never reaches a stationary state. Instead, for drops with a low concentration gradient with respect to the background fluid, the drop length increases indefinitely following asymptotically a power law: $l(t) \sim t^{2/5}$. The drop retains a cylindrical shape with spherical end-caps, indicating that in the experiments reported here radial deformations due to secondary flows are absent or negligible. The elongation behavior of our miscible drops is very well captured by a model originally proposed by Lister and Stone[29] for immiscible fluids, in the limit of vanishing surface tension and vanishing viscosity of the drop fluid ("bubble-like" dynamics).

The rest of the work is organized as follows. We briefly recall the theoretical background and the existent predictions for the elongational dynamics of spinning drops. We then present the materials employed and the experimental setup. Next, we discuss the results on the elongational dynamics for drops in an immiscible and miscible background fluid. In the last section, we make some concluding remarks and summarize the key results of this work.

Theoretical Background. Spinning drop tensiometry assumes the gyrostatic equilibrium of the drop, i.e., a state of uniform rotation in which every fluid element in a spinning rigid container is at rest with respect to the container wall. Consider a small drop of fluid A placed in a more dense fluid B contained in a cylindrical capillary. When the capillary is spun around its axis, the drop elongates axially and takes an ellipsoidal shape. At gyrostatic equilibrium, the normal component of the interfacial tension balances the hydrostatic pressure difference across the interface. If the drop length l (measured along the direction of the capillary axis) exceeds four times its equatorial diameter $2r$ (measured perpendicularly to the capillary axis), then the magnitude Γ of the interfacial tension can be calculated very simply from the drop radius r, the density difference $\Delta\rho = \rho_B - \rho_A$, and the angular velocity ω, via the well-known expression,

$$\Gamma = \frac{\Delta\rho\omega^2 r^3}{4} \tag{1}$$

first derived by Vonnegut.[11] Note that other methods of determining the interfacial tension based on the shape of a drop require a measurement of the two- or even three-dimensional profile of the drop and involve complicated

DOI: 10.1021/acs.langmuir.9b02091
Langmuir 2019, 35, 11330−11339

calculations, e.g., in the pendant drop method.[30] By contrast, the simplicity of Vonnegut's expression is one of the main advantages of the spinning-drop method.

Equation 1 holds at equilibrium, once a steady state has been reached. The time evolution of the drop upon a step change of ω has also been investigated. Theoretical models[17,19,20] and experiments,[15,16,18] both for immiscible fluids, suggest that drops relax exponentially toward their equilibrium state. Nevertheless, models developed for nearly spherical[20] or very elongated[19] drops predict qualitatively different expressions for the typical relaxation time τ. Stone and Bush[20] derived an exact solution for the fluid motion and time-dependent drop shape, provided that the following conditions are fulfilled: the drop remains nearly spherical, wall effects can be neglected, and fluid flows both inside and outside the drop are dominated by viscous effects. The last assumption allows the drop dynamics to be described in terms of centrifugally forced Stokes flows. In this case, the relaxation time after a rotation speed jump $\Delta\omega = |\omega_f - \omega_i|$ of a drop with viscosity η_d immersed in a surrounding liquid with viscosity η_e reads:

$$\tau = \frac{\eta_e a}{\Gamma} f(\lambda) \tag{2}$$

where a is the radius of the drop at rest, $\lambda = \eta_d/\eta_e$ the viscosity contrast, and $f(\lambda) = \frac{(3+2\lambda)(16+19\lambda)}{40(1+\lambda)}$ a dimensionless prefactor. The relaxation time described by eq 2 turns out to be identical to that obtained for drops in an extensional flow.[20,31] Interestingly, according to eq 2, τ does not depend neither on the angular speed ω nor on its change $\Delta\omega$.

The theory of ref 20 is limited to nearly spherical shapes. Hu and Joseph have investigated the opposite limit of very elongated drops,[19] proposing a semiempirical expression to fit the results of numerical simulations and experiments. The relaxation time may be cast in the following form:

$$\tau = \frac{\eta_d r_{eq}}{\Gamma} f_J(\lambda, l_{eq}, r_{eq}, R_c) \tag{3}$$

where $f_J(\lambda, l_{eq}, r_{eq}, R_c)$ is a function of the viscosity contrast, the inner radius of the cylindrical container, R_c, and the radius, r_{eq}, and length, l_{eq}, of the drop once equilibrium is reached at the final rotation speed ω_f. This expression was derived for elongated drops, contrary to the theory of ref 20. However, both theories deal with the case where the change of the drop shape results from a small speed jump. Equation 3 is qualitatively different from eq 2, since it predicts a dependence of τ on the equilibrium shape of the drop via r_{eq} and l_{eq}, and hence on ω_f. Hu and Joseph noticed that their theoretical expression for τ typically underestimates the time observed in experiments.[17,19] They argued that the detailed form of the flow around the end-caps of the drop may slow down its relaxation and account for this discrepancy.

So far, we briefly reviewed the theoretical background for the case of immiscible fluids displaying a non-negligible surface tension, for which spinning drop tensiometry was originally conceived. However, SDT has been also used, albeit much less frequently, to investigate the drop shape in miscible environments, aiming at measuring capillary forces between miscible fluids.[24−26] Unfortunately, there is no theoretical prediction available so far for this case. Capillary phenomena are expected to be weak, if not negligible, in miscible fluids. It is therefore interesting to briefly recall available results on the behavior of immiscible drops in the limit of vanishing interfacial tension. We focus mostly on the "bubble" limit, i.e., for the vanishing viscosity ratio λ between the drop and the surrounding fluid, and for intermediate ratios, as these cases will turn out to be of interest in our experiments.

In the cases of vanishing or intermediate viscosity ratios, Lister and Stone[29] have obtained asymptotic scaling laws for spinning drops in an unbounded geometry. The drops are assumed to be long and slender, with (time-dependent) equatorial radius a_0 much smaller than the length l. At all times, the interface between the two fluids is supposed to be infinitely sharp and stable, and the surface tension is supposed to be negligible. The rate of elongation and thinning is estimated by imposing a balance between the centrifugal pressure $\frac{1}{2}\Delta\rho\omega^2 a_0^2$ times the area $O(\pi a_0^2)$ over which it acts, and the dominant resisting viscous stress times the area over which it acts. The viscous stress is found to depend on both the viscosity ratio λ and the aspect ratio $l/2a_0$. We anticipate here that for the drop-background fluid system that we will consider hereafter, namely a drop containing 5 wt % H2O and 95 wt % glycerol suspended in pure glycerol, $\lambda = 0.537$ and $1 \lesssim l/2a_0 \lesssim 50$.

As it will turn out to be relevant for our drops, we first discuss the low viscosity ratio limit ($\lambda \ll 2a_0/l \ll 1$), for which the motion of the internal fluid as the drop extends generates less viscous dissipation than the deformation of the external fluid. Because of the centrifugal pressure, the shape of very elongated drops is expected to be close to that of a cylinder with domed end-caps. For small λ, the primary resistance to deformation is due to the displacement of the background fluid as the drop elongates. A force balance in the neighborhood of the end-cap, which has radius $O(a_0)$, surface area $O(2\pi a_0^2)$ and moves at velocity $U = \frac{1}{2}dl/dt$, yields $2\pi a_0^2 \eta_e U/a_0 \simeq \frac{1}{2}\Delta\rho\omega^2 a_0^2 \pi a_0^2$. Using volume conservation in the approximate form $V \simeq 2\pi a_0^2 l$ and estimating the velocity as $U \simeq l/2t$ yields the time-dependent length,

$$l(t) \simeq \left(\frac{\Delta\rho\omega^2 V^{3/2}}{\eta_e}\right)^{2/5} t^{2/5} \tag{4}$$

where for clarity we have dropped multiplicative numerical constants.

For more viscous drops, the shear stresses generated by the motion of the internal fluid along the rotation axis toward the drop ends become relevant and along the (half) length of the drop a pressure gradient $\Delta\rho\omega^2 a_0^2/l$ is established. The shear within the drop occurs on a length scale $O(a_0)$, whereas the external shear occurs on a somewhat larger scale $O(a_0 \ln(l/a_0))$, as shown in refs 32,33 by analyzing the axial motion of a slender body with radius a_0 and length l. The relative magnitudes of λ and $1/\ln(l/2a_0)$ controls which shear term contributes most. For the case $\lambda \ll 1/\ln(l/2a_0)$, the internal shear is dominant and is $O(\eta_d U/a_0)$, while the total resistance along the whole drop length is $O(\pi l \eta_d U)$. The rate of extension is then,[29]

$$l(t) \simeq \left(\frac{\Delta\rho\omega^2 V^2}{\eta_d}\right)^{1/4} t^{1/4} \tag{5}$$

In the opposite case, $\lambda \gg 1/\ln(l/2a_0)$, similar estimates lead to the following:[29]

DOI: 10.1021/acs.langmuir.9b02091
Langmuir 2019, 35, 11330−11339

$$l(t) \simeq \left(\frac{\Delta\rho\omega^2 V^2}{\eta_e}\right)^{1/4}\left(t\ \ln\frac{t}{\bar{t}}\right)^{1/4} \tag{6}$$

where $\bar{t} = \eta_e/(\Delta\rho\omega^2 V^{2/3})$ and the factor $\ln(t/\bar{t})$ arises from a leading-order expansion of $\ln(l/2a_0)$, which is assumed much larger than 1. It is worth noting that for our drops with 5 wt % H_2O and 95 wt % glycerol in a bath of pure glycerol one has $\bar{t}$ = 0.032 s and the logarithmic correction is negligible on the typical experimental time scale.

For a larger viscosity ratio, $\lambda \gg (l/2a_0)^2/\ln(l/2a_0) \gg 1$, extended drops resist deformation under the centrifugal pressure primarily owing to the internal gradient of the axial velocity. The deformation is analogous to the stretching of a piece of toffee.[29] This case is not relevant to our experiments and will not be discussed further.

■ EXPERIMENTAL SECTION

Materials. Glycerol (≥99.5 wt %) was purchased from Sigma-Aldrich and used without further purification. Silicone Oil (SO) has been purchased from Brookfield Ametek and used as-received. Milli-Q ultra pure water has been employed to prepare the water−glycerol mixtures. Densities ρ and zero-shear viscosities η at T = 25 °C of these liquids are reported in Table 1. Fluorescein (disodium salt) (from Merck KGaA) was dissolved in all water/glycerol drops (at a concentration of 2×10^{-3} wt/wt), for which pure glycerol was the background fluid.

Table 1. Mass Density and Viscosity of the Fluids Used in This Work

liquid	ρ (g/cm^3)	η (mPa s)[a]
SO	0.971[b]	91 680
Glycerol ($c_w \leq 0.02$)	1.260 ± 0.001	800.0 ± 0.1
H_2O-Gly (c_w = 0.05)	1.250 ± 0.001[c]	430.8 ± 0.1

[a]The viscosity of the water−glycerol mixture and the pure glycerol were measured performing steady rate rheology experiments at shear rates ranging from 10 s^{-1} up to 300 s^{-1}, using a stress-controlled AR 2000 rheometer (TA Instruments) equipped with a steel cone-and-plate geometry (cone diameter = 50 mm, cone angle = 0.0198 rad). All samples showed pure Newtonian response with no dependence of viscosity on the shear rate. [b]The viscosity and the density of SO are those quoted by the supplier company. [c]The density of the water-glycerol mixture was inferred from the measured zero-shear viscosity, using tables reporting both η and ρ as a function of c_w.[34]

Experimental Setup. All experiments were performed with a Krüss spinning drop tensiometer. Rates of rotation were accurate to 1%. The temperature was always set to 25.0 ± 0.5°C and kept constant using a flow of temperature-controlled air. Different tests were performed with rotation rates ranging from 6000 to 15 000 rpm, such that buoyancy effects were negligible compared to centrifugal ones: the displacement of the drop off the rotation axis due to buoyancy was always smaller than 5 μm, as calculated following ref 35. All drops were illuminated by a blue Light Emitting Diode (LED) with a dominant emission wavelength of 469 nm. Measurements were performed using a cylindrical capillary with internal diameter $2R_c$ = 3.25 mm. A CMOS camera (Phantom Miro 310 by Vision Research) run at 100 frames per second was used to record movies during the relaxation of immiscible drops of SO in glycerol. The camera was equipped with an objective by Nikkor (AF-Micro Lens 60 mm f/2.80, yielding a magnification M = 1). No dye labeling was used for the immiscible fluids, since the persistent, sharp contrast of refractive index between the drop and the surrounding fluid allows the drop boundary to be clearly visualized and its position to be accurately tracked in time, with an accuracy of 1 pixel, equivalent to 20 μm. For the immiscible SO/glycerol systems, the lighter fluid (SO) was deposited on one cap of the capillary. The capillary was spun at high speed and ω was then reduced by an amount $\Delta\omega$. This resulted in the formation of an isolated drop due to the viscous pinch-off mechanism induced by surface tension.[36] Drops of different volume V were obtained by depositing a larger initial volume of SO in the capillary. In all cases drops were in full contact with the surrounding fluid once the capillary was spun. The equilibrium between SO drops and glycerol was further tested by checking the reversibility of drop shapes performing a few elongation-retraction cycles.

Imaging the "interface" between two miscible fluids, by contrast, is more challenging. First of all, the sharp optical contrast characterizing the boundary between the two fluids when they are initially brought in contact vanishes in few seconds, due to diffusion that smears out the concentration gradient. The smearing time is much smaller than the typical duration of our experiments, which is on the order of several minutes. Fluorescent labeling was therefore needed to track the drop elongation. Under the illumination of the blue LED light, fluorescein-rich drops appear as bright green-yellow regions, since the fluorescein adsorption and emission spectra (in polar solvents) are peaked at $\lambda \approx 485$ nm and $\lambda \approx 511$ nm,[37,38] respectively. The good contrast with the dark background allows for a precise measurement of the position and shape of the miscible drops as a function of time. In particular, we measure the drop length from the intensity profile on the drop axis: we define l as the distance between the two apical points of the drop end-caps where the intensity profile reaches half of its maximum value.

In order to follow the evolution of very elongated miscible drops, we have extended the field of view in the direction of the capillary axis (the x direction in Figure 1). The custom imaging setup designed to

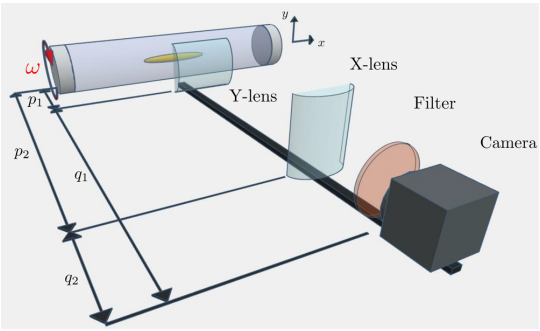

Figure 1. Setup used to characterize the extensional dynamics of fluorescent drops (water-glycerol mixture, c_w = 0.05) in a miscible background fluid (pure glycerol, $c_w \approx 0$). The drop is retro-illuminated by a series of LED (not shown for clarity).

this end is sketched in Figure 1. The setup consists in a set of two plano-convex cylindrical lenses (Newport CKX17-C) sharing the same optical axis. The first lens, labeled Y-lens in Figure 1, expands the image in the vertical direction with magnification M_y = 3.36, while the second one (X-lens) contracts it the horizontal direction, with magnification M_x = 0.3. Both lenses have an effective focal lens of 7.5 mm, and distances $p_1 = q_2$ = 9.5 cm and $p_2 = q_1$ = 32 cm as indicated in Figure 1. With this configuration the field of view in the x direction is 3.25 cm (half of the capillary length) while it is of 3 mm in the y direction. The setup allows the fluorescein concentration profile to be measured accurately in the y direction, while retaining a large field of view in the x direction, as required to follow very elongated drops. A blue-light filter removes the background light emitted by the source. In this configuration, a B/W CMOS camera (Toshiba Teli BU406M) run at a frame rate ⩽90 Hz was used, the image size being 2048 × 2048 pixels. The magnifications M_x and M_y were measured by inserting a calibrated plastic grid into the capillary filled with the external fluid (glycerol). The lattice spacing was then measured in

DOI: 10.1021/acs.langmuir.9b02091
Langmuir 2019, 35, 11330−11339

both the x and y directions, yielding calibration constants of 63 pixel/mm and 730 pixel/mm in the x and y directions, respectively.

For miscible fluids, all drops were injected directly in the capillary flushed and prefilled with glycerol. Care was taken to make sure that air bubbles were removed from the capillary before sample injection. All drops were formed in the prefilled capillary at rest, using a 1 μL syringe, and their volume has been fixed to 1 μL. The microsyringe was smoothly removed from the capillary, to avoid the formation of tails of fluoresceinated water−glycerol mixtures that would have hampered the formation of initially quasi-spherical drops.

In the following we shall compare our experimental results to theories assuming that, upon a change of ω, the final rotational speed is attained instantaneously and the fluids move solidly with the capillary. In experiments, however, changing ω and attaining a new rotational speed, uniform everywhere in the capillary, require a finite time due to the setup inertia and finite momentum diffusivity. It is therefore important to estimate these time scales and compare them to that of the drop evolution. In order to estimate τ_{setup}, the time required for the setup to change ω, we consider the worst-case scenario, ω_i = 6000 rpm and ω_f = 15 000, and measure the relaxation dynamics of a fast-relaxing drop of butanol in water, for which the theoretical relaxation time according to eq 2 is $\tau \ll 0.1$ s. We measure a much larger relaxation time of about 0.3 s, which we thus identify with the setup response time τ_{setup}. The time for the system (capillary, drop, and background fluid) to move uniformly at one single ω can be estimated as the ratio between the squared capillary radius and the momentum diffusivity. Typical values are of the order of $\tau_{diff} \simeq \frac{R_0^2\rho}{\eta_e} \approx 0.01$ s. In our experiments on both miscible and immiscible fluids, the drops always evolve on time scales much larger than both τ_{setup} and τ_{diff}; thus, we shall consider that the final rotation speed and the rigid motion of the fluids are attained instantaneously.

■ RESULTS AND DISCUSSION

Drop Extension in Immiscible Liquids. In order to test the predictions of existing theories, we investigated the relaxation dynamics of SO drops in an immiscible glycerol background, upon a rotational speed jump.

We start by showing in panels A to C of Figure 2 the equilibrium shape of a 2.95 μL SO drop in glycerol at different rotation speeds ω. In agreement with Vonnegut's and Laplace's theories,[39] we observe an increased stretching of the drop as ω grows. As predicted by Vonnegut's theory[11,39] for drops with aspect ratio $l/r \gtrsim 4$, we observe a direct proportionality between r^{-3} and ω^2 once the equilibrium shape of the drops is attained (Figure 2D). From the slope of the linear regression we obtain the surface tension between SO and glycerol: Γ = (17.81 ± 0.02) mN/m. It is worth noting that this value is less than half of that reported for SO and water (39.8 mN/m[40]) and is in agreement with recent results obtained for Γ in systems of nonpolar mineral oils in contact with water−glycerol mixtures with variable glycerol fractions.[41] We emphasize that by fitting r^{-3} vs ω^2 one reduces the experimental uncertainty affecting Γ with respect to measuring the drop radius at one single rotation speed. While yielding a very precise measurement, this procedure reduces the complications inherent to methods relying on the detection of the whole drop shape, e.g., the Young−Laplace fit of the drop surface, which are more sensitive to refraction effects due to the cylindrical capillary and are affected by any change in the illumination conditions.

The relaxation of the drop toward its equilibrium shape following a sudden jump of rotation speed $\Delta\omega = \omega_f - \omega_i$ has been investigated in a series of tests. In most experiments, the drop volume is fixed to V_1 = 2.95 μL and the initial speed is ω_i = 8000 rpm. The relaxation dynamics are measured for a series

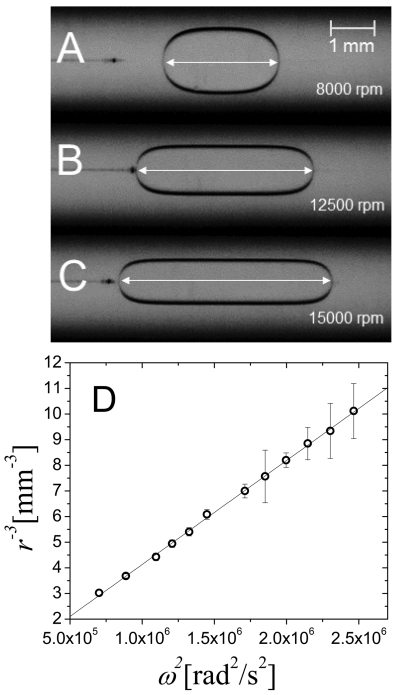

Figure 2. Spinning drops of SO at equilibrium in a reservoir of glycerol. A: ω = 8000 rpm. B: ω = 12 500 rpm. C: ω = 15 000 rpm. The white arrows show the length of the drops. D: r^{-3} vs ω^2 for one SO drop of volume V_1 = 2.95 μL in glycerol. The equilibrium radius is measured at the midsection of the drop. The solid line is a linear fit of the data, from which Γ has been calculated using Vonnegut's formula (eq 1). Error bars are calculated from the standard deviation of the radius over time.

of rotational speed jumps ranging from $\Delta\omega$ = 1000 rpm to $\Delta\omega$ = 7000 rpm. The time dependent drop length normalized by l_0 is shown in Figure 3A. Some of the relaxation tests have been repeated for smaller drops with volume V_2 = 0.66 μL. Finally, we have performed drop retraction experiments, corresponding to $\Delta\omega < 0$.

Equation 2 predicts that the relaxation time τ normalized by the drop radius at rest a is independent of the drop volume V and of $\Delta\omega$, while τ should depend on the value of the interfacial tension and on the viscosities of the two fluids. We test this prediction by showing all the normalized relaxation times τ/a in Figure 3B. Indeed, the measured normalized relaxation times are neither affected by the drop volume, nor by the magnitude or the sign of $\Delta\omega$. To further corroborate this scenario, we report in Figure 3C the normalized relaxation curves $\frac{l-l_0}{l_\infty - l_0}$, where l_∞ and l_0 are measured at equilibrium for each rotation speed. All data collapse onto the mastercurve $\frac{l-l_0}{l_\infty - l_0} = 1 - \exp[-(t/\tau)_{av}]$, with $(\tau/a)_{av}$ = 4.9 ± 0.2 s/mm the scaled relaxation time averaged over all the experiments.

We find an excellent agreement between the scaled drop relaxation time and the theoretical value predicted by the Stone and Bush theory,[20] $(\tau/a)_{th} = \frac{\eta_e}{\Gamma} f(\lambda)$= 4.97 ± 0.01 s/mm. Remarkably, the theory of ref 20 turns out to be an

DOI: 10.1021/acs.langmuir.9b02091
Langmuir 2019, 35, 11330−11339

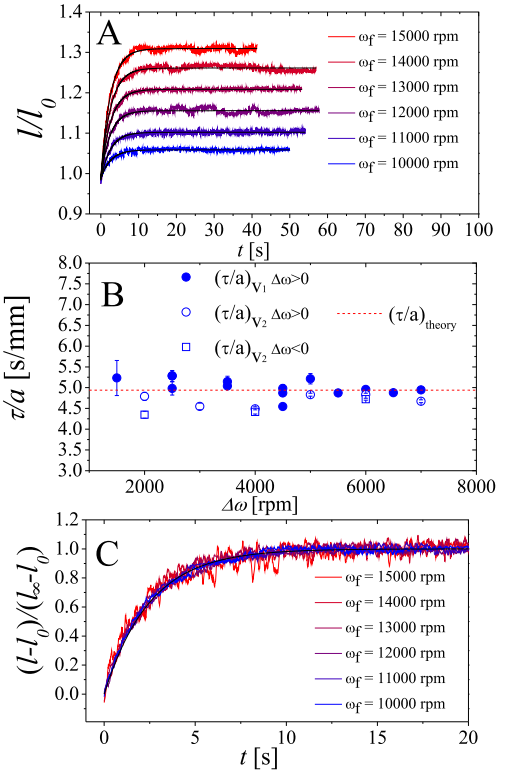

Figure 3. A: Normalized length l/l_0 of silicone oil drops in glycerol as a function of time for different rotation speed jumps $(\omega_f - \omega_i)$, with ω_i = 8000 rpm. B: Relaxation time normalized by the drop radius at rest as a function of the magnitude of the speed jump, for all experiments. The drop volume and the sign of $\Delta\omega$ are shown by the labels. The dashed red line shows the prediction of eq 2.[20] C: Scaled length $(l - l_0)/(l_\infty - l_0)$, where the initial, l_0, and asymptotic, l_∞, drop lengths are obtained as detailed in the text.

excellent predictive tool for the relaxation dynamics of viscous drops well beyond the limit of nearly spherical drops and small Bond number $\mathrm{Bo} = \frac{\Delta\rho\omega^2 a^3}{\Gamma} \ll 1$, for which it has been derived. Indeed, for our SO drops the aspect ratio $l/2r$ ranges from 1.00 to 5.25 and $1.4 \leq \mathrm{Bo} \leq 9.1$. Our findings suggest that higher order spherical harmonics that should be added to model the shape of elongated droplets, leading to corrections to the expression derived in ref 20 for the velocity and pressure fields, do not influence appreciably the drop dynamics. More theoretical work will be needed to confirm this scenario.

Evolution of Drops in a Miscible Background Fluid. Studying the drop evolution in a miscible background fluid is not an easy task as capillary effects due to a gradient of concentrations[42,43] are transient and their magnitude is expected to be very weak in miscible molecular fluids, for which typical estimates of the EIT are smaller than 1 mN/m.[24−26] Moreover, stresses induced by secondary flows in the spinning capillary may be comparable to or even larger than those due to surface tension, resulting in permanent drop deformation or time dependent instabilities.[23] Indeed, when a capillary starts rotating, the background fluid within the shear layer is pushed toward the drop center, as pointed out by Currie et al.[35] and Manning et al.,[23] who showed that this effect is large enough to deform drops in water−hydrocarbon−surfactant systems with an equilibrium interfacial tensions of the order of 10 μN/m. Secondary flows cause long lasting dog-bone drop shapes that are unusable for determining the interfacial tension with eq 1, and affect the drop elongation dynamics. For our miscible systems, we have observed dog-bone shapes for all drops composed of a water−glycerol mixture with a water mass fraction $c_w > 0.05$ and immersed in pure glycerol. We shall discuss the evolution of these dog-bone shaped drops in a forthcoming publication. Here, we report data for drops with c_w = 0.05, which retain a end-capped cylindrical shape over (at least) thousands of seconds, for all probed ω_f. A typical drop is shown in Figure 4, for different times t following a jump of the rotational speed from ω_i = 0 to ω_f = 15 000 rpm at t = 0.

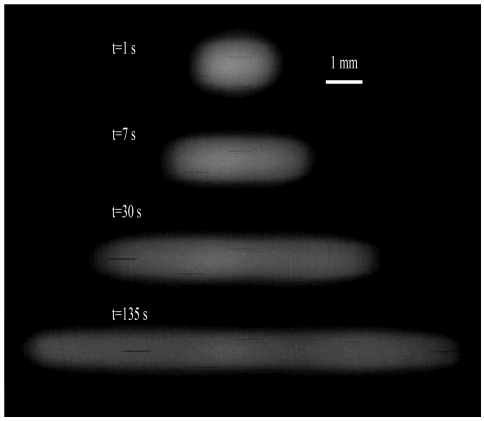

Figure 4. Temporal evolution of the H_2O−Glycerol drop (c_w = 0.05) in pure glycerol at ω_f = 15 000 rpm. t = 0 represents the beginning of the rotation. All drops are shown at an aspect ratio of 1.

Figure 5A shows the drop length as a function of time for four identical drops, with V = 1 μL and c_w = 0.05. In all experiments, ω_i = 0, while the final angular speed has been varied in the range 6000−15 000 rpm, as shown by the labels. In all cases, the increase of the drop length is very well fitted by a power-law: $l(t) = l_0 + \alpha t^m$. The fitting parameters α and m are reported in Table 2. To monitor possible deviations from a power-law behavior, we compute the time-dependent (local) exponent $m(t) = \frac{\mathrm{dlog}[l(t) - l_0]}{\mathrm{dlog}(t)}$, shown in the inset of Figure 5B. For all data sets, m is very close to 0.4 throughout the duration of the experiment, with no systematic deviations.

The values obtained for m are in very good agreement with $m = \frac{2}{5}$ as predicted by Lister and Stone for the "bubble-like" regime (eq 4), e.g., for drops with negligible effects of intradrop stresses. To further test the applicability of eq 4, we inspect the ω_f dependence of the prefactor α. We find $\alpha \sim \omega_f^{0.83 \pm 0.12}$, very close to the scaling $\alpha \sim \omega_f^{4/5}$ predicted by eq 4. Indeed, Figure 5B shows that all the data nicely collapse onto a mastercurve when using the scaled variable $(l - l_0)/\omega_f^{4/5}$ as suggested by eq 4. Interestingly, we find that the bubble-like regime extends beyond the limits described originally in ref 29. Indeed, in our experiments λ = 0.537 < 1 and the aspect ratio

DOI: 10.1021/acs.langmuir.9b02091
Langmuir 2019, 35, 11330−11339

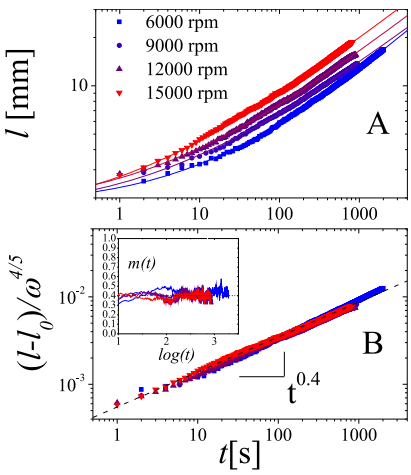

Figure 5. A: Temporal evolution of the H_2O−Glycerol drop length in pure glycerol at different rotation speed ω_f as indicated by the labels. Solid lines are best fits to a power-law growth, $l(t) = l_0 + \alpha t^m$. B: Rescaled increase of the drop length $(l - l_0)/\omega_f^{4/5}$, as a function of time. The dashed line shows the best fit obtained using the scaling law $l - l_0 \sim t^{2/5}$ predicted by Lister and Stone[29] (eq 4). The inset shows the time-dependent (local) exponent $m(t) = d\log(l-l_0)/d\log(t)$.

Table 2. Fitting Parameters for the Data Shown in Figure 5

ω_f (rpm)	α (mm/s^m)	m^a
15 000	1.227 ± 0.003	0.3934 ± 0.0004
12 000	0.962 ± 0.003	0.3960 ± 0.0005
9000	0.864 ± 0.002	0.3870 ± 0.0005
6000	0.525 ± 0.001	0.44 ± 0.02

[a]The reported errors are those on the fit parameters of the nonlinear regression of the experimental data performed with the Origin software (OriginLab corporation).

of the drop at its maximum (measurable) extension is $2a_0/l \approx 0.02$, so that one has $2a_0/l \ll \lambda < 1$. This is to be compared to $\lambda \ll 2a_0/l \ll 1$, as postulated in ref 29 for the bubble-like regime.

Overall, our data for miscible drops are very well accounted for by the model of ref 29 which was developed for immiscible fluids in the limit $\Gamma \to 0$. The agreement with the theory by Lister and Stone strongly suggests that capillary forces do not affect significantly the dynamics of our miscible drops. This is consistent with what expected for a pair of miscible fluids with a very low compositional gradient at their boundary (due to molecular diffusion) and with the fact that interfacial stresses further decay to zero as diffusion smears out the interface. It is furthermore consistent with previously reported data for the effective interfacial tension in water−glycerol mixtures,[24] from which we expect $\Gamma \ll 0.02$ mN/m for our system. We expect our results to be generic for fluids miscible in all proportions and far from critical points, where mutual diffusion and interfacial stresses may be affected by large fluctuations and the vicinity to demixing regions present in the phase diagram of the two-fluid system.

It is also worth noting that the interface between the two fluids is supposed to be infinitely sharp in ref 29 while it is smeared out by diffusion in our experiments. It is thus important to analyze the effects of diffusion to rationalize why the diffusion-free model by Lister and Stone describes our data so well. Due to diffusion, the effective surface tension tends to decrease with time, since the composition gradient at the interface diminishes. However, this evolution is most likely masked by the fact that for miscible systems Γ is already low enough to meet the $\Gamma \to 0$ condition postulated in ref 29 at all times. Diffusion may also impact the drop evolution in a more subtle way, by coupling to the centrifugal forcing: the forcing may change the evolution of the concentration profile; in turn, a smeared profile modifies the centrifuge forces. We first show that in fact the centrifugal forcing does not affect Fickian diffusion within the capillary. By balancing the entropic force (diffusion) and the centrifugal one[45] acting on all fluid elements in the capillary, the length scale over which the mass distribution of the two liquids is affected by rotation may be estimated, and the approximate equilibrium profile of water molecules in a water/glycerol mixture at $\omega > 0$ can be calculated. Following[44] we obtain the following:[45]

$$x_w(r) \sim \exp\left[-\frac{r^2}{l_{\omega_f}^2}\right] \tag{7}$$

where x_w is the mole fraction of water in the mixture and l_{ω_f} is the rotational length,

$$l_{\omega_f} = \frac{1}{\omega_f}\sqrt{\frac{2RT}{v_w\rho_{av} - M_w}} \tag{8}$$

i.e., the analogous to the gravitational length calculated under static conditions.[44] Here R is the universal gas constant, T the absolute temperature, M_w and v_w the molecular weight and the partial molar volume of water, and ρ_{av} the average density of the mixture. For water and glycerol at ω_f = 15 000 rpm we obtain $l_{\omega_f} \simeq 2.75$ m much greater than the capillary radius,[45] showing that in our system the centrifugal forcing is far from affecting interdiffusion between the drop and the surrounding liquid.

Having established that diffusion can be safely taken to be Fickian, we discuss its effect on the centrifugal forcing. Although the diffusion of water initially contained in the drop is a slow process, its effect over the typical duration of our experiments (several hundreds of seconds) is not negligible. Indeed, it takes about 710 s for a water molecule to diffuse in glycerol over a distance of 100 μm:[46] diffusion does indeed smear out significantly the interface between the drop and the surrounding medium during the experiment. Because of smearing, the pressure field in the capillary is different from that for a sharp interface. In our experiments the dominant contribution to the drop dynamics arises from the pressure jump ΔP across the end-caps of the drop; we thus calculate ΔP for the two cases of a sharp or diffused interface. For a sharp interface, the net pressure exerted on the head of a quasi cylindrical drop is as follows:[29]

$$\Delta P_{sharp} \simeq \frac{1}{2}\Delta\rho\omega_f^2 r_0^2 \tag{9}$$

where r_0 is the radius of the drop with sharp boundaries.

Equation 9 is actually a particular case of a more general expression that arises from the difference between the pressure field integrated along two distinct radial trajectories: one lying outside the spinning drop, the second one partially included in

DOI: 10.1021/acs.langmuir.9b02091
Langmuir 2019, 35, 11330−11339

the drop, as sketched in Figure 6. Under rotation, this gives rise to an effective hydrostatic pressure on the drop that reads:

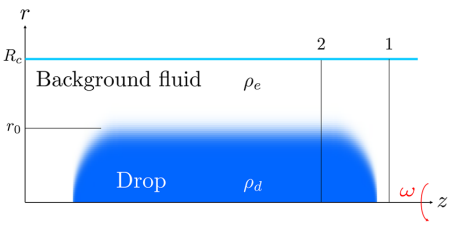

Figure 6. Scheme for the general case of a drop with diffused interface. The pressure field can be integrated on lines 1 and 2 to obtain the forcing on the drop.

$$\Delta P_d \simeq \omega_f^2 \int_0^{R_c} [\rho_1(r) - \rho_2(r)] r \, dr \tag{10}$$

where ρ_1 is the density profile along the line 1, equal to the density of the surrounding liquid, ρ_2 is the density profile along the line 2, and R_c = 1.625 mm for our capillary. The density profile along line 2 is computed by solving the diffusion equation along the radial direction r.

Since diffusion is slow, one can simplify the problem by considering the section sketched in Figure 6 as being composed by two semiplanes separated by an initially planar boundary at distance r_0 from the origin, the latter corresponding to the rotation axis of the capillary. Considering that the density of water−glycerol mixtures varies linearly with the water weight fraction for $0 \leq c_w \leq 0.05$,[47] eq 10 can be written as follows:

$$\Delta P_d \simeq \omega_f^2 \int_0^{R_c} \left\{ \frac{\Delta\rho}{2} - \frac{\Delta\rho}{2} \mathrm{erf}\left[\frac{(r - r_0)}{\sqrt{4 D_w t}} \right] r \right\} dr \tag{11}$$

where r_0 is the drop radius, $\Delta\rho$ = 10 kg/m^3 is the initial density difference between the drop and the background fluid, D_w = 1.4 · 10^{-11} m^2/s is the diffusion coefficient of water in glycerol,[46] and t is the time elapsed since the drop has been inserted in the capillary. From the experimental images we estimate that the radius r_0, defined as the position of the flex point of the radial intensity profile, lays between 0.25 and 0.35 mm. By using eq 11 an upper bound for the relative variation of the hydrostatic pressure can be calculated: $(\Delta P_{sharp} - \Delta P_d)/\Delta P_{sharp} \leq 30\%$ for t = 1000 s, while the same quantity is as small as 3% for t = 100 s. We thus expect that the dynamics are essentially not affected by diffusion-driven effects for the first few hundred seconds, while some limited impact may be present in the last time decade (10^2−10^3 s) explored in our experiments. Consistently with this analysis, Figure 5 shows no significant deviations from the Lister-Stone theory up to t = 2000 s. Note that, as pointed out first by Zeldovich[48] and then by Zoltowski et al.,[26] mass conservation implies that as the drop is stretched the transition zone at its boundary is thinned. This effect likely keeps the concentration profile sharper than expected from Fickian diffusion, thus contributing to maintain the scaling predicted by eq 4.

■ CONCLUSIONS

We have experimentally investigated the relaxation of Newtonian spinning drops after a jump of angular speed, detailing two radically different cases: (i) immiscible fluids with viscosities high enough for the slow extensional dynamics to be fully uncoupled from the inertial response of the tensiometer; (ii) miscible fluids with negligible capillary effects and no deformations due to secondary flows in the rotating capillary. A crucial experimental improvement was the use of a custom imaging geometry, which allowed us to follow the elongation of drops up to very large aspect ratios, a regime never probed experimentally before. By imaging the full drop, we were furthermore able to rule out the presence of shape instabilities for all the samples discussed here, and unambiguously ascertain whether or not a steady state was eventually reached.

For immiscible fluids, we have found that the drop dynamics is described remarkably well by predictions for a quasi-spherical drop subject to small deformations, for which the typical relaxation time does not depend on the forcing, i.e., the product $\omega^2\Delta\rho$, nor on the equilibrium length or shape of the drops. For these immiscible drops, the relaxation dynamics depend only on the interfacial tension Γ, the drop radius at rest, and the viscosity of the drop and background fluids. An excellent quantitative agreement is found with the theory proposed in ref 20 with a larger than expected domain of applicability.

Drops in miscible environments exhibit a totally different relaxation dynamics, their length increasing indefinitely according to a power law, in agreement with predictions for "bubble-like" dynamics in absence of capillary effects: $l(t) - l(0) \sim \alpha \times t^{2/5}$, with $\alpha \sim \omega_f^{4/5}$.[29] A global theory that fully captures the experimental droplet relaxation under the assumption of a pure unsteady extension superposed to a rigid rotation is still missing, as also pointed out by Joseph et al.[17] Our results suggest that existing models based on the calculation of the contribution of the dominant viscous stresses inside and outside the drop reproduce very well the experimental data. This observation should be useful for guiding future theoretical efforts.

Finally, it is worthwhile to briefly compare our results in light of previous works, notably ref 24 which reported SDT measurements of the effective interfacial tension between a drop of water and water−glycerol mixtures as the background fluid. In these experiments, which are similar to those reported here for miscible fluids, the concentration c_g of glycerol in the background fluid was systematically varied. It was observed that Γ vanishes as c_g decreases, becoming unmeasurable for c_g < 40% wt. This is consistent with our result that the elongation dynamics of drops with composition very close to that of the background fluid is well described by Lister and Stone's theory, where interfacial tension is neglected.[29] Indeed, in our system the composition mismatch is smaller than the smallest one for which Petitjean was still able to measure Γ (compare c_w = 5 wt % to c_g = 40 wt %). That said, we believe that the conclusions of previous works probing dynamics of drops in miscible environments[24−26] should be revisited and rechecked as the existence of a true steady state in miscible fluids, assumed in these works, is strictly hampered by diffusion and a slow power-law dynamics could also be present in those systems.

The results presented here should help clarifying the debate on the behavior of spinning drops in miscible and immiscible background fluids. We hope that they will also stimulate further theoretical work in this field.

DOI: 10.1021/acs.langmuir.9b02091
Langmuir 2019, 35, 11330−11339

■ ASSOCIATED CONTENT

Supporting Information

The Supporting Information is available free of charge on the ACS Publications website at DOI: 10.1021/acs.langmuir.9b02091.

Calculation of the rotational length for water−glycerol mixtures (PDF)

■ AUTHOR INFORMATION

Corresponding Author

*E-mail: domenico.truzzolillo@umontpellier.fr.

ORCID

Luca Cipelletti: 0000-0003-2956-7580

Domenico Truzzolillo: 0000-0002-1841-969X

Notes

The authors declare no competing financial interest.

■ ACKNOWLEDGMENTS

We thank L. Isa for fruitful discussions and gratefully acknowledge support from the Centre national d'études spatiales (CNES).

■ REFERENCES

(1) Rayleigh, L. The equilibrium of revolving liquid under capillary force. *Philos. Mag.* **1914**, *28*, 161.

(2) Janiaud, E.; Elias, F.; Bacri, J.-C.; Cabuil, V.; Perzynski, R. Spinning ferrofluid microscopic droplets. *Magnetohydrodynamics* **2000**, *36*, 300−304.

(3) Hill, R. J. A.; Eaves, L. Nonaxisymmetric Shapes of a Magnetically Levitated and Spinning Water Droplet. *Phys. Rev. Lett.* **2008**, *101*, 234501.

(4) Chandrasekhar, S. *Hydrodynamic and Hydromagnetic Stability*; Oxford University Press, 1961.

(5) Li, H.; Fang, W.; Li, Y.; Yang, Q.; Li, M.; Li, Q.; Feng, X.-Q.; Song, Y. Spontaneous droplets gyrating via asymmetric self-splitting on heterogeneous surfaces. *Nat. Commun.* **2019**, *10*, 1−5.

(6) Filali, Y.; Er-Riani, M.; El Jarroudi, M. The deformation of a ferrofluid drop under a uniform magnetic field. *Int. J. Nonlin. Mech.* **2018**, *99*, 173−181.

(7) Kékesi, T.; Amberg, G.; Prahl Wittberg, L. Drop deformation and breakup in flows with shear. *Chem. Eng. Sci.* **2016**, *140*, 319−329.

(8) Holgate, J. T.; Coppins, M. Shapes, stability, and hysteresis of rotating and charged axisymmetric drops in a vacuum. *Phys. Fluids* **2018**, *30*, 064107.

(9) Zhang, K.; Liao, X. *Theory and Modeling of Rotating Fluids: Convection, Inertial Waves and Precession*; Cambridge University Press: Cambridge, 2017.

(10) Brown, R. A.; Scriven, L. E. The Shape and Stability of Rotating Liquid Drops. *Proc. R. Soc. London, Ser. A* **1980**, *371*, 331−357.

(11) Vonnegut, B. Rotating Bubble Method for the Determination of Surface and Interfacial Tensions. *Rev. Sci. Instrum.* **1942**, *13*, 6−9.

(12) Princen, H.; Zia, I.; Mason, S. Measurement of interfacial tension from the shape of a rotating drop. *J. Colloid Interface Sci.* **1967**, *23*, 99−107.

(13) Torza, S. The rotating-bubble apparatus. *Rev. Sci. Instrum.* **1975**, *46*, 778−783.

(14) Cayas, J.; Schechter, R.; Wade, W. *ACS Symposium*; Mittal, K. L., Eds.; Adsorption at Interfaces—American Chemical Society, 1975; Vol. *8*.

(15) Patterson, H. T.; Hu, K. H.; Grindstaff, T. H. Measurement of interfacial and surface tensions in polymer systems. *J. Polym. Sci., Part C: Polym. Symp.* **1971**, *34*, 31−43.

(16) Hsu, J. C.; Flumerfelt, R. W. Rheological Applications of a Drop Elongation Experiment. *Trans. Soc. Rheol.* **1975**, *19*, 523−540.

(17) Joseph, D. D.; Arney, M. S.; Gillberg, G.; Hu, H.; Hultman, D.; Verdier, C.; Vinagre, T. M. A spinning drop tensioextensometer. *J. Rheol.* **1992**, *36*, 621−662.

(18) Joseph, D.; Arney, M.; Ma, G. Upper and lower bounds for interfacial tension using spinning drop devices. *J. Colloid Interface Sci.* **1992**, *148*, 291−294.

(19) Hu, H.; Joseph, D. Evolution of a Liquid Drop in a Spinning Drop Tensiometer. *J. Colloid Interface Sci.* **1994**, *162*, 331−339.

(20) Stone, H.; Bush, J. Stone - Time-dependent drop deformation in rotating viscous fluid. *Q. Appl. Math.* **1996**, *54*, 551−556.

(21) Than, P; Preziosi, L; Josephl, D.D; Arney, M Measurement of Interfacial Tension between Immiscible Liquids with the Spinning Rod Tensiometer. *J. Colloid Interface Sci.* **1988**, *124*, 552−559.

(22) Verdier, C. *Topics in the Fluid Dynamics of Viscoelastic Liquids*, PhD dissertation; 1990.

(23) Manning, C. D.; Scriven, L. E. On interfacial tension measurement with a spinning drop in gyrostatic equilibrium. *Rev. Sci. Instrum.* **1977**, *48*, 1699−1705.

(24) Petitjeans, P. Une tension de surface pour le fluides miscibles. *C. R. Acad. Sci. Paris* **1996**, 673−679.

(25) Pojman, J. A.; Whitmore, C.; Turco Liveri, M. L.; Lombardo, R.; Marszalek, J.; Parker, R.; Zoltowski, B. Evidence for the Existence of an Effective Interfacial Tension between Miscible Fluids: Isobutyric Acid-Water and 1-Butanol-Water in a Spinning-Drop Tensiometer. *Langmuir* **2006**, *22*, 2569−2577.

(26) Zoltowski, B.; Chekanov, Y.; Masere, J.; Pojman, J. A.; Volpert, V. Evidence for the Existence of an Effective Interfacial Tension between Miscible Fluids. 2. Dodecyl Acrylate-Poly(dodecyl acrylate) in a Spinning Drop Tensiometer. *Langmuir* **2007**, *23*, 5522−5531.

(27) Lombardo, R.; Calabrese, I.; Gelardi, G.; Turco Liveri, M. L.; Pojman, J. A. The apparently anomalous effects of surfactants on interfacial tension in the IBA/water system near its upper critical solution temperature. *Colloid Polym. Sci.* **2016**, *294*, 1425−1430.

(28) Viner, G.; La Monica, T.; Lombardo, R.; Pojman, J. A. Effect of pseudo-gravitational acceleration on the dissolution rate of miscible drops. *Chaos* **2017**, *27*, 104603.

(29) Lister, J.; Stone, H. Time-dependent viscous deformation of a drop in a rapidly rotating denser fluid. *J. Fluid Mech.* **1996**, *317*, 275−299.

(30) Saad, S. M.; Policova, Z.; Neumann, A. W. Design and accuracy of pendant drop methods for surface tension measurement. *Colloids Surf., A* **2011**, *384*, 442−452.

(31) Rallison, J. M. The Deformation of Small Viscous Drops and Bubbles in Shear Flows. *Annu. Rev. Fluid Mech.* **1984**, *16*, 45−66.

(32) Batchelor, G. K. Slender-body theory for particles of arbitrary cross-section in Stokes flow. *J. Fluid Mech.* **1970**, *44*, 419.

(33) Cox, R. G. The motion of long slender bodies in a viscous fluid Part 1. General theory. *J. Fluid Mech.* **1970**, *44*, 791.

(34) *Physical Properties of Glycerine and Its Solutions*; Glycerine Producers' Association: New York, 1963.

(35) Currie, P.; Van Nieuwkoop, J. Buoyancy effects in the spinning-drop interfacial tensiometer. *J. Colloid Interface Sci.* **1982**, *87*, 301−316.

(36) Stone, H. A.; Bentley, B. J.; Leal, L. G. An experimental study of transient effects in the breakup of viscous drops. *J. Fluid Mech.* **1986**, *173*, 131.

(37) Panchompoo, J.; Aldous, L.; Baker, M.; Wallace, M. I.; Compton, R. G. One-step synthesis of fluorescein modified nano-carbon for Pd(ii) detection via fluorescence quenching. *Analyst* **2012**, *137*, 2054.

(38) Szalay, L.; Tombácz, E. Effect of the solvent on the fluorescence spectrum of trypaflavine and fluorescein. *Acta Phys. Acad. Sci. Hung.* **1964**, *16*, 367−371.

(39) Viades-Trejo, J.; Gracia-Fadrique, J. Spinning drop method. *Colloids Surf., A* **2007**, *302*, 549−552.

(40) Koos, E.; Johannsmeier, J.; Schwebler, L.; Willenbacher, N. Tuning suspension rheology using capillary forces. *Soft Matter* **2012**, *8*, 6620.

DOI: 10.1021/acs.langmuir.9b02091
Langmuir 2019, 35, 11330−11339

(41) Sinzato, Y. Z.; Dias, N. J. S.; Cunha, F. R. Experimental measurements of interfacial tension between liquid−liquid mixtures in the presence of surfactants. *Proceedings of the 23rd ABCM International Congress of Mechanical Engineering*; Rio de Janeiro, Brazil, 2015.
(42) Truzzolillo, D.; Cipelletti, L. Off-equilibrium surface tension in miscible fluids. *Soft Matter* **2017**, *13*, 13−21.
(43) Truzzolillo, D.; Mora, S.; Dupas, C.; Cipelletti, L. Non-equilibrium Interfacial Tension in Simple and Complex Fluids. *Phys. Rev. X* **2016**, *6*, 041057.
(44) Obidi, O.; Muggeridge, A. H.; Vesovic, V. Analytical solution for compositional profile driven by gravitational segregation and diffusion. *Phys. Rev. E: Stat. Phys., Plasmas, Fluids, Relat. Interdiscip. Top.* **2017**, *95*, 022138.
(45) See SI.
(46) D'Errico, G.; Ortona, O.; Capuano, F.; Vitagliano, V. Diffusion Coefficients for the Binary System Glycerol + Water at 25 °C. A Velocity Correlation Study. *J. Chem. Eng. Data* **2004**, *49*, 1665−1670.
(47) Cheng, N.-S. Formula for the Viscosity of a Glycerol-Water Mixture. *Ind. Eng. Chem. Res.* **2008**, *47*, 3285−3288.
(48) Zeldovich, Y. B. *Zh. Fiz. Khim. (in Russian)* **1949**, *23*, 931−935.

DOI: 10.1021/acs.langmuir.9b02091
Langmuir 2019, 35, 11330−11339

Supplemental material to
Spinning drop dynamics in miscible and immiscible environments

Alessandro Carbonaro,[1] Luca Cipelletti,[1] and Domenico Truzzolillo[1]

[1]*Laboratoire Charles Coulomb (L2C),*

UMR 5221 CNRS-Université de Montpellier, Montpellier, France

ROTATIONAL LENGTH FOR SPINNING WATER-GLYCEROL MIXTURES

In order to discuss the effect of diffusion on our experiments, we need to start by understanding whether there is an influence of the centripetal forcing on diffusion itself, i.e. if we can consider diffusion to be Fickian. We can indeed expect, in principle, the concentration profile of fluids in the capillary to be set by the rotation, in analogy with the exponential profile set by gravity [1]. This characteristic length scale of the problem determines then the effect of the centripetal forcing on diffusion: if this "rotational length" l_ω is much bigger than the capillary diameter d_c, we can consider the system to be freely diffusing without any influence of the centrifugal forcing, and diffusion to be Fickian. With a procedure analogous to that described in Ref. [1], at equilibrium we can write the variation of chemical potential along the radial coordinate r as

$$\left(\frac{d\mu_i}{dr}\right)_T = M_i\omega^2 r \tag{1}$$

for each species i, whose molecular weight is M_i. Similarly, for the pressure variation

$$\frac{dp}{dr} = \rho(r)\omega^2 r \tag{2}$$

where $\rho(r)$ is the density at distance r from the axis of rotation. If we consider the system as an ideal mixture we have then from thermodynamics

$$d\mu_i = v_i dp + \sum_j \frac{\partial \mu_i}{\partial x_j} dx_j \tag{3}$$

and

$$\mu_i = \mu_i^0 + RT \ln x_i \tag{4}$$

with T being the temperature, R the universal gas constant, v_i and x_i the partial molar volume and mole fraction of species i. Combining eq. 1 to 4 we get

$$\frac{RT}{x_i}\frac{dx_i}{dr} = \left[M_i - \rho(r)v_i\right]\omega^2 r \tag{5}$$

If we approximate $\rho(r)$ with a constant equal to the average density of the two fluids, i.e. $\rho(r) = \rho_{av}$, Eq. 5 can be integrated analytically. This approximation works well for fluids that have a similar density (in our case $\rho_{H_2O} = 1000\,\mathrm{kg/m^3}$ and $\rho_{gly} = 1260\,\mathrm{kg/m^3}$) and allows us to get an estimate of the rotational length of our system [1]. Integration of eq. 5 yields

$$x_i\left(r\right) \simeq x_i\left(0\right)\exp\left\{-\frac{(\rho_{av}v_i - M_i)\omega^2}{2RT}r^2\right\} \tag{6}$$

from which we can define the square rotational length l_ω^2,

$$l_\omega^2 = \frac{2RT}{(\rho_{av} v_i - M_i)\omega^2} \,. \tag{7}$$

For the case of water in glycerol at 15000 rpm, we obtain

$$l_\omega = \frac{1}{\omega}\sqrt{\frac{2RT}{\rho_{av} v_w - M_w}} \approx 2.75\,\mathrm{m} \gg d_c \tag{8}$$

and we can thus assume diffusion not to be affected by the centripetal forcing, and thus to be described by Fick's law.

[1] O. Obidi, A. H. Muggeridge, and V. Vesovic, Physical Review E **95** (2017), ISSN 2470-0045, 2470-0053, URL `https://link.aps.org/doi/10.1103/PhysRevE.95.022138`.

Chapter 3

Ultralow effective interfacial tension between miscible molecular fluids

Drops spinning in a denser background fluid do not always maintain a simple ellipsoidal shape. On the contrary, when the interfacial tension between the two fluids is sufficiently low, they can develop a so called "dumbbell" shape, with two bigger heads connected by a thinner central body. We have recently exploited such a radial deformation of drops to measure the ultralow effective interfacial tension between miscible molecular fluids. In the present chapter, we elucidate some aspects of our work and present the results recently published in [30].

3.1 Dumbbell shapes

In Ref. [11] we have shown that, when interfacial tension is negligible, spinning drops elongate indefinitely, following a power law dynamics:

$$l(t) \simeq \left(\frac{\Delta\rho\omega^2 V^{3/2}}{\eta_e} \right) t^{2/5} \,. \tag{3.1}$$

Here l and V are the drop length and volume, $\Delta\rho$ the density difference between the drop and the background fluids, ω the angular velocity and η_e the background fluid viscosity. In particular, we verified the validity of such power-law dynamics for one specific pair of miscible fluids with a small concentration gradient, namely a 5% H_2O - 95% glycerol mixture drop spinning in a reservoir of pure glycerol. In this case, drops always evolved maintaining an ellipsoidal shape. However, the dynamics are not the same for all values of the mass concentration c_w of water in the drop. Figure 3.1 reports the time evolution of the drop length for various water concentration in the drop and various rotation speeds. All drops spin in pure glycerol. The data in panel A are those presented in [11] for a water mass fraction $c_w = 0.05$. Remarkably, as the water concentration in the drop increases,

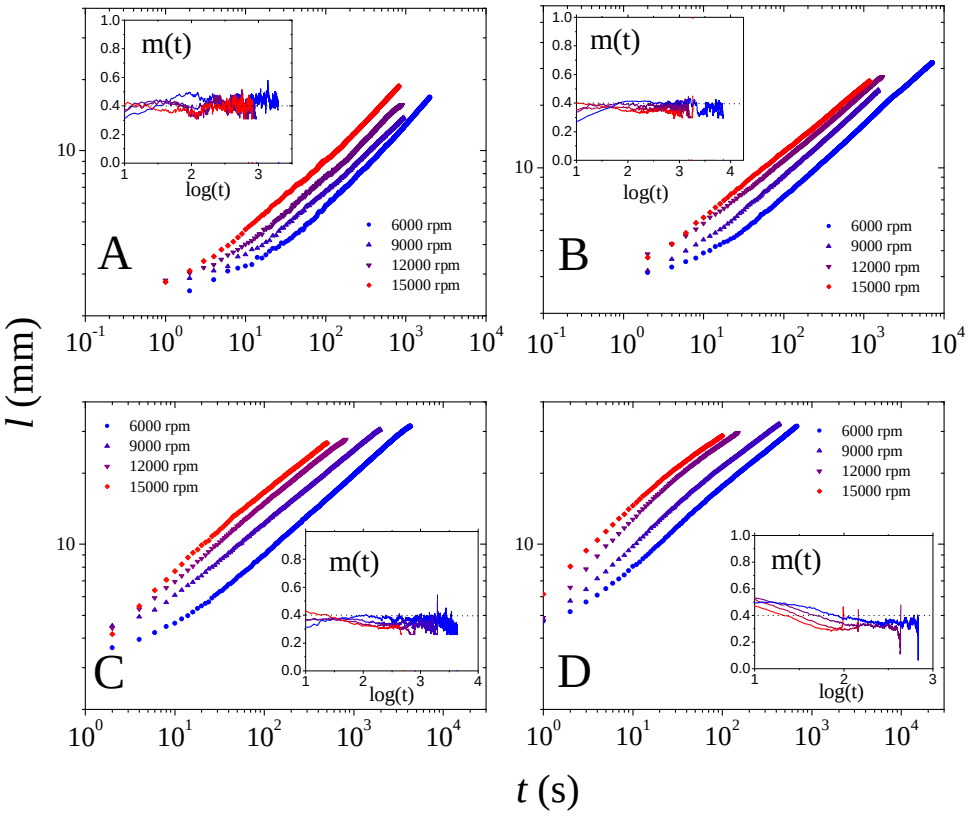

Figure 3.1: Elongation dynamics of drops of water-glycerol mixtures spinning in pure glycerol, for various rotation speeds. The drops have water mass fraction $c_w = 0.05$ in Panel A, 0.25 in Panel B, 0.45 in Panel C and 1 in Panel D. The four insets show the local exponent of the dynamics when they are described as a power law with an exponent dependent on time, as detailed in the text.

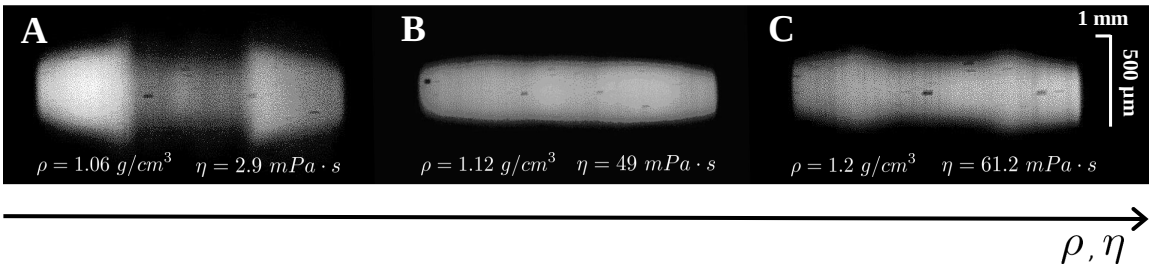

Figure 3.2: Images of drops of 75% H_2O - 25% glycerol (Panel A), triethylene glycol (Panel B) and 20% H_2O - 80 %glycerol (Panel C), all spinning in pure glycerol. Note the different magnification factors in the horizontal and vertical directions.

from panel A to panel D, the elongation dynamics of drops are no longer captured by Eq. 3.1, and tend to slow down as drops elongate. Furthermore, the slowing down of the dynamics is more evident for drops with a higher water content, and at higher angular velocity. In order to highlight such slowing down of the elongation dynamics, the insets of Fig. 3.1 show the local exponent m of $l(t)$, when the length is described as a power law, $l(t) \propto t^m$. Once again, $m(t)$ decreases over time for large c_w and ω, while $m(t) = 0.4$ for a low concentration mismatch between the drop and the background fluid (panel A).

One could think of a couple different explanation for the different behaviour of the elongation dynamics with respect to Eq. 3.1, at high c_w. The first possible cause for this phenomenon could be diffusion, which is stronger for less viscous, high-c_w drops. With time, diffusion smears out the concentration gradient at the drop surface, and consequently the density difference between the drop and background fluids. However, as already discussed in [11], the difference in centripetal forcing due to diffusion is negligible over the time scale of our experiment. Furthermore, this would not explain why $m(t)$ would decrease faster for higher angular velocities, for which experiments are shorter. A second possible explanation could be the presence of Korteweg stresses at the interface opposing drop elongation, which could be stronger for higher c_w due to the steeper concentration gradient between the drop and the background fluids. However, the reduction of $m(t)$ is observed over hundreds of seconds, while Korteweg stresses are expected to become negligible after a few seconds [30]. Indeed, as it will be detailed later in [30], diffusion is not sufficient to induce a strong variation of centripetal forcing, but it is enough to make EIT vanish over the time of the experiment.

As a consequence, neither diffusion nor Korteweg stresses alone can explain the data in Fig. 3.1. Furthermore, there is an additional, important aspect worth discussing for drops at high c_w, related to their shape. Remarkably, in an SDT experiment drops do not always maintain an ellipsoidal shape. On the contrary, for sufficiently low values of the interfacial tension, they develop a "dumbbell", or "dog-bone" shape, with two larger heads connected by a thinner central body. Such a phenomenon was reported already in 1977 by Manning and Scriven for the case of water-hydrocarbon-surfactant systems [45], for which Γ is as low as 10 µN/m, albeit no explanation could be provided. An example of such dumbbell shapes is reported in Fig. 3.2 (Fig. 1 in [30]). The drops in panels A and

C are composed of mixtures of water and glycerol, with water mass fractions $c_w = 0.75$ and $c_w = 0.2$, respectively. The drop in panel B, on the other hand, is made of triethylene glycol (TEG). All drops are spinning in pure glycerol, with which they are fully miscible. Note the different magnification factors in the horizontal x and vertical y directions, as images are optically compressed along x and expanded along y to increase the resolution. Remarkably, not only does Fig. 3.2 provide examples of dumbbell-shaped drops, but it also shows that such dumbbell shapes do not depend only on the density and viscosity contrast between the drop and background fluids. If this was the case, the TEG drop in panel B would indeed have an intermediate shape between the drops in panels A and C, since it has intermediate density and viscosity. This is clearly not the case, and Fig. 3.2 cannot be explained only by means of hydrodynamics arguments. On the contrary, the development of a dumbbell shape must depend on the molecular structure of the fluids, and hence on interfacial stresses arising from different molecular interactions. Therefore, investigating the origin and the temporal dynamics of these shapes naturally appears as a valid strategy to investigate the effective interfacial tension between the drop and the background fluid. This is indeed the strategy that we adopted. In the present chapter, we present the results obtained following this approach.

3.2 Concentration profiles: some geometrical considerations

In order to precisely characterise the time evolution of the drop shape we exploit fluorescent drops to extract the three-dimensional concentration profile $\tilde{\varphi}$ of the drop fluid in the capillary. The procedure to obtain $\tilde{\varphi}$ from the intensity of the fluorescence signal is described in [30]. Here we briefly recall the main features and make some comments.

The concentration of the fluorophore, which is proportional to the light intensity collected, follows closely the one of the drop fluid, since over the duration of one run there is not enough time to develop an appreciable difference in the distribution of the two components due to diffusion. As a consequence, one can measure $\tilde{\varphi}$ from the fluorescence intensity by means of some geometrical considerations. By dividing the drop in concentric cylindrical shells with a local value $\tilde{\varphi}_i$ of drop fluid concentration, one can write the fluorescence intensity at a given location with horizontal and vertical coordinates x and y as a sum over the contributions of all shell:

$$I(x, y) = \sum_{i=1}^{N} c_i(y)\tilde{\varphi}_i(x)\,. \tag{3.2}$$

Here $c_i(y)$ is a geometric factor that contains the length of the chord that traverses each shell i at coordinate y. We solve for $\tilde{\varphi}$ by recasting Eq. 3.2 in matrix form after discretizing both the x and y coordinates. In order to speed up the inversion of the matrix $\mathbf{C} \equiv c_i(y)$, we exploit the symmetry of the drop around the rotation axis. In practice, this means averaging around the rotation axis the upper and lower halves of the images, which allows also for improving the signal-to-noise ratio, a desirable feature due to the low intensity of the fluorescence signal. Note that such a procedure is only possible if the images are actually symmetric around the rotation axis, and the position of the latter is well established. Experimentally this is achieved by taking an image of a drop and by analysing the profile

of the fluorescence intensity, in order to determine the vertical coordinate of the maximum of the intensity and that of the center of mass of the signal, which should coincide for a perfectly symmetric image. if the two coordinates do not coincide, the viewing angle, i.e. the angle between the tensiometer and the rail supporting the optics and the camera, is adjusted and the position of the maximum of the intensity and of the intensity center of mass is checked again. The whole procedure is iterated as needed. The code used to extract the concentration profile is available at [46].

3.3 Determination of the deformation amplitude

Once obtained the three-dimensional concentration profile $\tilde{\varphi}(x, r)$ of the drop fluid in the spinning capillary, we define the drop surface as the set of points where $\tilde{\varphi}(x, r) = 0.5$, with $\tilde{\varphi}$ normalized to unity in the inner region of the drop, close to its axis. As an example, Fig. 3.3 shows the time evolution of the drop surface for a drop of water spinning in pure glycerol. The development of a dumbbell shape is evident. In order to quantitatively characterize the deformation, we define its amplitude h as the difference in radii between the larger heads and the thinner central body.

We emphasize that this is not sufficient to unambiguously define the deformation amplitude, because the profile of the drop surface is not perfectly symmetric. One possibility would be to take the difference between the absolute maximum radius and the minimum radius of the profile, at one drop head and around its center, respectively. A second strategy would be to exploit the drop symmetry, averaging the two maximum radii of the drop heads, at x_1 and x_2, and measuring the amplitude of the deformation by taking the difference with respect to the radius at the horizontal coordinate in the middle of the drop, at $x_M = \frac{x_1+x_2}{2}$. This second approach allows taking into account a possible asymmetry in the drop shape due to an imperfect injection in the capillary: a non-spherical drop would yield a skewed profile, with one of the two heads larger than the other. Averaging the two sides of the drop automatically includes the skewness of the interface profile, allowing one to directly characterize the amplitude of the radial deformation. By carefully looking at Fig. 3.3 it is possible to observe that indeed the interface profile is slightly skewed at short times, evolving towards a more symmetric shape. Such a behaviour is the signature of a

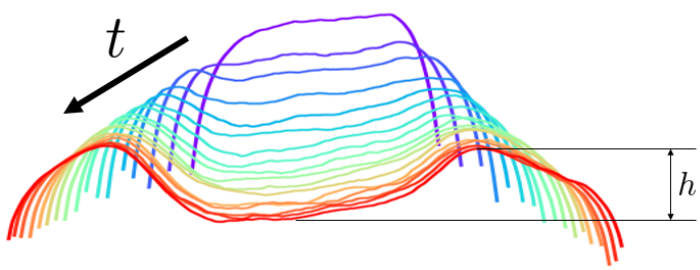

Figure 3.3: Time evolution of the interface profile for a drop of pure water spinning at 15500 rpm in a reservoir of pure glycerol, from $t = 1\,\mathrm{s}$ (purple) to $t = 18\,\mathrm{s}$ (red) by steps of $1\,\mathrm{s}$. Time $t = 1\,\mathrm{s}$ corresponds to the beginning of rotation.

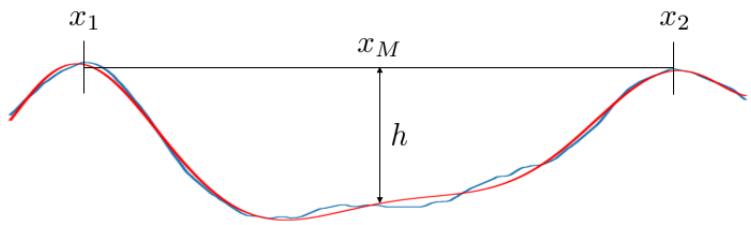

Figure 3.4: Interface profile (blue line) and polynomial fit of order 10 (red line) for a drop of pure water spinning in pure glycerol, at 15500 rpm and 15 s after the beginning of rotation.

drop which is not perfectly spherical at the beginning of rotation. Nevertheless, it is still possible to measure the deformation amplitude for a (slightly) skewed drop by averaging the left and right heads. This is indeed the procedure that we decided to use.

Once determined the position of the maximum and minimum radii, one still needs to decide how to measure the deformation amplitude h. In particular, we extracted h by directly measuring the radii from the interface profile, and also by fitting the latter with a polynomial function of order 10, in order to reduce possible noise. As an example, Fig. 3.4 shows a polynomial fit superposed to a selected interface profile.

The results obtained by measuring the deformation amplitude h on the polynomial fit and directly on the drop profile were always compatible,to within experimental uncertainty. In particular, the velocity of deformation, $v = \frac{dh}{dt}$, was always the same in the two cases. Since the latter is the quantity that allows us to measure the effective interfacial tension Γ_e, the two procedures are equally valid. For consistency, the data that we present in [30] were always obtained by measuring h directly on the interface profile, taking the difference between the average radius of the two heads of the drop (the average of the two maxima in the interface profile, x_1 and x_2) and the radius at the horizontal coordinate $x_M = \frac{x_1+x_2}{2}$, as shown in Fig. 3.4.

3.4 Origin of the dumbbell shape: background fluid recirculation

Dumbbell-shaped drops have been observed as early as in 1977, when Manning and Scriven observed that drops of water-hydrocarbon-surfactant systems assumed non ellipsoidal shapes when the interfacial tension was less then 10 µN/m [45]. Even though they did not report an explanation for this finding, they also observed a motion of the background fluid in the spinning capillary. Indeed, in an SDT experiment the background fluid is not at rest, but rather flows towards the center of the capillary at the center of the drop. This recirculating flow was further investigated by Currie and Van Nieuwkoop [44], and has lately been indicated as the possible cause of dumbbell shapes in SDT experiments [17], because the normal stress applied on the drop surface is higher at the drop center than at its edges. In order to verify this assumption and better understand the origin and time evolution of the drop shape, we numerically solve the Navier-Stokes equations in the background fluid, during rotation. The code used to this end is available at [46]. Our results are reported

in [47], and the aim of this section is to anticipate and give some further detail on the procedure we use.

As described by Currie and Van Nieuwkoop [44], the recirculating flow arises from the inhomogeneous pressure field in the spinning capillary. Even for the case of a drop immiscible with the background reservoir, the spinning capillary contains a region of lower pressure: the centripetal pressure depends on the fluid density as

$$P(r,x) = \int_0^r \rho(r',x)\omega^2 r' \mathrm{d}r' \,. \tag{3.3}$$

Since the drop has a lower density ρ_d than that of the background fluid ρ_e, a horizontal pressure gradient arises in correspondence to the drop heads, as schematically represented in Fig. SM1 of [47]. At the drop heads, the background fluid is subject to a pressure jump $\Delta P_\omega = \frac{1}{2}\Delta\rho\omega^2 r^2$ along the horizontal direction, with the consequent recirculating motion induced by such an inhomogeneity of the pressure field. In order to numerically solve the Navier-Stokes equations and gain insight on the fluid motion, we divided the pressure in a steady and an unsteady component, $p(x,r) = P(x,r) + p'(x,r)$. The former contains the centripetal forcing, including both the quadratic dependence in the radial direction r and the decrease along the horizontal direction x above the drop, while the latter is associated to the fluid motion. As described in [47], splitting the pressure field in two components is analogous to introducing a source term $\vec{F} = -\frac{1}{\rho}\nabla P$ in the momentum conservation equation. The flow of the background fluid can thus be described by:

$$\frac{\partial \vec{v}}{\partial t} + (\vec{v}\cdot\nabla)\vec{v} = -\frac{1}{\rho}\nabla p' + \nu\nabla^2\vec{v} + \vec{F} \,. \tag{3.4}$$

In [47] we numerically solve Eq. 3.4 in two dimensions (along the horizontal, x, and radial r, coordinates), together with the Poisson equation that is obtained by inserting in the momentum equation the continuity equation ($\nabla\cdot\vec{v} = 0$) for the incompressible background fluid. In particular, taking the divergence of the momentum equation in two dimensions x and r (so that $\vec{v} = u\hat{\imath} + v\hat{\jmath}$), and writing for the second term on the left hand side

$$\nabla\cdot\left[\left(u\frac{\partial}{\partial x} + v\frac{\partial}{\partial r}\right)(u\hat{\imath} + v\hat{\jmath})\right] = \frac{\partial u}{\partial x}\frac{\partial u}{\partial x} + \frac{\partial v}{\partial x}\frac{\partial u}{\partial r} + \frac{\partial u}{\partial r}\frac{\partial v}{\partial x} + \frac{\partial v}{\partial r}\frac{\partial v}{\partial r} \,,$$

one obtains the desired Poisson equation for pressure (in two dimensions):

$$\frac{\partial^2 p}{\partial x^2} + \frac{\partial^2 p}{\partial r^2} = -\rho\left[\left(\frac{\partial u}{\partial x}\right)^2 + 2\frac{\partial u}{\partial r}\frac{\partial v}{\partial x} + \left(\frac{\partial v}{\partial r}\right)^2\right] \,. \tag{3.5}$$

Once inserted the pressure field in the system (3.4-3.5), we iterate until the solution is stable.

For further use and completeness, we report here also the discretized version of Eqs. (3.4-3.5) that we used. By explicitly writing the source terms $\vec{F} = -\frac{1}{\rho}\nabla P$ in order to

differentiate $P(x,r)$, and by performing a central discretization of each term [48], one can calculate the velocity field at each time step $n+1$ as:

$$\begin{aligned} u_{i,j}^{n+1} = u_{i,j}^n - u_{i,j}^n \frac{\Delta t}{\Delta x}(u_{i,j}^n - u_{i-1,j}^n) - v_{i,j}^n \frac{\Delta t}{\Delta r}(u_{i,j}^n - u_{i,j-1}^n) + \\ - \frac{\Delta t}{\rho 2 \Delta x}(p_{i+1,j}^n - p_{i-1,j}^n) - \frac{\Delta t}{\rho 2 \Delta x}(P_{i+1,j}^n - P_{i-1,j}^n) + \\ + \nu \left[\frac{\Delta t}{\Delta x^2}\left(u_{i+1,j}^n - u_{i,j}^n + u_{i-1,j}^n\right) + \frac{\Delta t}{\Delta r^2}\left(u_{i,j+1}^n - u_{i,j}^n + u_{i,j-1}^n\right) \right] \end{aligned} \tag{3.6}$$

$$\begin{aligned} v_{i,j}^{n+1} = v_{i,j}^n - u_{i,j}^n \frac{\Delta t}{\Delta x}(v_{i,j}^n - v_{i-1,j}^n) - v_{i,j}^n \frac{\Delta t}{\Delta r}(v_{i,j}^n - v_{i,j-1}^n) + \\ - \frac{\Delta t}{\rho 2 \Delta r}(p_{i,j+1}^n - p_{i,j-1}^n) - \frac{\Delta t}{\rho 2 \Delta r}(P_{i,j+1}^n - P_{i,j-1}^n) + \\ + \nu \left[\frac{\Delta t}{\Delta x^2}\left(v_{i+1,j}^n - v_{i,j}^n + v_{i-1,j}^n\right) + \frac{\Delta t}{\Delta r^2}\left(v_{i,j+1}^n - v_{i,j}^n + v_{i,j-1}^n\right) \right] \end{aligned} \tag{3.7}$$

$$\begin{aligned} p_{i,j}^n = \frac{(p_{i+1,j}^n + p_{i-1,j}^n)\Delta r^2 + (p_{i,j+1}^n + p_{i,j-1}^n)\Delta x^2}{2(\Delta x^2 + \Delta r^2)} + \\ + \frac{\rho \Delta x^2 \Delta r^2}{2(\Delta x^2 + \Delta r^2)} \left[\frac{1}{\Delta t}\left(\frac{u_{i+1,j}^n - u_{i-1,j}^n}{2\Delta x} + \frac{v_{i,j+1}^n - v_{i,j-1}^n}{2\Delta r} \right) + \right. \\ \left. - \left(\frac{u_{i+1,j}^n - u_{i-1,j}^n}{2\Delta x} \right)^2 - 2\frac{u_{i,j+1}^n - u_{i,j-1}^n}{2\Delta r}\frac{v_{i+1,j}^n - v_{i-1,j}^n}{2\Delta x} + \left(\frac{v_{i,j+1}^n - v_{i,j-1}^n}{2\Delta r} \right)^2 \right] \end{aligned} \tag{3.8}$$

Here u and v are the horizontal and radial component of the velocity, the superscript indicates the time step of the iteration, and the subscripts i, j run over the discretized variables x and r in the horizontal and radial direction, respectively. Δx, Δr and Δt are the space and time discretization intervals ($\Delta x = \Delta r = 0.1$, with x and r ranging from 0 to 4 and from 0 to 2, respectively).

The results of such a numerical solution are reported in [47]: the recirculating motion of the background fluid does indeed depend on the pressure jump ΔP_ω at the drop heads. In particular, the difference between the radial component of the velocity field at the drop center and at the heads depends linearly on ΔP_ω. Therefore, the extra normal stress exerted on the drop surface that induces the dumbbell shape depends on ΔP_ω as well. We exploit this result in [30] to compute the total stress on the drop and to measure the effective interfacial tension from the time evolution of dumbbell-shaped drops and the velocity of radial deformation. Reference [47] reports the results of such an analysis on the motion of the background fluid for a specific drop length and radius, at various angular velocities and values of the density mismatch between the drop and background fluid, but the same behaviour is maintained when the drop size is varied.

PHYSICAL REVIEW FLUIDS **5**, 074001 (2020)

Editors' Suggestion

Ultralow effective interfacial tension between miscible molecular fluids

Alessandro Carbonaro,* Luca Cipelletti, and Domenico Truzzolillo
Laboratoire Charles Coulomb (L2C), UMR 5221 CNRS-Université de Montpellier, Montpellier, France

(Received 21 March 2020; accepted 4 June 2020; published 10 July 2020)

We exploit the deformation of drops spinning in a denser background fluid to investigate the effective interfacial tension (EIT) between miscible molecular fluids. We find that, for sufficiently low interfacial tension, spinning drops develop dumbbell shapes, with two large heads connected by a thinner central body. We show that this shape depends not only on the density and viscosity contrast between the drop and background fluids, but also on the fluid molecular structure, and hence on the stresses developing at their interface due to a different molecular interaction. We systematically investigate the dynamics of dumbbell-shaped drops of water-glycerol mixtures spinning in a pure glycerol reservoir. By developing a model for the deformation based on the balance of the shear stress opposing the deformation, the imposed normal stress on the drop, and an effective interfacial tension, we exploit the time evolution of the drop shape to measure the EIT. Our results show that the EIT in water-glycerol systems is orders of magnitude lower than that reported in previous experimental measurements, and in excellent agreement with values calculated via the phase field model proposed by Truzzolillo *et al.* [Phys. Rev. X **6**, 041057 (2016)].

DOI: 10.1103/PhysRevFluids.5.074001

I. INTRODUCTION

Interfacial tension between immiscible fluids is a well-defined, well-known quantity of paramount importance in a wide range of phenomena, from soft matter and material science to biophysics, oil recovery and multiphase flow [1]. By contrast, the presence of capillary stresses at the interface between miscible fluids is still debated and actively investigated. For miscible fluids, equilibrium thermodynamics states that interfacial tension should not exist, the equilibrium state being a homogeneous mixture of the fluids. However, transient capillary stresses between miscible fluids were first postulated in 1901 by Korteweg, who asserted that stresses due to density (or composition) gradients in a multifluid system could act as an effective interfacial tension (EIT) [2]. Following his work, one can write the EIT, hereinafter denoted by Γ_e, similarly to the tension at equilibrium between immiscible fluids, i.e., by expanding the mixing free energy in even powers of the concentration gradient $\nabla\tilde{\varphi}$ [3]. By considering only the first term of this expansion, Γ_e can be written as

$$\Gamma_e = \int_{-\infty}^{+\infty} \kappa(\tilde{\varphi})(\nabla\tilde{\varphi})^2 dz. \tag{1}$$

Here $\tilde{\varphi}$ is the space-dependent volume fraction of one of the two fluids, z is the coordinate orthogonal to the interface, and $\kappa(\tilde{\varphi})$ is the so-called Korteweg parameter, embedding the effect of the specific interaction between the fluids [4,5]. Clearly, Γ_e tends to zero with time t, as diffusion smears out the interface, whose thickness increases, reducing $\nabla\tilde{\varphi}$ with t [6]. Such a transient, out-of-equilibrium interfacial tension has been invoked in literature to rationalize the behavior of miscible fluids at short

*alessandro.carbonaro@umontpellier.fr

times, before they are fully mixed, and several works tried to elucidate the role of stresses at miscible boundaries, both theoretically [7–12] and experimentally. Among the strategies adopted to measure the EIT between miscible fluids, the most recent ones leverage on the study of hydrodynamic instabilities [5,13], on light scattering experiments probing capillary waves [6,14], and on the observation of the shape of drops and threads under an external forcing [15–17]. Despite this effort, the magnitude and even the very existence of EIT between simple molecular fluids is still debated and mostly unclear.

One technique to measure very low interfacial tensions (10^{-3}–10^{-2} mN/m [18,19]) is spinning drop tensiometry (SDT), which is based on the observation of drop shapes. In an SDT experiment a drop is injected in a denser background fluid contained in a cylindrical capillary. When the capillary is spun, the drop elongates on the axis of rotation due to centrifugal forces. Following the drop shape by means of video imaging, one can then measure the interfacial tension between the drop and the background fluid. In the case of immiscible fluids, for which SDT was initially conceived by Vonnegut [20], one typically measures the equilibrium shape of the drop, which is dictated by the balance between surface tension and centripetal forces. The interfacial tension Γ is then obtained through the Vonnegut equation [20]:

$$\Gamma = \frac{\Delta\rho\omega^2 r^3}{4}, \tag{2}$$

where $\Delta\rho$ is the density difference between the background and drop fluids, ω the angular velocity, and r the equilibrium radius of the drop. A second possibility is to characterize the time evolution of the drop after a sudden rotational speed jump. Recently, we have employed this technique to study the elongation dynamics of drops, both in miscible and immiscible background fluids [16], showing that the drop dynamics towards an equilibrium state are characterized by a relaxation time fully determined by (i) the viscosity of the fluids, (ii) the drop size, and (iii) the interfacial tension. In the past few decades, SDT experiments aiming at characterizing equilibrium states and diffusion processes have been performed by several groups to investigate the presence and the relevance of an EIT between miscible fluids, either close to [15,21] or far from a spinodal decomposition of the fluids [22,23]. Unfortunately, in the case of fully miscible molecular liquids, such as water and glycerol, diffusion hampers the measurement of stationary states and literature data are conflicting, sometimes even in experiments by the same authors [23,24]. Indeed, when Γ is negligible a stationary state is never attained, as we showed for one specific pair of miscible fluids with small compositional mismatch, namely a drop of a water-glycerol mixture (5 wt % H_2O) spinning in pure glycerol. As a result, the question of whether an EIT exists or not in such a case has not been settled yet.

SDT experiments at low Γ are furthermore complicated by the fact that drops do not always maintain a simple ellipsoidal shape. Even for immiscible fluids, for sufficiently low interfacial tensions, they can develop a "dumbbell" or "dog-bone" shape consisting of two large heads connected by a thinner central body, as reported in the case of water-hydrocarbon-surfactant systems with $\Gamma < 10\ \mu$N/m [25]. In this case a satisfactory explanation of the phenomenon is still lacking. More recently [22], such shapes have been also observed in miscible fluids and have been attributed to the effect of perturbation due to viscous secondary flows in finite reservoirs of rotating fluids. Such an effect, till now unexplored, is the focus of the present work.

To set the scene, Fig. 1 shows examples of such dumbbell shapes for drops rotating in a pure glycerol reservoir. Drops in panels A and C are composed of mixtures of water and glycerol, respectively with water mass concentration $c_w = 0.75$ and $c_w = 0.20$, whereas the drop in panel B is made of triethylene glycol (TEG). All drops are fully miscible with the glycerol background. Strikingly, Fig. 1 shows that the development of a dumbbell shape depends not only on the density and viscosity contrast with respect to the background fluid, but also on the molecular structure of the fluids. Indeed, in absence of any interfacial stresses, the TEG drop should have an intermediate shape between drops in panels A and C, since it has intermediate density and viscosity. This is evidently not the case; consequently, Fig. 1 cannot be explained only by means of hydrodynamic

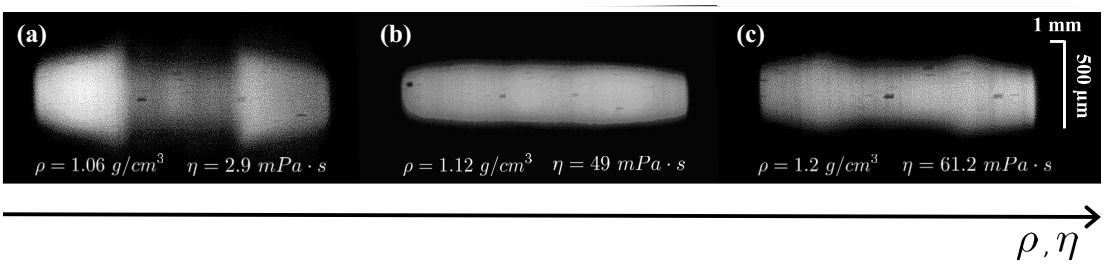

FIG. 1. Dyed drops containing 75% H_2O–25% glycerol (panel A), TEG (panel B), and 20% H_2O–80% glycerol (panel C). All drops spin in a reservoir of pure glycerol. Images are optically compressed in the horizontal direction and expanded in the vertical direction to improve resolution, as detailed in the main text (Sec. II).

arguments. Thus, characterizing the evolution of such drop shapes appears to be a promising strategy to measure the effect of interfacial stresses between the drop and background fluids. In this work, we tackle this challenging task and investigate experimentally the time evolution and the origin of dumbbell-shaped drops by systematically varying the composition of the drop fluid in a series of SDT experiments. Furthermore, we exploit fluorescent drops to track the time evolution of the full concentration profile of the fluids in the capillary, instead of simply measuring the intensity profile of the collected light. We model the temporal dynamics of the drop shape by balancing the normal stress imposed on the drop surface, the shear stress opposing the deformation, and the effect of an EIT, and we exploit the deformation dynamics to measure the effective interfacial tension between miscible molecular fluids.

The rest of the work is organized as follows. In Sec. II we present the setup and materials employed, and elucidate the procedure to extract the concentration profile of the fluids in the capillary. In Sec. III we present the data on the deformation dynamics of drops, discussing our results in the light of a model allowing one to measure Γ_e. Finally, in Sec. IV we make some concluding remarks and summarize the key results of our work.

II. MATERIALS AND METHODS

Glycerol ($\geqslant$99.5 wt %) was purchased from Sigma Aldrich and used as received. Water-glycerol mixtures were prepared using Milli-Q ultrapure water, with densities ρ and viscosities η reported in Table I as a function of water mass fraction c_w, for $T = 25.0 \pm 0.5\,^\circ$C. The water mass fraction was determined via rheological measurements as detailed in Table I. Fluorescein (disodium salt) was purchased from Merck KGaA and dissolved in the drop fluids at two concentrations, 2×10^{-3} wt/wt and 10^{-3} wt/wt, for two independent sets of measurements as detailed later. Experiments were performed with a Krüss spinning drop tensiometer at $25.0 \pm 0.5\,^\circ$C, with rates of rotation ranging from 6000 to 15 000 rpm, so that buoyancy could be neglected. All drops were injected with a 1 μl syringe in a capillary with an internal diameter of 3.25 mm, prefilled with glycerol before each experiment. The time between the injection and the beginning of the rotation was typically 10–15 seconds. After each measurement, the fluids were replaced and a fresh new drop was injected in the capillary. To image the drops, the tensiometer is equipped with a blue LED with dominant wavelength of 469 nm for illumination and a CMOS camera (Toshiba Teli BU406M) for imaging. Since the drops become very elongated, we use as an objective two cylindrical lenses (Newport CKX17-C) that expand the field of view in the horizontal direction x and compress it in the vertical direction y. As described in [16], the resulting magnification in the x (horizontal) direction is $M_x = 0.3$, while the magnification in the y (vertical) direction is $M_y = 3.36$. The different horizontal and vertical magnifications allow one to follow the dynamics of very elongated drops along almost all the capillary length (5 cm), while gaining at the same time in accuracy along the vertical direction.

TABLE I. Densities and viscosities of the water-glycerol mixtures used in the experiments.

Liquid	ρ (g/cm^3)[a]	η (mPa s)[b]
Glycerol[c] ($c_w \leqslant 0.02$)	1.26 ± 0.01	800.0 ± 0.1
$c_w = 0.25$	1.19 ± 0.01	33.8 ± 0.1
$c_w = 0.45$	1.12 ± 0.01	9.0 ± 0.1
$c_w = 0.70$	1.07 ± 0.01	2.8 ± 0.1
$c_w = 0.75$	1.06 ± 0.01	2.3 ± 0.1
$c_w = 0.90$	1.02 ± 0.01	2.2 ± 0.2
Water[d]	0.996 ± 0.001	0.89 ± 0.01

[a]Densities of water-glycerol mixtures were obtained from tabulated values [26] corresponding to mixtures having the measured zero-shear viscosities.
[b]The viscosities of water-glycerol mixtures and pure glycerol were measured by performing steady rate rheology experiments using a stress-controlled AR 2000 rheometer (TA Instruments) with a steel cone-and-plate geometry (cone diameter = 50 mm, cone angle = 0.0198 rad). No dependence of the viscosity on the shear rate was observed as all samples showed pure Newtonian response.
[c]The viscosity of the glycerol used as the background fluid is lower than that tabulated for anhydrous glycerol [26] because of the unavoidable adsorption of water from the atmosphere.
[d]The viscosity and the density of water were measured using a rolling-ball Anton Paar Lovis 2000ME microviscosimeter and a DMA 4500M densimeter, respectively.

Following the magnification stage, a blue light filter in front of the CMOS eliminates the blue background light.

A. Concentration profiles

An example of the optically compressed images of the drops obtained with the experimental setup is shown in Fig. 2(a), displaying the typical time evolution of a drop of pure water spinning in pure glycerol. A further step is required to follow more precisely the evolution of the interface. To this end, we extract the concentration profile of the drop fluid from the fluorescence intensity, in order to define precisely the drop boundary. Note that, strictly speaking, the fluorescence signal

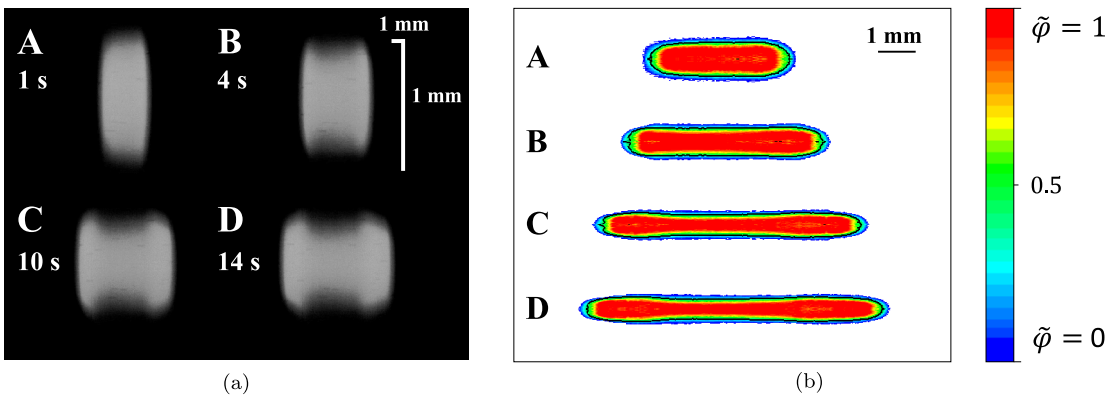

FIG. 2. (a) Time evolution of the fluorescence intensity recorded for a typical drop of pure water in a pure glycerol background. Note the different magnification in the horizontal and vertical directions. (b) Concentration profiles reconstructed from the fluorescence intensity images of panel (a), as detailed in the text. In panel (b), the scale is the same in the horizontal and vertical directions. The black line represents the drop surface, defined as the set of points where $\tilde{\varphi}(x, r) = 0.5$.

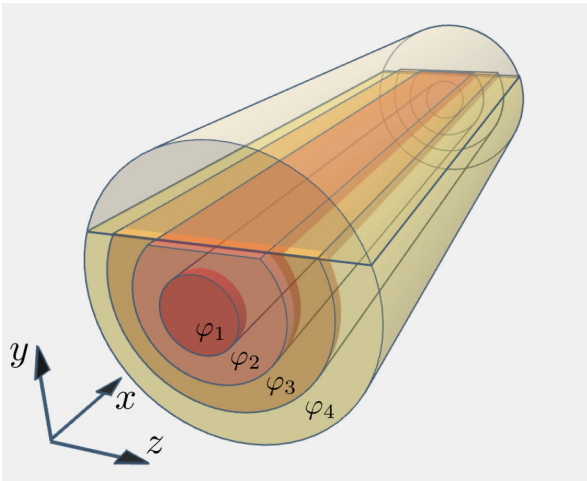

FIG. 3. Scheme of the drop for the inversion routine to retrieve the concentration profile from the fluorescence intensity. We typically use $N = 204$ shells; for clarity, only the first four shells are shown here. The fluorescence intensity distribution generally varies along the x direction, yielding an x-dependent concentration profile for the drop fluid $\tilde{\varphi}(x, r)$.

comes from the spatial distribution of fluorescein, not that of the drop fluid. However, over the timescale of our experiments (∼10 s) we assume the concentration profile of fluorescein to closely follow the one of the drop fluid, since there is not enough time to develop an appreciable difference in distribution of the two components. To support this claim, we compare the diffusion coefficients of water (the drop fluid) and of fluorescein in the background glycerol. The self diffusion coefficient of water is $D_w = 1.025 \times 10^{-9}$ m^2/s and the diffusion coefficient of water in glycerol is $D_{wg} = 1.4 \times 10^{-11}$ m^2/s [27]. On the other hand, the diffusion coefficient of fluorescein in water is $D_{fw} = 6.4 \times 10^{-10}$ m^2/s [28]. We estimate the diffusion coefficient of fluorescein in glycerol as $D_{fg} \simeq D_{fw}\frac{D_{wg}}{D_w} \simeq 8.7 \times 10^{-12}$ m^2/s. Therefore, the difference between the distances over which water and fluorescein may diffuse over the time scale of our experiments is $l_w - l_f \approx 3$ μm, much smaller than the resolution with which we measure the drop shape, which we determine to be a few tens of μm. Consequently, we can safely assume the concentration profile of the fluorophore to represent well that of the drop fluid. Furthermore, by changing the concentration of fluorophore over more than one decade (from 1×10^{-4} wt/wt to 2.5×10^{-3} wt/wt), we tested that the concentration of fluorescein is directly proportional to the light intensity collected.

These considerations, together with an additional symmetry argument, allow linking the intensity of the collected light to the x dependent radial concentration profile of the drop fluid. Exploiting the cylindrical symmetry of the drops, one can move from a bidimensional intensity image to a three-dimensional concentration map.

In order to do so, we divide the drop into N concentric cylindrical shells of radius r_i and constant thickness dr, each of them having a local value of water volume fraction $\tilde{\varphi}_i$ (see Fig. 3). The fluorescence intensity at a given horizontal coordinate x and vertical coordinate y is be given by the sum over the contributions of each shell, weighted by a geometric factor c_i proportional to the length of the chord that traverses such shell at coordinate y, along the z direction, i.e., the line of sight.

Accordingly, the intensity distribution reads

$$I(x_k, y_j) = \sum_{i=1}^{N} c_i(y_j)\tilde{\varphi}_i(x_k), \tag{3}$$

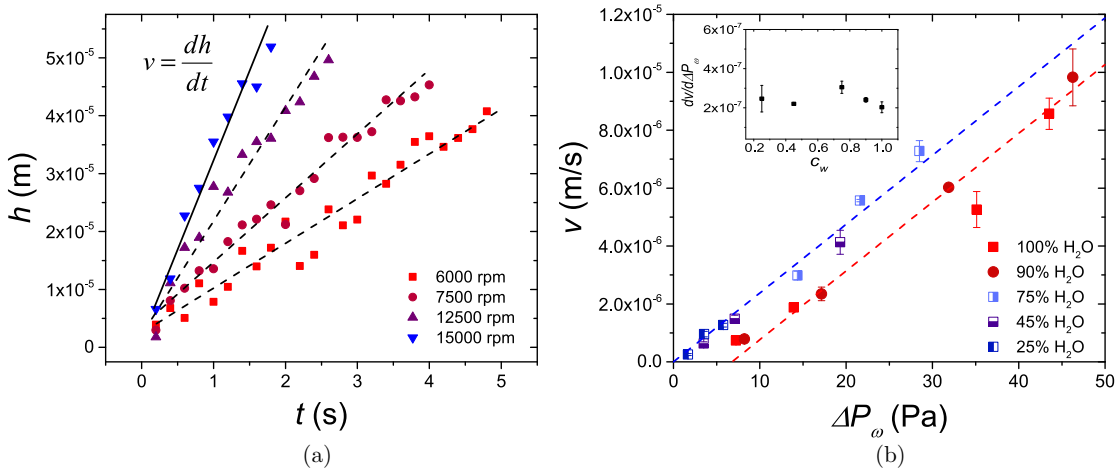

FIG. 4. (a) Time evolution of the deformation amplitude h for a drop of pure water in a pure glycerol background, at different ω as shown by the labels. (b) Deformation velocity as a function of the centripetal forcing, for various water mass fractions in the drop. The inset shows the slope of the velocity versus ΔP_ω, obtained by fitting independently datasets at a given c_w with a straight line.

where the indexes k and j have been introduced to account for the discretization of I on the pixel grid of the CMOS camera. For a given x_k, one can recast the problem in the matrix form

$$\mathbf{I} = \mathbf{C}\tilde{\varphi}, \tag{4}$$

with $\mathbf{I} = \{I_j\}$, $\mathbf{C} = \{c_{ji}\}$, and $\tilde{\varphi} = \{\tilde{\varphi}_i\}$; and $I_j \equiv I(x_k, y_j)$, $c_{ji} \equiv c_i(y_j)$, and $\tilde{\varphi}_i \equiv \tilde{\varphi}_i(x_k)$. For each k, the solution is thus $\tilde{\varphi} = \mathbf{C}^{-1}\mathbf{I}$. This procedure is mathematically equivalent to calculating a discrete version of the inverse Abel transform of the intensity distribution of the fluorescent light. Furthermore, the inversion of the matrix $\mathbf{C}$ is sped up by exploiting the symmetry of the drop around the longitudinal axis, which translates into the condition that $\mathbf{C}$ is lower-diagonal. By solving Eq. (4) for all x_k of interest, one obtains the concentration map of the the drop fluid in the capillary, as shown in Fig. 2(b). We use the maps to define the drop surface as the set of points where $\tilde{\varphi}(x, r) = 0.5$, with $\tilde{\varphi}(x, r)$ normalized to unity in the region of the drop close to the axis of rotation. The amplitude h of the drop deformation is defined as the difference between the maximum radius of the drop, close to the tips, and the minimum radius, at the center of the drop (see Fig. 5 below).

III. RESULTS AND DISCUSSION

We characterize the evolution of the drops towards a dumbbell shape by observing the time evolution of the deformation amplitude h, varying systematically the drop composition. Figure 4(a) shows the time evolution of h for a drop of pure water in pure glycerol, for various rotational speeds. Time $t = 0$ corresponds to the onset of the deformation, shortly after the start of rotation. At short time the deformation amplitude increases linearly with time, with a velocity $v = \frac{dh}{dt}$ that depends on the rotation speed. This dependence on ω stems from the fact that spinning drops are subject at the head of the drop to a rotation-induced pressure jump $\Delta P_\omega = \frac{1}{2}\Delta\rho\omega^2 r^2$ [16,29], where $\Delta\rho$ is the density difference between the denser background fluid and the drop and r the drop radius. This pressure jump ΔP_ω induces the drop elongation in first place, but it is also responsible for a secondary flow of the background fluid that leads to the dumbbell shape, as we shall detail below. Figure 4(b) reports the radial deformation velocity as a function of ΔP_ω, for various concentrations of water in the drops.

It is worth underlining two features. First, the velocity of the radial deformation is approximately a linear function of ΔP_ω, with a slope that is essentially independent of the concentration of water in the drop, as shown in the inset of Fig. 4(b). Second, even before trying to rationalize the dependence

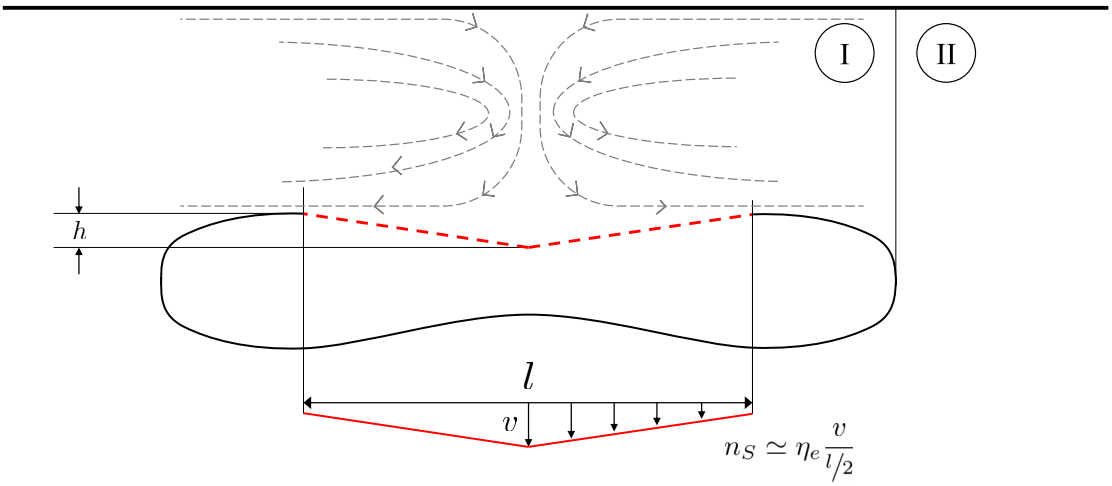

FIG. 5. Scheme of the drop deformation. The dashed arrows show the secondary flow of the background fluid induced by the capillary rotation.

of v on ΔP_ω, it appears clearly that the data may be divided in two main families. All data for drops with a mass concentration of water $c_w \leqslant 0.75$ are compatible with a straight line through the origin. By contrast, data from drops with $c_w = 0.9$ and $c_w = 1$ show a different behavior in that a linear fit of $v(\Delta P_\omega)$ displays a negative intercept with the v axis. This is counterintuitive if we were to neglect interfacial tension: drops containing a larger fraction of water, being less viscous, should be deformed more rapidly for a given centripetal forcing. Thus, the negative intercept of data for $c_w \geqslant 0.9$ strongly suggests a nonvanishing EIT for these systems. As a first step towards the modeling of our experiments, we perform a linear fit of two families of data in Fig. 4(b), for water concentrations up to $c_w = 0.75$ and above $c_w = 0.9$, respectively:

$$v = A\Delta P_\omega + B, \tag{5}$$

finding an R^2 value of 0.98 and 0.97 respectively, keeping the slope A the same for the two data families. The physical meaning of the terms A and B will be detailed later; however, we anticipate that B depends on the concentration c_w of water in the drop and hence on the EIT. It is thus crucial to perform a statistical analysis of the data of Fig. 4(b) in order to assess whether the difference in the offset B between data below and above $c_w = 0.9$ (semifilled and solid symbols, respectively) is statistically significant, or just due to experimental noise.

We perform a t test [30,31] on the difference between term B of the fit for the two data families, for $c_w \leqslant 0.75$ and $c_w \geqslant 0.9$. As detailed in [32], for the data of Fig. 4(b) the Student t distribution yields a value of the standardized variable $t = 6.43$. This is much larger than $t_{0.995} = 2.95$, the edge of the 1% confidence interval for a two-tailed t distribution with $N_1 + N_2 - 2 = 15$ degrees of freedom, where $N_1 = 9$ and $N_2 = 8$ are the numbers of data points in the two datasets. Hence we conclude that the difference between the B parameter for the two datasets in Fig. 4(b) is statistically significant, with a confidence level greater than 99%.

A. Model of the radial deformation and EIT

Having checked that the effect of the EIT on the data of Fig. 4(b) is statistically significant, we propose a simple model to rationalize the data and extract from them Γ_e. The model is based on the balance of all sources of stress on the drop interface at the onset of the deformation. Similarly to the approach by Lister and Stone in [29], we write an equilibrium equation for the stresses on the drop surface, at the center of the drop:

$$n_E = n_S + n_L, \tag{6}$$

where n_E is the normal stress inducing the deformation and n_S and n_L are the normal stresses opposing the deformation, with n_S the shear stress arising from the motion of the drop and background fluids and n_L a Laplace-like term that takes into account the effect of the EIT. Since in our experiments the viscosity η_e of the external background fluid is much higher than the viscosity η_d of the drop fluid, the shear stress can be approximated as $n_S \simeq 2\eta_e v/l$, where l is the distance over which the radial deformation develops as shown in Fig. 5. The Laplace-like term n_L is estimated as the difference between the Laplace pressure jump at the heads of the drop and that at the central body. At the onset of the deformation, the drop shape is well described by a cylinder with radius r_0 capped by two hemispheres. Consequently, the hemispherical heads and the cylindrical body will be characterized by a pressure jump with respect to the background fluid of $2\Gamma_e/r_0$ and Γ_e/r_0 respectively, leading to $n_L = \Gamma_e/r_0$, where Γ_e is the EIT.

The normal stress n_E inducing the deformation and arising from the external forcing on the drop deserves a further discussion. When investigating the limits of the SDT technique, as early as in 1982, Currie and Van Nieuwkoop observed that in any spinning capillary the background fluid is not at rest, but rather flows towards the axis of the capillary at the center of the drop, thus inducing an extra normal stress on the drop surface [25,33]. This secondary recirculating flow pushing on the drop surface originates from the jump in centripetal pressure at the drop head, between regions I and II in Fig. 5. The origin of this jump is easily understood by recalling that the hydrostatic pressure induced by the rotational acceleration is proportional to the fluid density, which is smaller in the drop as compared to the background fluid. By numerically solving the Navier-Stokes equations [34], we verified that this secondary flow gives rise to a velocity field with a radial component directly proportional to ΔP_ω [32]. Since the external forcing on the drop originates from the secondary recirculating flow and the latter is proportional to ΔP_ω, we write $n_E = \alpha \Delta P_\omega$ with α a positive constant.

Equation (6) can then be rewritten as

$$\alpha \Delta P_\omega - \frac{2\eta_e v}{l} - \frac{\Gamma_e}{r_0} = 0, \tag{7}$$

which yields for the radial deformation velocity

$$v = \frac{\alpha l}{2\eta_e}\Delta P_\omega - \frac{\Gamma_e l}{2 r_0 \eta_e}, \tag{8}$$

i.e., the linear form introduced empirically in Eq. (5). Note that for miscible fluids Γ_e decreases over time, such that Eq. (8) holds only for short times after the onset of the radial deformation, well before diffusion smears out the interface. For this reason, we measure the dynamics of the drop deformation only for a few seconds, before diffusion becomes significant.

Albeit simple, Eq. (8) allows all the main features of the experimental data of Fig. 4(b) to be rationalized: the velocity of the radial deformation at the onset of the instability varies linearly with the centripetal forcing ΔP_ω, with a prefactor that does not depend on the specific parameters of the drop fluid, namely its viscosity and water concentration c_w. Furthermore, Eq. (8) contains an offset proportional to Γ_e, which for miscible fluids is expected to depend on the concentration gradient according to Eq. (1), and thus to be more significant at the highest c_w. This explains why the data for $c_w \geqslant 0.9$ in Fig. 4(b) are not compatible with a line passing through the origin. Figure 6(a) shows a master curve obtained by fitting each dataset at a given water concentration with Eq. (8) and then rescaling the data using the parameters resulting from the best fit, by defining the scaled variables $v' = (v\frac{r_0}{l} + \frac{\Gamma_e}{2\eta_e})\frac{2\eta_e}{\alpha}$ and $P' = r_0 \Delta P_\omega$. In this representation, the data should fall on the straight line $v' = P'$. Figure 6 shows that within experimental error this is indeed the case, and that the results do not depend on the fluorescein concentration.

The values of Γ_e used to rescale the data in Fig. 6(a) are shown in Fig. 6(b) as a function of the volume fraction ϕ and mass fraction c_w of water in the drop, where solid and open symbols refer to two concentrations of fluorescein. It is worth emphasizing the ultralow value of the EIT, which attains at most 250 ± 50 nN/m for pure water drops in pure glycerol. This value is much lower

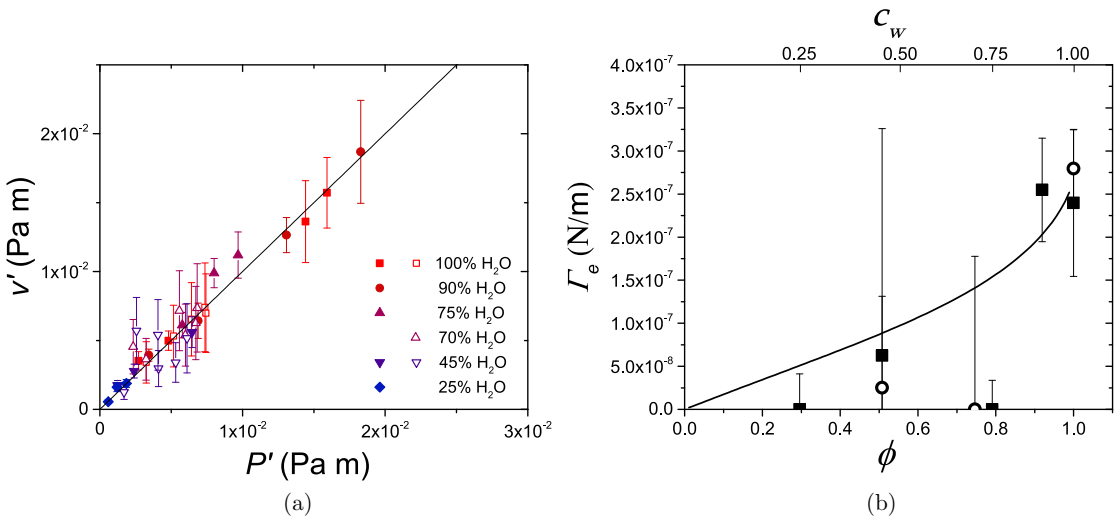

FIG. 6. (a) Mastercurve of the data of Fig. 4(b), obtained by using the scale variable introduced in the text. (b) Experimental values of Γ_e used to rescale the data in panel (a) as a function of the water volume fraction ϕ (bottom axis) and the correspondent water mass fraction c_w (top axis) in the drop. The black line is the theoretical prediction for Γ_e [Eq. (10)], discussed in the text. In both panels, solid (open) points refer to measurements with fluorescein concentration 2×10^{-3} wt/wt (10^{-3} wt/wt).

than that previously reported in literature [23]. Our findings solve the longstanding controversy stemming from conflicting literature values for the same system [23,24,35], as mentioned in Sec. I. In particular, our result is in stark contrast with the value of EIT between water and glycerol reported in [23], $\Gamma_e = 0.58$ mN/m. Note that this latter value is also in contrast with the experimental observation that drops of pure water spinning in glycerol keep on elongating without reaching a stationary state, even in experiments lasting thousands of seconds. If the EIT was as high as reported in [23], a drop of water in glycerol would deform towards a stationary state following an exponential relaxation with time constant $\tau \simeq 1.4$ s, estimated following Ref. [16] and assuming a relaxation dynamics similar to that of drops spinning in an immiscible background fluid. This is clearly not the case. By contrast, the ultralow magnitude of the EIT measured here (a few hundreds of nN/m) is consistent with several works [24,36,37] that report a negligible EIT for the same system.

A further support to our findings comes from a review of previous works investigating the Saffman-Taylor instability occurring when water is injected in a Hele-Show cell containing glycerol. Although a Saffman-Taylor instability does occur a few ms after the injection of the less viscous fluid (water) into a Hele-Shaw cell and hence reduces the effects of diffusion, its visualization has systematically suggested that viscous dissipation largely dominates over interfacial effects. In this limit, the wavelength of the instability λ_{ST} is only dictated by the gap of the injection cell b, and is expected to satisfy

$$4b \lesssim \lambda_{ST} \lesssim 5b. \tag{9}$$

Previous works by Paterson [35] and more recently by Bischofberger and coworkers [36] and Lajeunesse and coworkers [37] systematically find λ_{ST} values in this regime, thus suggesting that the EIT between water and glycerol is too low to be measurable through the Saffman-Taylor instability. To corroborate this notion, we use Eq. (9) to extract a lower bound for the Γ_e values measurable with this technique [38,39], which we quantify as the EIT for which the wavelength observed at the onset of the instability equals $4b$. We show in [32] that this lower bound for water-glycerol systems in a typical Hele-Show cell and for accessible injection rates is approximately 0.1 mN/m, while the measurement of much lower values is hampered by diffusion.

By contrast, the analysis of the radial deformation of drops towards dumbbell shapes proposed here allows one to measure EIT values as low as hundreds of nN/m, well beyond the limits of any other standard experimental technique. The strength of the method proposed in this work resides in the fact that the forcing $\alpha\Delta P_\omega$ is very weak, thus allowing relatively low values of the capillary (Ca) and the Bond (Bo) numbers to be reached. The first is defined as the ratio between viscous forces and surface tension forces acting across the interface between the fluids: $\mathrm{Ca} = \frac{\eta v}{\Gamma}$. Considering the viscosity of the background fluid (glycerol), the measured deformation speed v and Γ_e, the capillary numbers characterizing our experiments are in the range $2 \lesssim \mathrm{Ca} \lesssim 20$, which are relatively low, taking into account that we probe miscible interfaces and hence Γ_e is very small. The second dimensionless number relevant for our experiments is the Bond number, the ratio of the external forces to surface tension forces: $\mathrm{Bo} = \alpha\Delta P_\omega r_0/\Gamma_e$. In our case, $0.4 \lesssim \mathrm{Bo} \lesssim 4$, corroborating a scenario where capillary stresses are indeed relevant for the drop deformation. The estimates for Ca and Bo also explain the large uncertainty on the value of Γ_e at $\varphi < 0.9$ in Fig. 6(b): when the EIT decreases to extremely low values, both the capillary and the Bond number increase well above unity, making Γ_e barely measurable.

In order to further validate our measurements, we calculate the expected EIT between water and glycerol using a phase field model introduced in [5]. We briefly recall the main ingredients of the model: by assuming local equilibrium between the two fluids [40–42], one computes both the enthalpic and the entropic contributions to the Korteweg parameter $\kappa(\tilde{\varphi})$ using lattice theory arguments and assuming for simplicity that the mixture is symmetric, i.e., that the two fluids have the same molecular volume. The two terms are due, respectively, to the variation of the internal energy density u and to the decrease of configurational entropy density s in the region where $|\nabla\tilde{\varphi}| > 0$. They are obtained by expressing u and s as a function of the local concentration, assuming a concentration gradient across three adjacent lattice layers orthogonal to the z direction, and finally by expanding the local concentration around that of the central layer, up to second order in the spatial derivatives of $\tilde{\varphi}$. Furthermore, in analogy to equilibrium systems, the local concentration profile is modeled by $\tilde{\varphi} = \frac{\phi}{2} + \frac{\phi}{2}\tanh(\frac{z}{\delta})$, with ϕ the volume fraction of one kind of molecules, e.g., water, in the bulk fluids. As detailed in Ref. [5], the model predicts

$$\Gamma_e = \frac{RTa^2}{V_m\delta}\left\{\chi_{wg}\frac{\phi^2}{6} + \frac{2}{3}\left[1 + \frac{1-\phi}{\phi}\ln(1-\phi)\right]\right\}, \tag{10}$$

with R the ideal gas constant, a and V_m the diameter and the molar volume of the fluid molecules respectively, and δ the interface thickness. The first term on the right-hand side of Eq. (10), proportional to the χ_{wg} parameter characterizing the interaction between water and glycerol molecules, quantifies the energy penalty (or gain) due to a local compositional inhomogeneity. The second term is always positive and depends only on ϕ. It quantifies the entropy loss due to the (transient) gradient of concentration. We note that the approximations used to derive Eq. (10) imply that the concentration gradient at the interface is small, such that the effective interfacial tension is dominated by the first term of the mixing free energy expansion, i.e., the square gradient one.

To estimate Γ_e for our water-glycerol mixtures we use Eq. (10) and take the average of the molecular diameter and molar volume of water and glycerol: $\langle a\rangle = 0.45$ nm and $\langle V_m\rangle = 45.5$ ml/mol. We further consider the effect of diffusion by calculating the thickness of the interface as $\delta = \sqrt{2D_{wg}t}$ where $D_{wg} = 1.4 \times 10^{-11}$ m^2/s is the diffusion coefficient of water in glycerol [27] and $t \approx 15$ s is the typical time elapsing between the drop injection and the observation of the instability. The result is displayed in Fig. 6(b) (line), showing that our data are very well captured by the theoretical Γ_e obtained via Eq. (10), with no adjustable parameter. The agreement between the data and Eq. (10) suggests that the model of Ref. [5], albeit very simple, may be reliably used to estimate the EIT. Since $-1 < \chi < 1$ for most pairs of miscible substances [43], for $\phi \simeq 1$ the effective interfacial tension between miscible molecular fluids is well approximated by

$$\Gamma_e \approx \frac{2RTa^2}{3V_m\delta}. \tag{11}$$

As an example, for liquids with characteristics similar to water ($a \approx 0.1$ nm, $V_m = 18$ ml/mol, $D = 1.025 \times 10^{-9}$ m^2/s [27] at $T = 298.15$ K), Eq. (11) predicts a tension ranging from $\Gamma_e \approx 13$ mN/m to $\Gamma_e \approx 20 \times 10^{-6}$ mN/m as the interface thickness increases from a value comparable to the molecular size ($\delta \approx a$ for $t = 0$) to 45 μm after $t = 1$ s of interdiffusion. This supports the fact that for fully miscible low-viscosity fluids capillary effects decay very rapidly with time and can be safely neglected in most cases. However, this may not be the case when diffusivity is very low, a condition that can be attained in many simple liquids like silicon oils [44], colloidal and polymer suspensions [5], or in geologically relevant fluids such as silicate fluids in the Earth mantle [45,46]. Finally, we note that this argument offers also a possible explanation for the absence of deformation for the triethylene glycol drop in Fig. 1, panel B. Indeed, TEG has a miscibility with glycerol similar to that of water, the three liquids having similar Hansen solubility parameters [47], but it is significantly more viscous than water ($\eta_{\mathrm{TEG}} = 49$ mPa s). Therefore, one may expect, on the timescale of our experiments, a stronger effect of the EIT as compared to the case of water drops, thus preventing the development of the dumbbell shape.

IV. CONCLUSIONS

We have experimentally characterized the time evolution of the shape of miscible drops in SDT experiments. We have shown that a dumbbell shape arises for sufficiently low values of EIT, which depends not only on the density and viscosity contrast between the drop and the background fluids, but also on the molecular structure of the fluids. We have focused on mixtures of water and glycerol, for which literature data were conflicting [23,24,35], and employed the dynamics of the drop shape as a tool to measure the EIT. By means of a simple model which takes into account the normal stress on the drop surface, the shear stress opposing the deformation, and a Laplace-like term containing an effective interfacial tension, we obtained an EIT of 250 ± 50 nN/m for water in contact with pure glycerol, decreasing rapidly below the resolution limit of the method as the amount of glycerol in the drops increases above 10%. This result is in excellent agreement with an estimate of the order of magnitude for the EIT for the same system obtained from a phase field model [5], while it is orders of magnitude lower than the experimental limit of all conventional techniques for measuring interfacial tensions. Therefore, besides shedding light on the controversy stemming from conflicting literature data on the EIT between water and glycerol, our work demonstrates a new method to measure extremely low interfacial tensions and in particular the EIT, paving the way for a thorough understanding of Korteweg stresses and capillary phenomena in miscible fluids.

ACKNOWLEDGMENTS

We gratefully acknowledge support from the Centre National d'Études Spatiales (CNES). We thank Lucio Isa for fruitful discussions.

[1] J. S. Rowlinson and B. Widom, *Molecular Theory of Capillarity* (Dover, Mineola, NY, 2002).

[2] D. J. Korteweg, Sur la forme qui prennent les équations du movement des fluides si l'on tient compte des forces capillaires causées par des variations de densité considérable mais continues et sur la théorie de la capillarité dans l'hypothèse d'une variations continue de la densité, Arch. Neerl. Sci. Exactes Nat. **6**, 1 (1901).

[3] J. W. Cahn and J. E. Hilliard, Free energy of a nonuniform system. I. Interfacial free energy, J. Chem. Phys. **28**, 11 (1958).

[4] D. Truzzolillo and L. Cipelletti, Off-equilibrium surface tension in miscible fluids, Soft Matter **13**, 13 (2017).

[5] D. Truzzolillo, S. Mora, C. Dupas, and L. Cipelletti, Nonequilibrium Interfacial Tension in Simple and Complex Fluids, Phys. Rev. X **6**, 041057 (2016).

[6] P. Cicuta, A. Vailati, and M. Giglio, Capillary-to-bulk crossover of nonequilibrium fluctuations in the free diffusion of a near-critical binary liquid mixture, Appl. Opt. **40**, 4140 (2001).
[7] A. Vorobev, T. Zagvozkin, and T. Lyubimova, Shapes of a rising miscible droplet, Phys. Fluids **32**, 012112 (2020).
[8] L. K. Antanovskii, Microscale theory of surface tension, Phys. Rev. E **54**, 6285 (1996).
[9] M. Bier, Nonequilibrium interfacial tension during relaxation, Phys. Rev. E **92**, 042128 (2015).
[10] A. Vorobev and A. Boghi, Phase-field modelling of a miscible system in spinning droplet tensiometer, J. Colloid Interface Sci. **482**, 193 (2016).
[11] C.-Y. Chen and E. Meiburg, Miscible displacements in capillary tubes. Part 2. Numerical simulations, J. Fluid Mech. **326**, 57 (1996).
[12] C.-Y. Chen and E. Meiburg, Miscible displacements in capillary tubes: Influence of Korteweg stresses and divergence effects, Phys. Fluids **14**, 2052 (2002).
[13] V. Shevtsova, Y. A. Gaponenko, V. Yasnou, A. Mialdun, and A. Nepomnyashchy, Two-scale wave patterns on a periodically excited miscible liquid-liquid interface, J. Fluid Mech. **795**, 409 (2016).
[14] S. E. May and J. V. Maher, Capillary-Wave Relaxation for A Meniscus between Miscible Liquids, Phys. Rev. Lett. **67**, 2013 (1991).
[15] J. A. Pojman, C. Whitmore, M. L. Turco Liveri, R. Lombardo, J. Marszalek, R. Parker, and B. Zoltowski, Evidence for the existence of an effective interfacial tension between miscible fluids: Isobutyric acid-water and 1-butanol-water in a spinning-drop tensiometer, Langmuir **22**, 2569 (2006).
[16] A. Carbonaro, L. Cipelletti, and D. Truzzolillo, Spinning drop dynamics in miscible and immiscible environments, Langmuir **35**, 11330 (2019).
[17] K. Gowda. V, C. Brouzet, T. Lefranc, L. D. Söderberg, and F. Lundell, Effective interfacial tension in flow-focusing of colloidal dispersions: 3-D numerical simulations and experiments, J. Fluid Mech. **876**, 1052 (2019).
[18] S. Bamberger, G. V. Seaman, K. Sharp, and D. E. Brooks, The effects of salts on the interfacial tension of aqueous dextran poly(ethylene glycol) phase systems, J. Colloid Interface Sci. **99**, 194 (1984).
[19] Y. Liu, R. Lipowsky, and R. Dimova, Concentration dependence of the interfacial tension for aqueous two-phase polymer solutions of dextran and polyethylene glycol, Langmuir **28**, 3831 (2012).
[20] B. Vonnegut, Rotating bubble method for the determination of surface and interfacial tensions, Rev. Sci. Instrum. **13**, 6 (1942).
[21] G. Viner, T. La Monica, R. Lombardo, and J. A. Pojman, Effect of pseudo-gravitational acceleration on the dissolution rate of miscible drops, Chaos **27**, 104603 (2017).
[22] B. Zoltowski, Y. Chekanov, J. Masere, J. A. Pojman, and V. Volpert, Evidence for the existence of an effective interfacial tension between miscible fluids. 2. Dodecyl acrylate-poly(dodecyl acrylate) in a spinning drop tensiometer, Langmuir **23**, 5522 (2007).
[23] P. Petitjeans, Une tension de surface pour le fluides miscibles, C.R. Acad Sci. Paris **322**, 673 (1996).
[24] M. Legendre, P. Petitjeans, and P. Kurowski, Instabilités à l'interface entre fluides miscibles par forçage oscillant horizontal, C.R. Mec. **331**, 617 (2003).
[25] C. D. Manning and L. E. Scriven, On interfacial tension measurement with a spinning drop in gyrostatic equilibrium, Rev. Sci. Instrum. **48**, 1699 (1977).
[26] *Physical Properties of Glycerine and its Solutions* (Glycerine Producers' Association, New York, 1963).
[27] G. D'Errico, O. Ortona, F. Capuano, and V. Vitagliano, Diffusion coefficients for the binary system glycerol + water at 25 °C. A velocity correlation study, J. Chem. Eng. Data **49**, 1665 (2004).
[28] P. Galambos and F. K. Forster, in *Micro Total Analysis Systems 98*, edited by D. J. Harrison and A. van den Berg (Springer, Netherlands, Dordrecht, 1998), pp. 189–192.
[29] J. R. Lister and H. A. Stone, Time-dependent viscous deformation of a drop in a rapidly rotating denser fluid, J. Fluid Mech. **317**, 275 (1996).
[30] M. R. Spiegel and L. J. Stephens, *Statistics* (McGraw-Hill, New York, 2008).
[31] W. H. Press, S. A. Teukolsky, W. T. Vetterling, and B. P. Flannery, *Numerical Recipes in Fortran: The Art of Scientific Computing* (Cambridge University Press, Cambridge, 1996).
[32] See Supplemental Material at http://link.aps.org/supplemental/10.1103/PhysRevFluids.5.074001 for (i) the statistical significance of the c_w dependence of the deformation velocity, (ii) simulations of the

recirculating flow on top of spinning drops and the dependence of the flow on ΔP_ω, and (iii) the limitations of the direct visualization of the radial Saffman-Taylor instability as a method to measure the effective interfacial tension in water-glycerol systems.

[33] P. Currie and J. Van Nieuwkoop, Buoyancy effects in the spinning-drop interfacial tensiometer, J. Colloid Interface Sci. **87**, 301 (1982).

[34] A. Quarteroni, *Numerical Models for Differential Problems*, Modeling, Simulation and Applications, Vol. 16 (Springer International, Cham, 2017).

[35] L. Paterson, Fingering with miscible fluids in a Hele Shaw cell, Phys. Fluids **28**, 26 (1985).

[36] I. Bischofberger, R. Ramachandran, and S. R. Nagel, Fingering versus stability in the limit of zero interfacial tension, Nat. Commun. **5**, 5265 (2014).

[37] E. Lajeunesse, J. Martin, N. Rakotomalala, and D. Salin, 3D Instability of Miscible Displacements in A Hele-Shaw Cell, Phys. Rev. Lett. **79**, 5254 (1997).

[38] J. Miranda and M. Widom, Radial fingering in a Hele-Shaw cell: A weakly nonlinear analysis, Physica D **120**, 315 (1998).

[39] D. Truzzolillo, S. Mora, C. Dupas, and L. Cipelletti, Off-Equilibrium Surface Tension in Colloidal Suspensions, Phys. Rev. Lett. **112**, 128303 (2014).

[40] L. Jinwoo and H. Tanaka, Local non-equilibrium thermodynamics, Sci. Rep. **5**, 7832 (2015).

[41] D. Truzzolillo and L. Cipelletti, Hydrodynamic instabilities in miscible fluids, J. Phys.: Condens. Matter **30**, 033001 (2018).

[42] A. Kheniene and A. Vorobev, Linear stability analysis of a horizontal phase boundary separating two miscible liquids, Phys. Rev. E **88**, 022404 (2013).

[43] A. F. M. Barton, *Handbook of Poylmer-Liquid Interaction Parameters and Solubility Parameters* (CRC, Boca Raton, FL 1990).

[44] J. Kuang, T. Maxworthy, and P. Petitjeans, Miscible displacements between silicone oils in capillary tubes, Eur. J. Mech. B **22**, 271 (2003).

[45] G. Morra and D. A. Yuen, Role of Korteweg stresses in geodynamics, Geophys. Res. Lett. **35**, L07304 (2008)

[46] J. E. Mungall, Interfacial Tension in Miscible Two-Fluid Systems with Linear Viscoelastic Rheology, Phys. Rev. Lett. **73**, 288 (1994).

[47] C. M. Hansen, *Hansen Solubility Parameters - A User's Handbook* (CRC, Boca Raton, FL, 2000).

Supplemental material to Ultra-low effective interfacial tension between miscible molecular fluids

Alessandro Carbonaro,[1,*] Luca Cipelletti,[1] and Domenico Truzzolillo[1]

[1]*Laboratoire Charles Coulomb (L2C),*

UMR 5221 CNRS-Université de Montpellier, Montpellier, France

We provide here details on *i)* the statistical significance of the water concentration dependence of the deformation velocity of drops in a miscible background, *ii)* the simulations of the recirculating flow on top of spinning drops, and *iii)* the limitations of the direct visualization of the radial Saffman-Taylor instability as a method to measure the effective interfacial tension (EIT) in water-glycerol systems.

STATISTICAL SIGNIFICANCE OF THE c_w DEPENDENCE OF THE DEFORMATION VELOCITY

Figure 4b of the main text shows the deformation velocity v of drops evolving towards a dumbbell shape, as a function of the centripetal forcing ΔP_ω and for different values of the water mass fraction c_w of the drop. As seen in the figure, data may be divided in two sets: data points for $c_w \leq 0.75$ seem to be compatible with a straight line through the origin, while data for $c_w \geq 0.9$ apparently are not, since a linear fit exhibits a negative intercept with the v axis. Since the intercept depends on c_w, hence possibly on the EIT, it is important to perform a statistical analysis of the data in Fig. 4b, in order to ascertain whether the difference between the two sets of data is statistically significant or is just due to experimental noise.

Due to measurement uncertainties, experimental data y_{ex} measured as a function of a control parameter x_{ex} and supposedly described by some physical law $y = f(x)$ will always be scattered around the model prediction. Assuming that data scattering results from a large number of mutually independent error sources, the underlying distribution of the residues $y_{ex} - f(x_{ex})$ may be assumed to be Gaussian [1, 2]. When the number N of experimental data points is small, typically $N \lesssim 30$, statistics will deviate from that of large population samples. In particular, for small samples the Gaussian distribution of the residues will be replaced by the Student's t-distribution.

For our data, we consider the affine model $v = A\Delta P_\omega + B$ (Eq. (5) of the main text) and focus on the statistics of $\xi = v - A\Delta P_\omega$, where A is obtained by simultaneously fitting the two sets of data (experiments with $c_w \leq 0.75$ and $c_w \geq 0.9$, respectively), imposing the same slope for both data sets. We denote respectively by B_i, s_i, μ_i and N_i the mean, variance, expected value and number of samples for ξ_i, where the index $i = 1, 2$ refers to the two data sets. All values of the relevant experimental parameters are recapitulated in Table SMT1.

Data set	c_w	N_i	B_i (m/s)	s_i (m/s)
$i = 1$	≤ 0.75	9	-5.4×10^{-8}	3.3×10^{-7}
$i = 2$	≥ 0.9	8	-1.6×10^{-6}	6.1×10^{-7}

TABLE SMT1. Parameters for the analysis of the statistical significance of the data of Fig. 4 of the main manuscript. See text for more details.

To test the statistical significance of the difference between B_1 and B_2, we quantify the probability that the underlying expected values are actually identical, $\mu_1 = \mu_2$, while B_1 and B_2 differ just by chance, having being obtained from a limited number of experimental data points. For small populations, the standardized difference between the two mean values, t, is distributed according to a Student's t-distribution with $N_1 + N_2 - 2$ degrees of freedom, with

$$t = \frac{B_1 - B_2}{\sigma\sqrt{1/N_1 + 1/N_2}}\,, \tag{1}$$

and where σ is obtained from the experimental sample variances s_1 and s_2 as $\sigma = \sqrt{\frac{N_1 s_1^2 + N_2 s_2^2}{N_1+N_2-2}}$. Using the values reported in Table SMT1, we find $t = 6.43$, larger than $t = 4.073$, the edge of the 0.1% confidence interval for a two-tailed t-distribution with $N_1 + N_2 - 2 = 15$ degrees of freedom. We conclude that $\mu_1 \neq \mu_2$ with probability larger than 99.9%, i.e. that the difference between B_1 and B_2 is indeed statistically significant.

RECIRCULATING SECONDARY FLOW AND DEPENDENCE ON ΔP_ω

In any spinning drop tensiometry experiment, the background fluid is not at rest, but rather flows towards the axis of the capillary inducing an extra normal stress on the drop surface [3]. This phenomenon, present even for stationary, ellipsoidal drops, has been invoked to rationalize the origin of dumbbell shapes when the interfacial tension between the drop and the background fluid is extremely weak [4, 5]. Indeed, in a spinning capillary the centripetal pressure P depends on the axial, x, and radial, r, coordinates as:

$$P(r, x) = \int_0^r \rho(r', x)\omega^2 r' \mathrm{d}r'\,, \tag{2}$$

where ω is the rotational speed and ρ the fluid-dependent mass density. Since the mass density of the drop is lower than that of the background fluid, for a given distance r from

the capillary axis P is lower in the x region occupied by the drop, as shown in Fig. SM1, which displays the axial profile of P for a cylindrical drop capped by two hemispheres. The horizontal pressure gradient due to the pressure drop in the region $x_A < x < x_D$ induces a recirculation flow in the capillary.

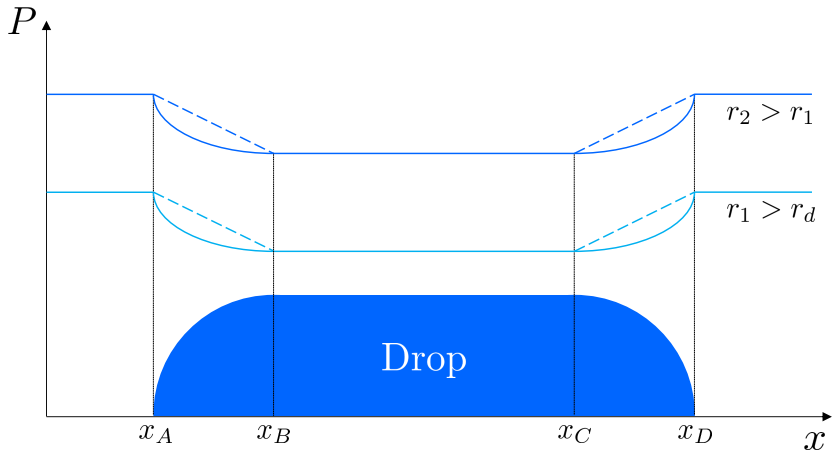

Figure SM1: Axial dependence of the pressure in the background fluid in a spinning drop experiment, for two distances r from the capillary axis, both larger than the drop radius. The drop shape is shown as the blue region. The solid lines show the pressure profile for a cylindrical drop capped by two hemispheres. The dashed lines show the simplified, piece-wise linear profile used in the calculations. The decrease of P in the x range occupied by the drop is responsible for the recirculation flow of the background fluid shown schematically in Fig. 5 of the main manuscript.

To gain insight on this flow, we solve numerically the Navier-Stokes equations for the background fluid in the region $x_A \leq x \leq x_D$ and $r_d \leq r \leq r_C$, with r_d and r_C the radius of the drop and of the capillary, respectively. We assume all fluids to be incompressible and write the momentum conservation equation by splitting the pressure into its steady and unsteady contributions: $p(x,r) = P(x,r) + p'(x,r)$, where the r.h.s. terms represent the inhomogeneous centripetal pressure and the pressure associated to fluid motion, respectively. One obtains

$$\frac{\partial \vec{v}}{\partial t} + (\vec{v} \cdot \nabla)\vec{v} = -\frac{1}{\rho}\nabla(P + p') + \nu\nabla^2\vec{v}\,, \tag{3}$$

where $\vec{v}$, ρ and ν are the fluid velocity, density and kinematic viscosity, respectively. Sepa-

rating the two contributions to the pressure field is equivalent to including in the momentum equation a source term arising from the (steady) pressure gradient, $-\frac{1}{\rho}\nabla P = \vec{F}$:

$$\frac{\partial \vec{v}}{\partial t} + (\vec{v}\cdot\nabla)\vec{v} = -\frac{1}{\rho}\nabla p' + \nu\nabla^2\vec{v} + \vec{F} \tag{4}$$

The cylindrical symmetry of the capillary allows the problem to be solved in two dimensions, yielding the following set of equations:

$$\frac{\partial u}{\partial t} + u\frac{\partial u}{\partial x} + v\frac{\partial u}{\partial r} = -\frac{1}{\rho}\frac{\partial p'}{\partial x} + \nu\left(\frac{\partial^2 u}{\partial x^2} + \frac{\partial^2 u}{\partial r^2}\right) + F_x \tag{5}$$

$$\frac{\partial v}{\partial t} + u\frac{\partial v}{\partial x} + v\frac{\partial v}{\partial r} = -\frac{1}{\rho}\frac{\partial p'}{\partial r} + \nu\left(\frac{\partial^2 v}{\partial x^2} + \frac{\partial^2 v}{\partial r^2}\right) + F_r \tag{6}$$

$$\frac{\partial^2 p'}{\partial x^2} + \frac{\partial^2 p'}{\partial r^2} = -\rho\left[\left(\frac{\partial u}{\partial x}\right)^2 + 2\frac{\partial u}{\partial r}\frac{\partial v}{\partial x} + \left(\frac{\partial v}{\partial r}\right)^2\right] \tag{7}$$

where u and v denote the x and r components of $\vec{v}$, respectively. Equation 7 is the Poisson equation for the pressure obtained by inserting the incompressibility condition for the background fluid ($\nabla\cdot\vec{v} = 0$) in the momentum equation.

We numerically solve Eqs.(5-7) for the background fluid ($r > r_d$), in the x range occupied by the drop, with boundary conditions $(u, v) = (0, 0)$ and $\frac{\partial p}{\partial \vec{n}} = 0$ at the drop-background fluid interface and at the capillary wall, where $\vec{n}$ is the unit vector normal to each boundary. The solution for u, v and p is obtained by performing a central discretization on the variables [6] and by iterating until stability is reached. Note that we are interested in understanding the general behavior of the recirculating flow rather than its detailed behavior. Accordingly, for the sake of simplicity we approximate the pressure profile $P(x)$ by a piecewise linear function with a trapezoidal shape and a pressure drop $\Delta P_\omega = \frac{\omega^2}{2}(\rho_f - \rho_d)r_d^2$ in correspondence with the drop body (see dashed lines in Fig. SM1).

In order to investigate the external forcing on the drop surface due to the recirculating flow, we evaluate the radial component of the velocity in the x range occupied by the drop body, $x_B < x < x_C$. Since we are interested in the radial deformation of the drop towards a dumbbell shape, we look for a difference between v at the center of the drop and close to the heads. Figure SM2 a) shows the axial dependence of $\Delta v(x) = v(x_B) - v(x)$, for various ΔP_ω. The data are obtained for $r = 19$, but they are representative of all r within the gap between the drop and the capillary wall. Clearly, the magnitude of the radial velocity is larger at the center of the drop than near the heads, resulting in the drop surface being

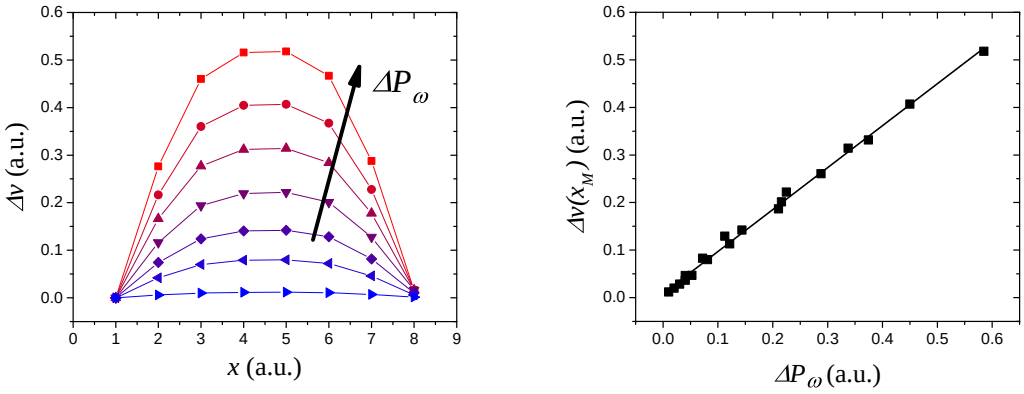

(a) (b)

Figure SM2: (a) Radial velocity difference $\Delta v(x) = v(x_B) - v(x)$ of the background fluid for several magnitudes of the centripetal forcing ΔP_ω, obtained from a numerical solution of Eqs.(5-7), with $x_B = 1$, $x_C = 8$, $r_d = 15$ and $r = 19$. ΔP_ω varies from 0.01 to 0.58 by steps of 0.095, from the bottom curve to the top one. (b) Symbols: maximum value of Δv, attained at $x_M = 4.5$, as a function of ΔP_ω. The line is a linear fit through the origin.

pushed towards the capillary axis stronger at its center than at the heads, consistent with the development of a dumbbell shape. Figure SM2 a) shows also that the velocity imbalance increases with increasing ΔP_ω, i.e. with increasing angular velocity or density mismatch. To quantify the dependence on the centripetal forcing, we plot in Fig. SM2 b) the maximum value of Δv, attained in correspondence to the center x_M of the drop body, as a function of ΔP_ω. The magnitude of the recirculating flow, $\Delta v(x_M)$, is found to depend linearly on ΔP_ω. This justifies writing the normal stress induced by the recirculating flow at the onset of the instability as $n_E = \alpha \Delta P_\omega$, with α a positive constant, as it was done in Sec. III A of the main text. Moreover, this explains why the experimental deformation velocity depends linearly on ΔP_ω, as seen in Fig. 4b of the main text.

CAN THE DIRECT VISUALIZATION OF THE RADIAL SAFFMAN-TAYLOR INSTABILITY BE USED AS A METHOD TO MEASURE Γ_e IN WATER-GLYCEROL SYSTEMS?

The Saffman-Taylor (S-T) instability occurs when a less viscous fluid displaces a more viscous one confined in a porus medium. The boundary between the fluids is uneven and the less viscous fluid develops fingers protruding into the more viscous one. Most experimental research on viscous fingering has been performed using Hele-Shaw cells, which consist of two closely spaced, parallel plates of glass. In the widely used radial configuration, the more viscous fluid is confined between the two plates and the less viscous fluid is injected through a small hole drilled in the center of one of the plates. We have recently shown that the analysis of the characteristic wavelength λ_{ST} at the onset of the radial S-T instability is a valuable tool to investigate interfacial stresses in miscible colloidal and polymeric fluids [7, 8]. One may thus wonder if the same strategy could be employed to measure Γ_e for water-glycerol systems.

Various experiments, however, have suggested that radial S-T instabilities occurring when water displaces glycerol [9] —or more generally when two different water-glycerol mixtures are used to generate S-T patterns [10]— are not affected by capillary forces. In 1985, Paterson [9] showed that in the absence of interfacial tension a cut-off wavelength characterizes the onset of the S-T instability. Namely, his theoretical analysis shows that for $\Gamma_e = 0$ the growth of the instability is dominated by viscous dissipation, giving rise to a characteristic wavelength dictated only by the cell gap b: $\lambda_{ST} \simeq 4b$. By contrast, for $\Gamma_e > 0$, the wavelength characterizing the onset of the instability depends not only on b, but also on the injection rate of the less viscous fluid, the viscosity contrast between the fluids and the interfacial tension [7]. In particular, all other parameters being fixed, λ_{ST} grows with Γ_e, such that $\lambda_{ST} \simeq 4b$ is the minimum wavelength of a S-T instability observable in a radial viscous fingering experiment. The experimental data for water/glycerol systems of Refs. [9, 10] are consistent with $\Gamma_e \simeq 0$, since it was found that $\lambda_{ST} \simeq 4b$.

In order to evaluate the feasibility of measuring Γ_e in water-glycerol systems via the visualization of S-T patterns, we perform numerical simulations based on the linear analysis introduced by Miranda and Widom [11]. Our goal is to quantify the minimum value of Γ_e that could be measured by this method in a Hele-Shaw experiment with optimized yet real-

istic parameters. In the simulations, the fluid-fluid interface is supposed to expand radially. A perturbation around this circular interface develops with time, due to the instability. It is convenient to decompose the perturbation in Fourier modes with complex amplitude $\zeta_n(t)$, $n = 1, 2, ...$ Assuming that the noise giving rise to the instability is a complex number ζ_n^0, with a random phase and a n-independent modulus, the time evolution of the amplitude of the n-th mode is given by [7, 11]:

$$\zeta_n(t) = \zeta_n^0 \left\{ \left(K(t) \frac{(nA-1)}{n^2(n-1)}^{nA-1} \right) \exp\left[(nA-1) \left(\frac{1}{K(t)} \frac{n(n^2-1)}{nA-1} - 1 \right) \right] \right\} . \quad (8)$$

In Eq. (8), $A = (\eta_2 - \eta_1)/(\eta_2 + \eta_1) > 0$ is the viscosity contrast between the two fluids and $K(t) = [r(t)Q]/(2\pi\beta)$, where $r(t)$ is the distance of the unperturbed fluid-fluid interface from the center of the cell, Q is the area covered by the injected fluid per unit time, and $\beta = b^2\Gamma/[12(\eta_1 + \eta_2)]$, with b the cell gap and Γ the interfacial tension between the two fluids. Note that Eq. (8) only holds for $nA > 1$, a condition fulfilled for water displacing glycerol for all $n > 1$. We emphasize that Eq. (8) is derived in the framework of a quasi 2D theory that neglects the curvature of the interface along the direction perpendicular to the glass plates. As a result, this theory poses no lower bound on the wavelength of the instability: values of $\lambda_{ST} < 4b$ issued from the simulations should therefore be regarded as nonphysical and discarded.

Using Eq. (8) and summing the contributions of 500 modes, we simulate the S-T instability in a Hele-Shaw cell with $b = 250$ μm, as in previous works on miscible fluids [8, 10]. The top row of Fig. SM3 shows three representative sets of interface positions at various times, obtained from simulations with different values of Γ_e, as indicated by the labels. We measure the wavelength of the instability at its onset by counting the number of nodes (inflection points) along the first contour line for which inflection points clearly emerge from the background noise. The wavelength thus obtained is plotted in the bottom panel of Fig. SM3, for three injection rates $\dot{V}$ within the typical range of experimentally accessible values [7, 8, 10]. Keeping in mind that data points with $\langle \lambda_{ST} \rangle < 4b$ are nonphysical, one concludes that for the parameters used here Γ_e values smaller than about 0.1 mN/m are unaccessible. This sets an upper bound for the interfacial tension between water and glycerol measured in previous Hele-Shaw experiments. Note that, in principle, thinner Hele-Shaw cells would allow smaller values of λ_{ST} and hence of Γ_e to be measured. However, for $b < 250$ μm it is hard to pre-fill homogeneously the cell with the more viscous fluid (glycerol in our case), because of the

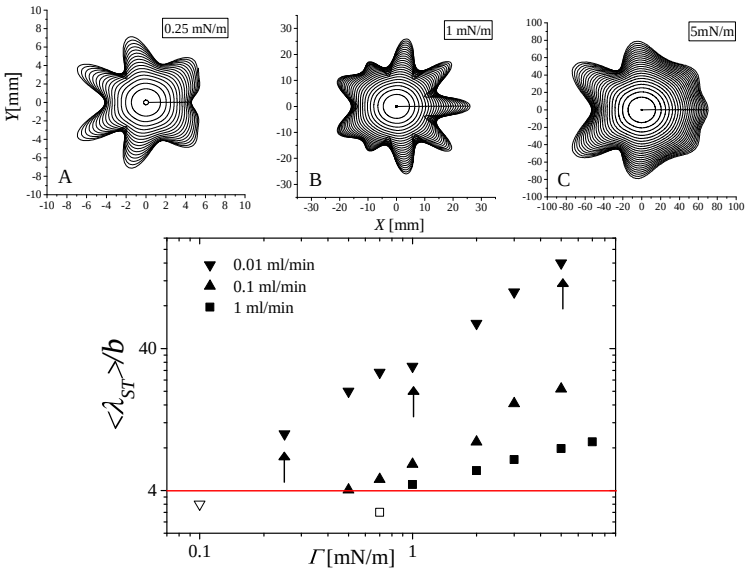

Figure SM3. Top row: representative patterns obtained at $\dot{V} = 0.01$ ml/min and for three values of the interfacial tension, as indicated by the labels. The curves display the interface between the two fluids at times that increase respectively from 10 s by steps of 10 s (A), from 10^2 s by steps of 10^2 s (B) and from 10^3 s by steps of 10^3 s (C). Bottom panel: Average wavelength of the radial S-T instability $\langle \lambda_{ST} \rangle$ at its onset as a function of the interfacial tension Γ for three different injection rates. $\langle \lambda_{ST} \rangle$ is obtained by averaging results from 10 simulation runs, with $b = 250$ μm and a random noise amplitude $|\zeta_n^0| = 10^{-9}$ m. The arrows indicate the data points corresponding to the three panels of the top row. Open symbols refer to nonphysical values $\langle \lambda_{ST} \rangle < 4b$ and should be discarded, as discussed in the text.

heterogeneous local wetting of the fluid on the cell walls, which are unavoidably irregular on the micron scale. This typically gives rise to an anisotropic distribution of the fluid in the cell, leading to erratic experimental results.

Another strategy to access very small Γ_e values by investigating the S-T instability might consist in using extremely low injection rates. Indeed, the bottom graph of Fig. SM3 shows that reducing the injection rate shifts the lower bound on the measurable EIT to lower values. To test whether this approach would be practically feasible, we run simulations imposing $\Gamma_e = 250 \times 10^{-6}$ mN/m, the value inferred from our spinning drop experiments. We tune the injection rate so as to keep the wavelength of the perturbation at the onset of the instability just above the limiting value $\lambda_{ST} = 4b$. The resulting pattern is shown in Fig. SM4. We

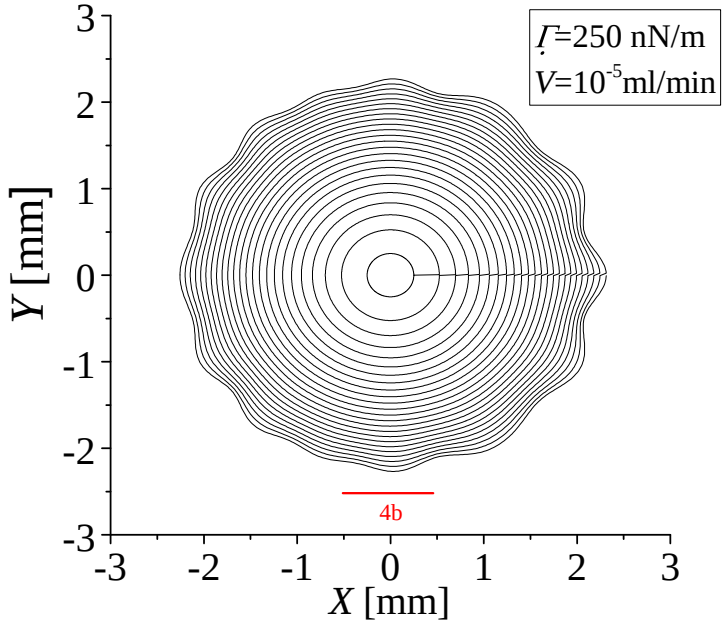

Figure SM4. Typical S-T pattern obtained by imposing $\Gamma_e = 250 \times 10^{-6}$ mN/m, as in our spinning drop experiments. The injection rate (10^{-5} ml/min) has been chosen to match the limiting condition $\langle \lambda_{ST} \rangle \approx 4b$. The time needed to the interface to reach the radius at which the instability becomes measurable is $t_{onset} \simeq 314$ s.

find that an extremely small injection rate would be required: $\dot{V} = 10^{-5}$ ml/min. Even more importantly, the onset of the instability would occur 314 s after starting the injection, a time span one order of magnitude larger than that in our spinning drop experiments. Over such a long time, diffusion would significantly smear out the interface, reducing the EIT well below the resolution of any method currently available. Therefore, the measurement of Γ_e through the detection of S-T patterns in water-glycerol systems appears to be unfeasible, because diffusion smears the interface at very low injection rates, while viscous dissipation alone dictates the interface shape at higher rates.

* Electronic address: `alessandro.carbonaro@umontpellier.fr`

[1] M. R. Spiegel and L. J. Stephens, *Statistics* (McGraw-Hill, 2008), schaum ed.

[2] W. H. Press, S. A. Teukolsky, W. T. Vetterling, and B. P. Flannery, *Numerical recipes in fortran: the art of scientific computing* (Cambridge University Press, 1996), ISBN 978-0-521-

43064-7 978-0-521-57439-6.

[3] P. Currie and J. Van Nieuwkoop, Journal of Colloid and Interface Science **87**, 301 (1982), ISSN 00219797, URL https://linkinghub.elsevier.com/retrieve/pii/0021979782903289.

[4] C. D. Manning and L. E. Scriven, Review of Scientific Instruments **48**, 1699 (1977), ISSN 0034-6748, 1089-7623, URL http://aip.scitation.org/doi/10.1063/1.1134934.

[5] B. Zoltowski, Y. Chekanov, J. Masere, J. A. Pojman, and V. Volpert, Langmuir **23**, 5522 (2007), ISSN 0743-7463, 1520-5827, URL https://pubs.acs.org/doi/10.1021/la063382g.

[6] A. Quarteroni, *Numerical Models for Differential Problems*, vol. 16 of *MS&A* (Springer International Publishing, Cham, 2017), ISBN 978-3-319-49315-2 978-3-319-49316-9, URL http://link.springer.com/10.1007/978-3-319-49316-9.

[7] D. Truzzolillo, S. Mora, C. Dupas, and L. Cipelletti, Physical Review Letters **112** (2014), ISSN 0031-9007, 1079-7114, URL https://link.aps.org/doi/10.1103/PhysRevLett.112.128303.

[8] D. Truzzolillo, S. Mora, C. Dupas, and L. Cipelletti, Physical Review X **6**, 041057 (2016).

[9] L. Paterson, Physics of Fluids **28**, 26 (1985), ISSN 0031-9171, URL https://aip.scitation.org/doi/10.1063/1.865195.

[10] I. Bischofberger, R. Ramachandran, and S. R. Nagel, Nature Communications **5** (2014), ISSN 2041-1723, URL http://www.nature.com/articles/ncomms6265.

[11] J. Miranda and M. Widom, Physica D: Nonlinear Phenomena **120**, 315 (1998), ISSN 01672789, URL https://linkinghub.elsevier.com/retrieve/pii/S0167278998000979.

Chapter 4

Spinning elastic beads: a route for simultaneous measurements of the shear modulus and the interfacial energy of soft materials

Even though the main interest of this thesis is the investigation of capillary phenomena at miscible interfaces, the techniques that we employ are also applicable to other systems. In particular, spinning drop tensiometry can be used to investigate the interplay between capillarity and elasticity when a soft solid bead is inserted in the spinning capillary, allowing for an independent measure of the bead elastic modulus and of the interfacial tension between the bead and the background fluid. Since more conventional techniques rely on the measurement of the elasto-capillary length (the ratio of the interfacial energy per unit area to the elastic modulus) and cannot decouple the capillary and elastic contribution, this use of SDT appears as a promising way to access both the shear modulus and the surface energy of soft solids. Here we present an investigation of this method, recently published in [31].

Soft Matter

ROYAL SOCIETY OF CHEMISTRY

PAPER

View Article Online
View Journal

Check for updates

Cite this: DOI: 10.1039/d0sm01024c

Spinning elastic beads: a route for simultaneous measurements of the shear modulus and the interfacial energy of soft materials

Alessandro Carbonaro, †[a] Kennedy-Nexon Chagua-Encarnacion,†[a] Carole-Ann Charles,†[a] Ty Phou,[a] Christian Ligoure, *[a] Serge Mora *[b] and Domenico Truzzolillo *[a]

Received 2nd June 2020,
Accepted 5th August 2020

DOI: 10.1039/d0sm01024c

rsc.li/soft-matter-journal

Large deformations of soft elastic beads spinning at high angular velocity in a denser background fluid are investigated theoretically, numerically, and experimentally using millimeter-size polyacrylamide hydrogel particles introduced in a spinning drop tensiometer. We determine the equilibrium shapes of the beads from the competition between the centrifugal force and the restoring elastic and surface forces. Considering the beads as neo-Hookean up to large deformations, we show that their elastic modulus and interfacial energy constant can be simultaneously deduced from their equilibrium shape. Also, our results provide further support to the scenario in which interfacial energy and interfacial tension coincide for amorphous polymer gels.

1 Introduction

When subjected to external loads, elastic bodies change their shape due to the interplay between the applied load and the restoring forces of the material the body is made of.[1,2] Below the elastic limit, these are the bulk elastic forces following the material-specific stress–strain relation, and the surface forces dictated by the interfacial free energy that characterizes the interaction with the surrounding medium. Since the subtle balance between these forces stays relevant even beyond the elastic limit and determines, together with the onset of plastic events, the occurrence of material failure and permanent deformation,[3] bulk and surface stresses turn out to drive the behavior of soft materials under many circumstances.[1–3] For this reason understanding the importance of these two contribution to material response is of paramount importance.

The impact of interfacial stresses on the equilibrium shape of elastic materials can be readily quantified by the elasto-capillary length ℓ, defined as the ratio of the interfacial energy per unit area Γ to the shear modulus G_0 of the body under consideration. When ℓ is comparable with or larger than other characteristic lengths of the system[4–6] interfacial stresses must be taken into account to compute stationary material shapes and to predict possibly the onset of instabilities.[7–9] This is the case for soft elastic samples with small geometric features. For example, for a hydrogel with shear modulus $G_0 \sim 30$ Pa and interfacial tension $\Gamma \sim 30$ mN m^{-1}, the elasto-capillary length is $\ell = 1$ mm. Therefore, the equilibrium shapes of millimetric and submillimetric elastic particles must be necessarily affected by the interfacial contribution to their total energy.

Despite of this general and well-grounded consideration, many important questions concerning the interplay between bulk and interfacial stresses[10,11] and the very nature of the latter in amorphous solids[12,13] remain unanswered. For a generic material immersed in a background medium interfacial energy is the energy required to create a unit area of new surface by a division process, whereas interfacial tension is the surface stress associated with its deformation. For Newtonian liquids, interfacial tension and interfacial energy are two strictly equal quantities since, when a liquid interface is deformed, the distances between the molecules at the interface are not affected by the imposed deformation as molecules can move freely from the bulk to the liquid boundaries. It is generally not so for a solid, for which interfacial energy may depend on the surface area, as first pointed out by Shuttleworth[14] in his pioneering work. Since a solid surface consists of a constant number of atoms, the work done to alter the separation distance between atoms at their surface is expected to depend on this distance itself.[14–16] As a result, the work required to deform a material is not necessarily the same as the thermodynamic work required to create a new surface. For crystals the problem has been solved[16,17] since their

[a] Laboratoire Charles Coulomb, Université de Montpellier and CNRS, F-34095 Montpellier, France. E-mail: christian.ligoure@umontpellier.fr, domenico.truzzolillo@umontpellier.fr
[b] Laboratoire de Mécanique et Génie Civil, Université de Montpellier and CNRS, F-34090 Montpellier, France. E-mail: serge.mora@umontpellier.fr
† These three authors contributed equally.

surface free energy is a function of the surface area itself and hence it is expected to be different from the surface tension. However, for amorphous materials, like cross-linked elastomers, the issue remains unresolved because the molecules have local mobility allowing them, at least in principle, to show liquid-like behavior: the surface reforms in response to external stimuli.[18,19] While this liquid-like scenario has been recently confirmed for Polydimethylsiloxane (PDMS) elastomers,[12] other experimental works pointed out that for specific soft gels[13,20,21] the interfacial energy does depend on the surface area, or equivalently on the imposed compressive strain parallel to the surface, and, as a consequence, interfacial free energy and interfacial stress are expected to differ.[14,20,21]

Moreover, for most solid materials the accurate measurement of the interfacial energy is experimentally challenging, since the intimate coupling between the contributions of interfacial and bulk energies hampers the detection of effects solely due to interfacial stresses. For instance instability thresholds[5,22] and the shapes taken by softened wedges[23–25] or ripple deformations[26] involve the coupling between surface stress and bulk elasticity through the elasto-capillary length, making impossible to determine separately the two parameters (G_0 and Γ). Even if one of the two parameters, *e.g.* the shear modulus, were determined elsewhere, a measurement relying on a single experiment is of limited accuracy. To solve this problem, indentation tests, standard rheometry or stretching tests, based on a gradual variation of an external load could in principle be used. However, these methods involve the presence of solid–solid contact forces[27,28] that typically affect the measurement and give rise to issues like slip and edge fracture. Furthermore, in the case of ultrasoft gels the measurement of the elastic modulus through these techniques is even more troublesome since one would be confronted with issues related to insufficient instrumental accuracy.

For these reasons, unveiling effects of surface energy in soft solids remains arduous and it has not been possible to converge to any conclusive result. This motivates investigations of phenomena that originate from a non-negligible contribution of interfacial free energy in the absence of solid–solid contacts over a wide range of strains, while, at the same time, engineering strategies to fully decouple interfacial and bulk stresses would be highly desirable.

In this paper, we tackle this challenging task and report on a theoretical and numerical study of the deformation of soft neo-Hookean beads when they are immersed and spun in a denser background fluid. Strikingly we found that, if the interfacial energy of the beads does not depend on their deformation, the elastic and the interfacial contributions determining the bead shape can be decoupled when the strong deformation limit is reached, namely when the ratio between the two principal axis of the deformed particles is $d_{\max}/d_{\min} \gtrsim 2$. To check further the reliability of our results we have investigated the deformation of soft polyacrylamide beads immersed in a denser immiscible fluid and spun in the capillary of a commercial spinning drop tensiometer (SDT).

Though an SDT is usually employed to measure low liquid–liquid interfacial free energies,[29–31] recently it has been used also for purposes ranging from the study of the relaxation dynamics of liquid drops[32] and the presence of an effective interfacial tension in miscible fluids,[32–35] to the characterization of the mechanical properties of thin elastic capsules[36] and viscoelastic properties of polymer melts.[37,38]

Unlike the aforementioned works, here we use an SDT to investigate the equilibrium shapes of full elastic beads with a radius of the order of one millimeter and shear modulus of the order of 10 Pa,[10] for which we expect important elasto-capillary effects. The analysis proposed in this work has been developed specifically for homogeneous beads and is far different from previous attempts to adapt spinning drop tensiometry measurements to elastic and viscoelastic bodies.[36–38]

When the SDT capillary is spun around its axis at a prescribed angular velocity, and once a steady state is reached, the beads spin solidly with the background fluid and the capillary itself. Since the surrounding fluid is denser than the bead, the centrifugal forces center and stretch the bead on the axis of rotation (Fig. 1). In this geometry, the sample bead is entirely surrounded by a liquid without any contact with other solid bodies. This is an important benefit of this geometry as the only interfacial free energy to be considered is the solid–liquid one. In addition, the external load (*i.e.* the centrifugal forces) can be finely tuned up to values generating large deformations ($\gtrsim$500%) of the bead.

The remainder of this paper is organized as follows. Assuming an interfacial energy independent from the deformation, the base equations governing the equilibrium of a spinning elastic bead surrounded by a liquid spinning at the same angular velocity are derived in Section IIA. These equations are first solved by assuming a homogeneous (biaxial) deformation of the bead (Section IIB). It is shown that, within this approximation, the effects on the deformation due to the contributions of the interfacial free energy and bulk elasticity can be decoupled at high centrifugal forcing. A full resolution of the base equations is made in Section IIC using the Finite Element method, showing the limitation of the biaxial approximation for a quantitative analysis. Interestingly, the behaviour emerging from the approximation still holds, providing a way to access to both the elastic

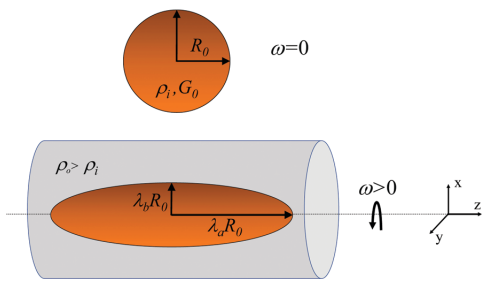

Fig. 1 Sketch of a spherical elastic bead immersed in a liquid of higher mass density and deformed by centrifugal forcing. (a) Initial configuration of the bead at rest (ω = 0). (b) The elastic bead is spun solidly ($\omega > 0$) with a denser fluid, both being contained in a cylindrical capillary. Centrifugal forces give rise to the reversible deformation of the bead and stabilize its position on the capillary axis.

View Article Online
Soft Matter Paper

modulus and the interfacial free energy constant of the beads. In Section III we report on experiments carried out with a commercial spinning drop tensiometer and soft polyacrylamide beads. A discussion of the main results and a comparison with the expected values for G_0 and Γ follows. Our experimental results point out that, for acrylamide gels, the interfacial energy is strain-independent and hence that the Shuttleworth effect is absent.[14] Such a conclusion has been further tested by comparing the interfacial energy of the beads and the interfacial tension measured between the background fluid and a non-crosslinked liquid polyacrylamide solution. The agreement between these two values further corroborates a scenario in which bulk elasticity does not contribute significantly to interfacial stresses. Finally, in Section IV we make some concluding remarks and summarize the key results of this work.

II Theory

A. Equilibrium equations at finite strains

The non-linear equations governing the equilibrium (steady) configuration of a rotating elastic sphere are derived considering a positive constant interfacial energy and an isotropic and incompressible neo-Hookean constitutive law. The latter is known to describe well the mechanical properties of soft polyacrylamide gels for strains up to several hundred percent.[39–41]

Let us consider an elastic bead of radius R_0, shear modulus G_0 and density ρ_i immersed in an infinite Newtonian background fluid of density $\rho_o > \rho_i$. As the sphere is spun at angular velocity ω around one diameter (aligned along axis z), the bead deforms, stretching along the rotation axis to minimize its rotational energy. In the co-rotating frame the elastic force, the surface force and the centrifugal force are conservative. The equilibrium can therefore be derived from the condition that the total potential energy is minimum. The position $\mathbf{R}$ of a material point in the deformed configuration is given as a map $\mathbf{R}(\mathbf{r})$ in terms of the position r in the undeformed configuration. For an isotropic and incompressible neo-Hookean solid, the strain energy density is:

$$W_{\mathrm{el}} = \frac{G_0}{2}\mathrm{tr}\left(\mathbf{F}^T \cdot \mathbf{F} - \mathbf{1}\right), \tag{1}$$

where $\mathbf{F} = \partial\mathbf{R}/\partial\mathbf{r}$ is the deformation gradient and $\mathbf{1}$ the unit matrix. The equilibrium is governed by the minimization of the free energy

$$\mathcal{E} = \Gamma A + \int_{\Omega_0} W_{\mathrm{el}} \mathrm{d}V_0 + \int_{\Omega_0} \frac{1}{2}\Delta\rho\omega^2 R^2 \mathrm{d}V_0, \tag{2}$$

where R is the radial distance from the z-axis in the deformed configuration ($R = \mathbf{R}\cdot\mathbf{R} - \mathbf{R}\cdot\mathbf{e}_z$), $\mathrm{d}V_0$ is a volume element in the reference configuration, Ω_0 is the volume occupied by the bead, A is the area of the deformed boundary and $\Delta\rho = \rho_o - \rho_i$ is the mass density contrast. It's worth stressing that we assume Γ independent of the deformation and the first term on the right hand side of eqn (2), $\mathcal{E}_\Gamma = \Gamma A$, represents the total interfacial energy of the system. This assumption, consistent with previous findings on elastic capsules[42,43] and equivalent to the absence of a Shuttleworth effect,[14] will be discussed in the light of the results reported in Section III. The second and the third terms are respectively the elastic and the centrifugal energies,[44] called later $\mathcal{E}_\varepsilon$ and $\mathcal{E}_\omega$. The equilibrium is governed by the minimization of the free energy, taking into account incompressibility of the elastic material which amounts to impose that the Jacobian of the transformation is equal to one:

$$\det\mathbf{F} = 1. \tag{3}$$

B. Biaxial approximation

1. General equations within the biaxial approximation. To a first approximation, the problem is simplified by assuming a homogeneous and biaxial deformation of the bead. In the Cartesian coordinate system (x,y,z), the applied centrifugal forcing gives rise to a prolate ellipsoid with axes $X = \lambda_b x$, $Y = \lambda_b y$ and $Z = \lambda_a z$. The stretch ratios λ_a and λ_b are two strictly positive constants with $\lambda_b < 1$ and $\lambda_a > 1$. This is sketched in Fig. 1. Eqn (3) further imposes $\lambda_a\lambda_b^2 = 1$. For a neo-Hookean material, the strain energy density is $W_{\mathrm{el}} = \frac{1}{2}G_0\left(\lambda_a^2 + 2\lambda_b^2 - 3\right)$ and the elastic energy defined in eqn (2) reads:

$$\mathcal{E}_\varepsilon = \frac{4}{3}\pi R_0^3 \frac{1}{2} G_0\left(\lambda_a^2 + 2\lambda_b^2 - 3\right). \tag{4}$$

The total interfacial energy defined in eqn (2), is:

$$\mathcal{E}_\Gamma = \Gamma A = \Gamma\left[2\pi\lambda_b^2 R_0^2 + \frac{2\pi\lambda_a\lambda_b R_0^2}{e}\arcsin(e)\right], \tag{5}$$

where $e = \frac{\sqrt{\lambda_a^2 - \lambda_b^2}}{\lambda_a}$ is the eccentricity of the ellipsoid of revolution. Finally the centrifugal energy, also defined in eqn (2) is given by:

$$\mathcal{E}_\omega = \frac{1}{2}\int \Delta\rho\left(x^2 + y^2\right)\omega^2 \mathrm{d}V_0 = \frac{4\pi}{15}\Delta\rho\omega^2\lambda_b^2 R_0^5. \tag{6}$$

Using volume conservation, eqn (4)–(6) allow us writing the total reduced energy density, defined as $\varepsilon = \mathcal{E}/(G_0 V_0)$ with V_0 the volume of the bead, as:

$$\begin{aligned}\varepsilon &= \frac{\alpha}{5}\lambda_a^{-1} + \frac{1}{2}\left(\lambda_a^2 + 2\lambda_a^{-1} - 3\right) \\ &\quad + \frac{3\beta}{2}\left(\lambda_a^{-1} + \frac{\lambda_a^2}{\sqrt{\lambda_a^3 - 1}}\arcsin\sqrt{\frac{\lambda_a^3 - 1}{\lambda_a^3}}\right),\end{aligned} \tag{7}$$

with

$$\alpha = \frac{\Delta\rho R_0^2\omega^2}{G_0} \tag{8}$$

and

$$\beta = \frac{\Gamma}{G_0 R_0} \tag{9}$$

being two characteristic dimensionless numbers. In particular, α is the Cauchy number and results from the balance between

inertia and elastic energy, while β is the ratio of the elasto-capillary length to the bead radius.

For a given set (α, β), the equilibrium shape is given by the minimization of ε with respect to λ_a, *i.e.* by the solution of the nonlinear algebraic equation $\frac{d\varepsilon}{d\lambda_a} = 0$, which can be obtained numerically. The deformation parameter defined as the ratio of the length (d_{max}) to the width (d_{min}) of the deformed shape, or equivalently ${\lambda_a}^{3/2}$, obtained numerically by minimizing eqn (7), is plotted in Fig. 2. Hereafter we derive the analytical expression for the deformation parameter ${\lambda_a}^{3/2}$ in the two limiting cases of small and large deformations and we show that when the latter are attained a simultaneous measurement of the elastic modulus and the interfacial free energy is feasible.

2. Small deformation limit. Let us first elucidate the behavior of the stretch ratio λ_a in the weak deformation limit, corresponding to Cauchy numbers $\alpha \ll 1$. In this case we can safely write $\lambda_a = 1 + \xi$, with $0 < \xi \ll 1$ and approximate the reduced energy density as follows:

$$\varepsilon \simeq \frac{1}{5}\alpha + 3\beta - \frac{1}{5}\xi\alpha + \xi^2\left(\frac{1}{5}\alpha + \frac{3}{2} + \frac{6}{5}\beta\right). \tag{10}$$

Minimizing with respect to ξ brings to the following equilibrium deformation with respect to the bead at rest:

$${\lambda_a}^{3/2} - 1 \simeq \left[\frac{\alpha}{10 + 8\beta}\right]. \tag{11}$$

Eqn (11) cannot be used to determine separately G_0 and Γ from a single measurement of ${\lambda_a}^{3/2}$ as a function of ω, since the deformation cannot be expressed as the sum of two (or more) terms each containing only α or β separately.

3. Large deformation limit. For $\alpha \gg 1$ and $\lambda_a \gg 1$, eqn (7) can be approximated by the algebraic sum of three terms:

$$\varepsilon \simeq \frac{1}{2}{\lambda_a}^2 + \frac{3\pi}{4}\beta{\lambda_a}^{1/2} + \frac{\alpha}{5}{\lambda_a}^{-1}. \tag{12}$$

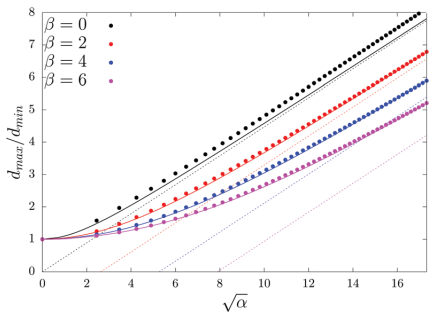

Fig. 2 Length-to-width ratio d_{max}/d_{min} of a deformed bead as a function of $\sqrt{\alpha}$ for different values of β (color coded). Solid lines are predictions from the biaxial approximation (minimization of eqn (7)). Asymptotes in the large α limit (eqn (14)) are plotted with dashed lines. Filled circles are the results of FE calculations discussed in Section II.C.

The minimization with respect to λ_a brings to:

$$d_{max}/d_{min} = {\lambda_a}^{3/2} = \frac{1}{2}\left[-\frac{3}{8}\pi\beta + \sqrt{\frac{9}{64}\pi^2\beta^2 + \frac{4}{5}\alpha}\right]. \tag{13}$$

Further expanding eqn (13) for $\alpha \gg 1$, we obtain:

$$d_{max}/d_{min} = \sqrt{\frac{\alpha}{5}} - \frac{3}{16}\pi\beta. \tag{14}$$

These asymptotes are plotted together with the complete expressions of d_{max}/d_{min} in Fig. 2 for different values of β. Note that due to the limited range of α, chosen accordingly with experiments introduced in Section III, the differences between the complete expression and the asymptotes remain significant and increases for increasing values of β. Quite interestingly eqn (14) decouples α and β, *i.e.* the effects of elasticity and interfacial energy on the bead deformation. In other words, for large centrifugal forcing, the deformation parameter ${\lambda_a}^{3/2}$ of a bead is proportional to the rotation speed with a proportionality constant equal to $R_0\sqrt{\frac{\Delta\rho}{G_0}}$. R_0 and $\Delta\rho$ being easily known a priori, G_0 can then be determined by considering the slope of ${\lambda_a}^{3/2}$ *versus* ω; next, the evaluation of a (virtual) intercept equal to $-\frac{3\pi\Gamma}{16G_0R_0}$ brings to the measurement of Γ.

G_0 and Γ can then be recovered by considering the large deformation limit with the biaxial approximation. In the following, we show that the approximation is not accurate enough to get precise values of these two quantities. Notwithstanding this, the main result stays valid: it is possible to determine both G_0 and Γ by considering the large deformation limit of a spinning bead.

C. Resolution using the finite element method

This section is devoted to the minimization of eqn (2) with the incompressibility condition (eqn (3)), using the Finite Element (FE) method.

We seek the displacement $\mathbf{u} = \mathbf{R} - \mathbf{r}$ by minimizing the augmented energy (eqn (2)) with the constraint $\det\mathbf{F} = 1$. This last condition is ensured by adding to eqn (2) the supplementary term

$$\int_{\Omega_0} p(\det\mathbf{F} - 1)\mathrm{d}V_0, \tag{15}$$

where p is a Lagrange multiplier to be computed together with $\mathbf{u}$. Because the solution is expected to be axially symmetric, the displacement vector is expressed in a cylindrical coordinate system as $\mathbf{u} = u_r(r,z)\mathbf{e_r} + u_z(r,z)\mathbf{e_z}$. For this two-dimensional problem in terms of r and z, the domain D we consider in the simulation is a disk of radius R_0 defined as $r^2 + z^2 < {R_0}^2$.

The FE formulation, implemented numerically using the FEniCS finite element library,[45] is here based on the research of the stationary points of the total energy functional given by eqn (2) with eqn (15). The displacement vector $\mathbf{u}$ and the Lagrange multiplier p are discretized using Lagrange FEs on a

View Article Online
Soft Matter Paper

triangular mesh. The nonlinear problem in the $(\mathbf{u}, p)$ variables is solved using a Newton algorithm based on a direct parallel solver (MUMPS,[46]) by setting $G_0 = 1$, $R_0 = 1$, $\Gamma = \beta$ and $\Delta\rho\omega^2 = \alpha$.

Quasi-static simulations are computed by progressively increasing the interfacial free energy β up to the desired dimensionless value, then by progressively incrementing the load parameter α, recording the displacement field and the Lagrange multiplier, and reaching convergence at each step. The equilibrium shape of the deformed body are obtained for a large range of parameters α, β (see Fig. 2 and 3).

Fig. 3 shows that the strain energy density is inhomogeneous in the sample, whereas it was assumed to be homogeneous within the biaxial in Section II.B. In Fig. 2, the values of $d_{\max}/d_{\min}$ calculated from the FE method and the biaxial approximation are compared. The biaxial approximation reproduces only qualitatively the deformation behaviour for small to moderate β (see Fig. 2 for $\beta = 0, 2$), converging quantitatively to the FE results only for larger values of β (*e.g.* $\beta = 4, 6$). Indeed, the biaxial approximation considers only the average deformation in the material instead of considering the local deformation, hence the observed discrepancies. This said, even if a quantitative analysis requires the use of the more precise FE calculation, the biaxial approximation provides a rigorous basis to understand bead deformation and the role played by interfacial stresses when elastic objects get deformed.

Inspired by the results obtained in the framework of the biaxial approximation (Section II.B), we focus on the large deformation limit. Our simulations still suggest that $d_{\max}/d_{\min}$ behaves as

$$d_{\max}/d_{\min} \sim a\sqrt{\alpha} + b \tag{16}$$

in the large deformation limit for any tested value of β (Fig. 4), where a and b are two fitting parameters. Interestingly, the variations of b as a function of β are far more pronounced than the variations of a, a result reminiscent with what was obtained in Section II.B (see eqn (14)).

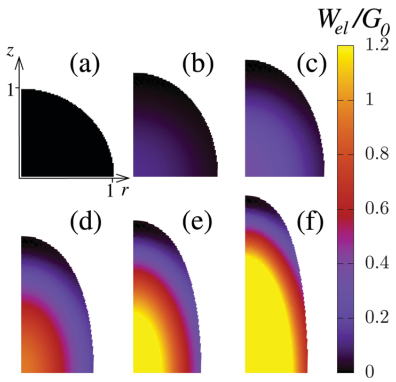

Fig. 3 Maps of the reduced strain energy density W_{el}/G_0 computed for $\beta = 1$ and different loads: $\alpha = 0$ (a), $\alpha = 5$ (b), $\alpha = 10$ (c), $\alpha = 20$ (d), $\alpha = 30$ (e) and $\alpha = 50$ (f). The corresponding values of $d_{\max}/d_{\min}$ are respectively equal to 1 (a), 1.3 (b), 1.6 (c), 2.0 (d), 2.4 (e), 3.0 (f). Unit-length is chosen so that initial configuration (a) is a disk of radius $R_0 = 1$. By symmetry, a quarter of the system is enough to completely characterize the deformed configurations of the bead.

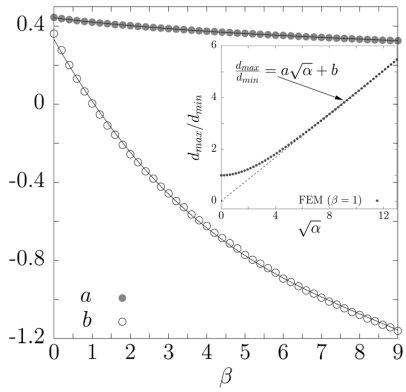

Fig. 4 $a(\beta)$ and $b(\beta)$ resulting from the fits of the large deformation limit of function $a\sqrt{\alpha} + b$ on $d_{\max}/d_{\min}$. The range for the fits is $d_{\max}/d_{\min} \in [2.5,6]$, in accordance with the domain explored in experiments detailed in Section III. Solid lines result from fourth order polynomial fits for $a(\beta)$ and $b(\beta)$ (see Table 1). Inset: $d_{\max}/d_{\min}$ calculated by the FE simulations as a function of $\sqrt{\alpha}$ for $\beta = 1$. $d_{\max}/d_{\min}$ is well approximated by the linear equation $d_{\max}/d_{\min} = a\sqrt{\alpha} + b$ in the large deformations limit.

Let us consider now experiments in which $d_{\max}/d_{\min}$ has been measured as a function of ω. In the regime of large deformations, we expect from eqn (16) the deformed shape of the spinning bead to follow $d_{\max}/d_{\min} \sim A\omega + B$. This is indeed observed for our polyacrylamide millimetric particles (see Fig. 7 and Section III for more details). Hence A and B can be, in principle, experimentally determined. In the other hand, we know from the results of the FE simulations that:

$$d_{\max}/d_{\min} \sim a(\beta)\sqrt{\alpha} + b(\beta) = a(\beta)\sqrt{\frac{\Delta\rho}{G_0}}R_0\omega + b(\beta). \tag{17}$$

By identifying A and B within eqn (17), we obtain:

$$\begin{cases} A = a(\beta)R_0\sqrt{\dfrac{\Delta\rho}{G_0}} \\ B = b(\beta). \end{cases} \tag{18}$$

Once the dependence of b on β is obtained from the FE solution, β can be determined. Then, from the first equation in (18), one can determine G_0 by performing a linear fit of the experimental data ($d_{\max}/d_{\min}$ *versus* ω) in the large deformation limit, and finally, the interfacial free energy can be calculated as $\Gamma = \beta R_0 G_0$. Once more, this shows that both the interfacial free energy Γ and the shear modulus G_0 of the bead can be extracted by fitting the bead deformation as a function of ω. To elucidate better the validity of eqn (16), $d_{\max}/d_{\min}$ is plotted as a function of $a(\beta)\sqrt{\alpha} + b(\beta)$ for different values of β (Fig. 5). $a(\beta)$ and $b(\beta)$ have been determined by considering deformations $d_{\max}/d_{\min}$ in the range [2.5,6], accordingly with the domain explored in experiments discussed in Section III. Even if the asymptotic regime is never strictly reached in this range for any β, the linear approximation of $d_{\max}/d_{\min}$ as function of $\sqrt{\alpha}$ remains

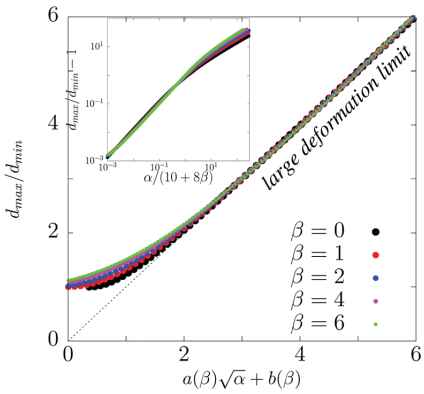

Fig. 5 d_{max}/d_{min} computed from the FE simulations as a function of $a\sqrt{\alpha} + b$ where a and b are determined as a function of β (see Fig. 4). Inset: $d_{max}/d_{min} - 1$ as a function of $\alpha/(10 + 8\beta)$.

Table 1 Coefficients K_i giving the best cubic polynomial fit of $a(\beta)$ and $b(\beta)$ shown in Fig. 4 and discussed in the main text

	K_1	K_2	K_3	K_4
$a(\beta)$	0.4422	−0.02848	1.69×10^{-3}	-6.65×10^{-5}
$b(\beta)$	0.3327	−0.3467	3.12×10^{-2}	-1.23×10^{-3}

very good. To make our results readily exploitable for future measurements, we have fitted separately $a(\beta)$ and $b(\beta)$ with a cubic function, namely $K_1 + K_2\beta + K_3\beta^2 + K_4\beta^3$. We report all values for the coefficients K_i in Table 1 and the result of the fit is shown in Fig. 4. The collapse of all curves in Fig. 5 confirms that the approximation $d_{max}/d_{min} \simeq a(\beta)\sqrt{\alpha} + b(\beta)$ is relevant for d_{max}/d_{min} in the experimental range.[2,6]

Finally it's worth noting that in the case $\alpha \ll 1$ (small deformation limit), the expression obtained from the biaxial approximation seems to hold well in the framework of the FE calculation (see inset of Fig. 5): all the deformations calculated for different β-values *via* FE method collapse on the bisector of the first quadrant when plotted *versus* the deformation obtained under biaxial approximation (eqn (11)). Indeed, matching the effective local deformation with the overall deformation of the bead is here relevant, because the material behaviour can be linearized within the limit of the small deformations.

III Experiments

A. Materials and methods

Polyacrylamide beads are prepared by copolymerization of acrylamide and *N*,*N*-methylenebisacrylamide in the presence of tetramethylenediamine (TEMED) and sodium persulfate as initiators, in water. Prior to mixing the constituents, all the solutions are saturated with nitrogen gas, to ensure the near insufficiency of oxygen. A given volume of the liquid mixture, corresponding to the radius of the bead, is transferred to an Eppendorf tube filled with the fluorinated oil in which all beads are solidly spun in our experiments. The aqueous droplets are small enough so that interfacial free energy ($\simeq 33 \pm 3$ mN m^{-1} measured by SDT in absence of crosslinker) made them spherical in oil. The polymerization and interchain crosslinking stopped after approximately 2 hours. The crosslinker and the acrylamide monomer concentrations were fixed respectively to 0.00119 ± 0.0006 mol l^{-1} and 0.45 ± 0.01 mol l^{-1} for all preparations. The same preparation protocol has been previously employed in our group to synthesize beads in silicon oil with shear modulus ranging from 13 Pa to 29 Pa.[10] Hence hereafter we will not consider any crosslinker and/or monomer density variation in the beads, whose effects will be possibly investigated in a future publication.

However, although the beads have been produced with the same protocol, we expect to find differences in their properties due to small uncontrolled variations affecting the preparation protocol and concerning the crosslinker/monomer molar ratio, the crosslinker and monomer concentrations, the presence of oxygen during the synthesis and the purity of the components. Since we consider beads characterized by low mass fractions of acrylamide, their mass density can be considered equal to the density of water at $T = 25$ °C, $\rho_i = 0.997$ g cm^{-3}.

All experiments were performed with a Krüss spinning drop tensiometer (SDT). Rates of rotation were accurate to 1%. The outer liquid, Fomblin Y oil [linear formula $CF_3O[-CF(CF_3)-CF_2O-]_x(-CF_2O-)_yCF_3$] of mass density $\rho_o = 1.9$ g cm^{-3} was purchased from Sigma-Aldrich and used without further purification at 25.0 °C. The temperature of the setup was always set to 25.0 ± 0.5 °C and kept constant using a flow of temperature-controlled air.

All beads were illuminated by a blue Light Emitting Diode (LED) with a dominant emission wavelength of 469 nm. Measurements were performed using a cylindrical capillary with internal diameter $2R_c = 3.25$ mm. Video recording has been performed by using a CCD camera attached to the SDT with a field of view 6 mm × 4.5 mm and resolution 2.3 μm. Different tests were performed with rotation rates ranging from 6000 rpm to 15 000 rpm. For our beads/oil system the displacement of the drop off the rotation axis due to buoyancy was smaller than 7 μm for $\omega > 800$ rad s^{-1}, as calculated following ref. 47. Such unavoidable deviation due to buoyancy is therefore much smaller than the bead size and of the same order of magnitude of the resolution of the camera used for the visual inspection the equilibrium shapes of the beads. The effect of buoyancy can thus be neglected and the measured deformation for $\omega > 800$ rad s^{-1} can be considered as only originated from the balance between the external forcing and the response of the material.

Being the refractive index of the background fluid ($n_b = 1.299$) close to that of water, fluorescent labelling was needed to ensure sufficient optical contrast and track the bead deformation. Under the illumination of the blue LED light, fluorescein-rich beads appear as bright green-yellow regions, since the fluorescein adsorption and emission spectra (in polar solvents) are peaked at $\lambda \approx 485$ nm and $\lambda \approx 511$ nm,[32,48,49] respectively.

B. Analysis

Four beads (coded as B1, B2, B3, B4) have been tested in the SDT in the large deformation limit ($d_{max}/d_{min} > 2$). Fig. 6 shows one fluoresceinated bead (B1) under different forcing (from 6000 rpm to 15 000 rpm). For all beads we have extracted the parameter A and B from the relation $d_{max}/d_{min} = A\omega + B$ in the large deformation regime (see Fig. 7), and then, G_0 and Γ have been deduced following the procedure detailed in Section II.C (see Table 2).

To check further the validity of our approach for largely deformed beads, we have rescaled our experimental data with the same procedure already adopted for the theoretical values of d_{max}/d_{min} (Fig. 8). Fig. 8 shows all values of d_{max}/d_{min} obtained for different synthesis of polyacrylamide beads in function of the rescaled forcing $A\omega + B$. All data collapse on a master curve, showing that the large deformation limit is indeed reached in all cases. The accuracy of our model in describing the data shows that the interfacial energy does not depend on the surface area of the bead, excluding the presence of a Shuttleworth effect.[14]

The values of the interfacial free energy are found to be similar among the beads, with a weighted average of $\Gamma = 28.1 \pm 3.0$ mN m^{-1} (see Table 2). Error bars could be reduced by exploring larger values of ω, which was not possible with our SDT. Since our gels are in water, we compare the interfacial energies of the elastic beads and that of a droplet containing a non-crosslinked polyacrylamide solution at the same acrylamide molar concentration of the beads. Interestingly, we found $\Gamma_{liq} = 33 \pm 3$ mN m^{-1} for the liquid droplet. Our measurements are therefore compatible with a negligible contribution of the polymer network to the interfacial energy.

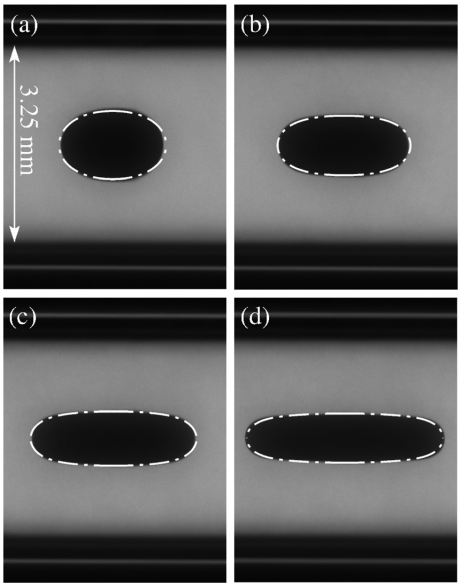

Fig. 6 Snapshots of sample B1 (details are given in Table 2) spinning with angular velocities 6000 rpm (a), 9000 rpm (b), 12 000 rpm (c) and 15 000 rpm (d). The observed deformation is correctly captured by the one obtained minimizing the total energy using the FE method (Section II.C), whose result is represented by the white dash-dotted lines. The corresponding values of the load are α = 27 (a), 60 (b), 107 (c) and 167 (d). The global deformations d_{max}/d_{min} are 1.6 (a), 2.2 (b), 3.0 (c) and 3.9 (d).

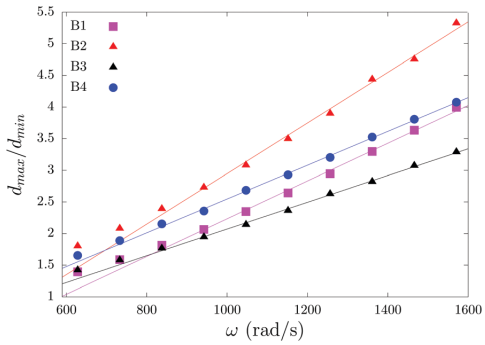

Fig. 7 d_{max}/d_{min} as a function of ω for four polyacrylamide beads with different radius R_0 and/or different shear modulus G_0. Solid lines are the results of linear fit $d_{max}/d_{min} = A\omega + B$ carried out for $\omega > 800$ rad s^{-1} (see Table 2).

As a final remark, we stress that the polymerization reaction used to synthesize the beads occurred into the background fluorinated oil used subsequently in SDT experiments. On the one hand, this ensures that the beads are not subject to a possible contamination that may arise from the synthesis in other immiscible media and that may affect subsequently the measurement performed in the SDT, notably the measured interfacial energy. On the other hand this oil inevitably alters the polymerization process, hence modifying the value of the gel modulus with respect to other similar synthesis already performed in our group.[10] This deviation, which can be significant for gels with low elastic modulus, is more pronounced as the contact surface between the aqueous solution and oil is larger. For this reason, we could not perform different types of synthesis like those carried out to produce macroscopic polyacrylamide gels,[10,50] whose modulus can be determined *via* other methods.[10,41] This hampered a direct cross-check of the values obtained for the shear modulus of our beads. Further research activity is being carried on in our group to develop a synthesis protocol enabling to crosscheck the measurement of elastic moduli obtained *via* a SDT. Despite of that, the values obtained with the SDT method seem relevant as they are in excellent agreement with those found *via* impact experiments[10] for similar polyacrylamide beads, suggesting that the bead deformation method under centrifugal forcing may serve as an ideal strategy to measure accurately both the elastic moduli and the surface energies of soft elastic materials.

4 Conclusions

Due to the interplay between bulk and surface forces acting simultaneously, isolating the effects of the solid–liquid

Table 2 Data obtained from the analysis of the measurements of d_{max}/d_{min} as a function of ω for the four tested samples. The reported uncertainties are the fit errors obtained using the nonlinear least-squares Marquardt–Levenberg algorithm, and according to the method described in Section II

Sample	R_0, mm	A, s	B	β	G_0, Pa	Γ, mN m^{-1}
B1	0.73 ± 0.01	$2.99 \times 10^{-3} \pm 0.07 \times 10^{-3}$	-0.75 ± 0.09	4.9 ± 0.6	7.1 ± 0.3	25.6 ± 4.4
B2	0.89 ± 0.01	$4.00 \times 10^{-3} \pm 0.01 \times 10^{-3}$	-1.05 ± 0.14	7.8 ± 1.6	5.1 ± 0.3	35.3 ± 8.9
B3	0.89 ± 0.01	$2.11 \times 10^{-3} \pm 0.04 \times 10^{-3}$	-0.042 ± 0.050	1.2 ± 0.2	27.8 ± 1.0	28.9 ± 5.0
B4	0.965 ± 0.010	$2.67 \times 10^{-3} \pm 0.04 \times 10^{-3}$	-0.13 ± 0.05	1.5 ± 0.2	16.4 ± 4.0	29.3 ± 10.0

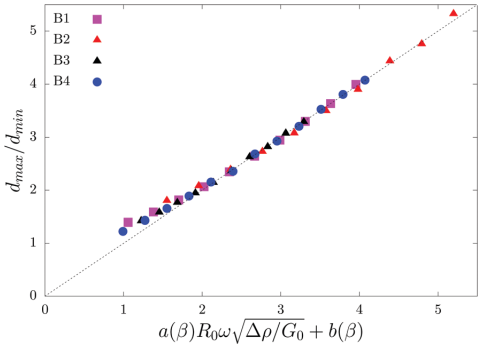

Fig. 8 d_{max}/d_{min} as a function of the rescaled angular velocity, for polyacrylamide beads with different radius and/or elastic modulus.

interfacial free energy constant of a soft solid is challenging. While for materials with large shear moduli the contribution of interfacial stresses to deformation can generally be safely neglected, the equilibrium shapes and the stability of soft solids under external drives are altered significantly by their ability to store and/or release interfacial energy. For such systems, measuring the shear modulus is also a difficult task since standard rheometric techniques are often confronted with experimental issues, like wall slip, edge fracture and instrumental resolution, hampering the accurate measurement of the material moduli. For this reason, a robust method able to measure unambiguously both the shear modulus and the interfacial free energy is highly desirable. In this paper we have shown that simultaneous measurements of the shear modulus and the interfacial free energy of elastic materials can be achieved without contact with a solid surface by analysing the shape of spinning soft beads. These measurements are based on a gradual variation of the load, *i.e.* of the angular velocity of the bead. This method requires the prior knowledge of the constitutive equation of the material. Here, in particular, we have investigated the case the isochoric neo-Hookean model, valid for polyacrylamide gels. We have shown that the deformation d_{max}/d_{min} of polyacrylamide beads is well approximated by a linear function of the angular speed for large deformations, supporting the validity of our model and the absence of any Shuttleworth effect.[14] We have measured the solid–liquid interfacial free energy for solid particles undergoing large deformations, and we have shown that, for these systems, the interfacial free energy is similar to the liquid–liquid interfacial tension measured in absence of elastic bulk forces. Our results corroborate a scenario where the deformation of soft amorphous polymer materials under an external load can be described considering one single interfacial free energy parameter independent on the deformation. Though it has been applied to one experimental system, our analysis suggests a much more general behavior of the interfaces between soft gels and newtonian fluids or gases, in line with previous results.[9,51,52] For materials following another known constitutive law (like the Gent model[53] or Mooney–Rivlin model[54]), the method described here also applies provided that this elastic law is accounted for in the simulations so that the functions $a(\beta)$ and $b(\beta)$ are properly determined. We hope that our work motivates further research both to improve and adapt SDT apparatus to the measurement of the elastic modulus of soft materials and to generalize our results to different elastic and viscoelastic systems.

Conflicts of interest

The authors state that there are no conflicts to declare.

Acknowledgements

CL and C-AC acknowledge partial financial support of the H2020 Program (Marie Curie Actions) of the European Commission's Innovative Training Networks (ITN) (H2020-MSCA-ITN-2017) under DoDyNet REA Grant Agreement (GA) No. 765811. The authors are most grateful to Jean Marc Fromental for providing technical help.

References

1 R. Style, A. Jagota, C. Hui and E. Dufresne, Elastocapillarity: surface tension and the mechanics of soft solids, *Annu. Rev. Condens. Matter Phys.*, 2017, **8**, 99–118.
2 J. Bico, E. Reyssat and B. Roman, Elastocapillarity: When surface tension deforms elastic solids, *Annu. Rev. Fluid Mech.*, 2018, **50**, 629–659.
3 C. Creton and M. Ciccotti, Fracture and adhesion of soft materials: a review, *Rep. Prog. Phys.*, 2016, **79**(4), 046601.
4 M. Nicolson, Surface tension in ionic crystals, *Proc. R. Soc. A*, 1955, **228**, 490–510.
5 S. Mora, T. Phou, J. M. Fromental, L. M. Pismen and Y. Pomeau, Capillarity driven instability of a soft solid, *Phys. Rev. Lett.*, 2010, **105**, 214301.
6 R. Style, C. Hyland, R. Boltyanskiy, J. Wettlaufer and E. Dufresne, Surface tension and contact with soft elastic solids, *Nat. Commun.*, 2013, **4**, 2728.

7 B. Andreotti, A. Marchand, S. Das and J. H. Snoeijer, Elastocapillary instability under partial wetting conditions: Bending *versus* buckling, *Phys. Rev. E: Stat., Nonlinear, Soft Matter Phys.*, 2011, **84**(6), 061601.
8 A. A. Evans, S. E. Spagnolie, D. Bartolo and E. Lauga, Elastocapillary self-folding: buckling, wrinkling, and collapse of floating filaments, *Soft Matter*, 2013, **9**(5), 1711–1720.
9 A. Chakrabarti and M. K. Chaudhury, Direct Measurement of the Surface Tension of a Soft Elastic Hydrogel: Exploration of Elastocapillary Instability in Adhesion, *Langmuir*, 2013, **29**(23), 6926–6935.
10 S. Arora, J. Fromental, S. Mora, T. Phou and C. Ligoure, Impact of beads and drops on a repellent solid surface: a unified description, *Phys. Rev. Lett.*, 2018, **120**, 148003.
11 M. Zhao, F. Lequeux, T. Narita, M. Roché and L. Limat, Growth and relaxation of a ridge on a soft poroelastic substrate, *Soft Matter*, 2018, **14**, 61–72.
12 S. Mondal, M. Phukan and A. Ghatak, Estimation of solid-liquid interfacial tension using curved surface of a soft solid, *Proc. Natl. Acad. Sci. U. S. A.*, 2015, **112**(41), 12563–12568.
13 B. Andreotti and J. Snoeijer, Soft wetting and the shuttleworth effect, at the crossroads between thermodynamics and mechanics, *EPL*, 2016, **113**, 66001.
14 R. Shuttleworth, The surface tension of solids, *Proc. Phys. Soc.*, 1950, **63**, 444–457.
15 P. Muller, Elastic effects on surface physics, *Surf. Sci. Rep.*, 2004, **54**(5–8), 157–258.
16 E. Orowan, Surface energy and surface tension in solids and liquids, *Proc. R. Soc. A*, 1970, **316**(1527), 473–491.
17 T. V. Savina, A. A. Golovin, S. H. Davis, A. A. Nepomnyashchy and P. W. Voorhees, Faceting of a growing crystal surface by surface diffusion, *Phys. Rev. E: Stat., Nonlinear, Soft Matter Phys.*, 2003, **67**(2), 021606.
18 A. Vaidya and M. K. Chaudhury, Synthesis and Surface Properties of Environmentally Responsive Segmented Polyurethanes, *J. Colloid Interface Sci.*, 2002, **249**(1), 235–245.
19 H. Hillborg, N. Tomczak, A. Olh, H. Schnherr and G. J. Vancso, Nanoscale Hydrophobic Recovery: A Chemical Force Microscopy Study of UV/Ozone-Treated Cross-Linked Poly(dimethylsiloxane), *Langmuir*, 2004, **20**(3), 785–794.
20 R. W. Style, A. Jagota, C.-Y. Hui and E. R. Dufresne, Elastocapillarity: Surface Tension and the Mechanics of Soft Solids, *Annu. Rev. Condens. Matter Phys.*, 2017, **8**(1), 99–118.
21 B. Andreotti and J. H. Snoeijer, Statics and Dynamics of Soft Wetting, *Annu. Rev. Fluid Mech.*, 2020, **52**(1), 285–308.
22 S. Mora, M. Abkarian, H. Tabuteau and Y. Pomeau, Surface instability of soft solids under strain, *Soft Matter*, 2011, **7**, 10612–10619.
23 C. Hui, A. Jogota, Y. Lin and E. Kramer, Constraints on microcontact printing imposed by stamp deformation, *Langmuir*, 2002, **18**, 1394–1407.
24 S. Mora, C. Maurini, T. Phou, J. M. Fromental, B. Audoly and Y. Pomeau, Solid drops: Large capillary deformations of immersed elastic rods, *Phys. Rev. Lett.*, 2013, **111**, 114301.
25 S. Mora and Y. Pomeau, Softening of edges of solids by surface tension, *J. Phys.: Condens. Matter*, 2015, **27**, 194112.
26 D. Paretkar, X. Xu, C. Y. Hui and A. Jagota, Flattening of a patterned compliant solid by surface stress, *Soft Matter*, 2014, **10**, 4084–4090.
27 A. Chakrabarti, M. K. Chaudhury, S. Mora and Y. Pomeau, Elastobuoyant heavy spheres: A unique way to study nonlinear elasticity, *Phys. Rev. X*, 2016, **6**, 041066.
28 J. Delavoipiere, Y. Tran, E. Verneuil and A. Chateauminois, Poroelastic indentation of mechanically confined hydrogel layers, *Soft Matter*, 2016, **12**, 8049.
29 B. Vonnegut, Rotating Bubble Method for the Determination of Surface and Interfacial Tensions, *Rev. Sci. Instrum.*, 1942, **13**(1), 6–9.
30 S. Bamberger, G. V. Seaman, K. Sharp and D. E. Brooks, The effects of salts on the interfacial tension of aqueous dextran poly(ethylene glycol) phase systems, *J. Colloid Interface Sci.*, 1984, **99**(1), 194–200.
31 Y. Liu, R. Lipowsky and R. Dimova, Concentration Dependence of the Interfacial Tension for Aqueous Two-Phase Polymer Solutions of Dextran and Polyethylene Glycol, *Langmuir*, 2012, **28**(8), 3831–3839.
32 A. Carbonaro, L. Cipelletti and D. Truzzolillo, Spinning Drop Dynamics in Miscible and Immiscible Environments, *Langmuir*, 2019, **35**(35), 11330–11339.
33 A. Carbonaro, L. Cipelletti and D. Truzzolillo, Ultralow effective interfacial tension between miscible molecular fluids, *Phys. Rev. Fluids*, 2020, **5**, 074001.
34 B. Zoltowski, Y. Chekanov, J. Masere, J. A. Pojman and V. Volpert, Evidence for the Existence of an Effective Interfacial Tension between Miscible Fluids. 2. Dodecyl Acrylate-Poly(dodecyl acrylate) in a Spinning Drop Tensiometer, *Langmuir*, 2007, **23**(10), 5522–5531.
35 J. A. Pojman, C. Whitmore, M. L. Turco Liveri, R. Lombardo, J. Marszalek, R. Parker and B. Zoltowski, Evidence for the Existence of an Effective Interfacial Tension between Miscible Fluids: Isobutyric Acid-Water and 1-Butanol-Water in a Spinning-Drop Tensiometer, *Langmuir*, 2006, **22**(6), 2569–2577.
36 G. Pieper, H. Rehage and D. Barth-Biesel, Deformation of a Capsule in a Spinning Drop Apparatus, *J. Colloid Interface Sci.*, 1998, **202**(2), 293–300.
37 D. D. Joseph, M. S. Arney, G. Gillberg, H. Hu, D. Hultman, C. Verdier and T. M. Vinagre, A spinning drop tensioextensometer, *J. Rheol.*, 1992, **36**(4), 621–662.
38 H. T. Patterson, K. H. Hu and T. H. Grindstaff, Measurement of interfacial and surface tensions in polymer systems, *J. Polym. Sci., Polym. Symp.*, 2007, **34**(1), 31–43.
39 R. Ogden, *Non-Linear Elastic Deformations*, Ellis Horwood Limited, Chichester, 1984.
40 J. Li, Y. Hu, J. Vlassak and Z. Suo, Experimental determination of equations of state for ideal elastomeric gels, *Soft Matter*, 2012, **8**, 8121.
41 S. Mora, E. Ando, J. Fromental, T. Phou and Y. Pomeau, The shape of hanging cylinders, *Soft Matter*, 2020, **15**, 5464–5473.
42 J. Hegemann, H.-H. Boltz and J. Kierfeld, Elastic capsules at liquid-liquid interfaces, *Soft Matter*, 2018, **14**(27), 5665–5685.

43 C. Wischnewski, E. Zwar, H. Rehage and J. Kierfeld, Strong Deformation of Ferrofluid-Filled Elastic Alginate Capsules in Inhomogenous Magnetic Fields, *Langmuir*, 2018, **34**, 13534–13543.

44 F. Richard, A. Chakrabarti, B. Audoly, Y. Pomeau and S. Mora, Buckling of a spinning elastic cylinder: linear, weakly nonlinear and post-buckling analyses, *Proc. R. Soc. A*, 2018, **474**, 20180242.

45 A. Logg, K. Mardal and G. Wells, *Automated Solution of Differential Equations by the Finite Element Method*, Springer, 2012.

46 P. Amestoy, I. Duff, J. L'Escellent and J. Koster, A fully asynchronous multifrontal solver using distributed dynamic scheduling, *SIAM J. Matrix Anal. Appl.*, 2001, **23**, 15–41.

47 P. Currie and J. Van Nieuwkoop, Buoyancy effects in the spinning-drop interfacial tensiometer, *J. Colloid Interface Sci.*, 1982, **87**(2), 301–316.

48 J. Panchompoo, L. Aldous, M. Baker, M. I. Wallace and R. G. Compton, One-step synthesis of fluorescein modified nano-carbon for Pd(ii) detection *via* fluorescence quenching, *Analyst*, 2012, **137**(9), 2054.

49 L. Szalay and E. Tombcz, Effect of the solvent on the fluorescence spectrum of trypaflavine and fluorescein, *Acta Phys. Acad. Sci. Hung.*, 1964, **16**(4), 367–371.

50 A. Chakrabarti, A. Porat, E. RaphaÃÂ«l, T. Salez and M. K. Chaudhury, Elastowetting of Soft Hydrogel Spheres, *Langmuir*, 2018, **34**(13), 3894–3900.

51 X. Shao, J. R. Saylor and J. B. Bostwick, Extracting the surface tension of soft gels from elastocapillary wave behavior, *Soft Matter*, 2018, **14**(36), 7347–7353.

52 X. Shao, S. A. Fredericks, J. R. Saylor and J. B. Bostwick, A method for determining surface tension, viscosity, and elasticity of gels via ultrasonic levitation of gel drops, *J. Acoust. Soc. Am.*, 2020, **147**, 2488–2498.

53 A. Gent, A new constitutive relation for rubber, *Rubber Chem. Technol.*, 1996, **69**, 59–61.

54 M. Mooney, A theory of large elastic deformation, *J. Appl. Phys.*, 1940, **11**, 582–592.

Part II

Hydrodynamic instabilities

Chapter 5

Instability of viscosity-stratified flows

"... nor could I then perceive any possible way in which instability could result from viscosity."

O. Reynolds

5.1 Theoretical background

As we have discussed in Chapter 1, the absence of consensus in the literature on the nature of Korteweg stresses [27–29] is due to the variety of experimental results obtained with different techniques, and it is thus crucial to tackle this problem from different angles in order to obtain a complete understanding. Therefore, exploiting different techniques is of fundamental importance for understanding the intimate nature of Korteweg stresses. We introduce here the study of the hydrodynamic instability of viscosity-stratified flow as a possible technique to investigate the EIT at the interface between two fluids. The importance of interfacial tension on stability makes this an interesting way to characterize capillary phenomena, such as for the case of tha Saffman-Taylor instability [7, 26, 27].

The stability of fluid flows constitutes a problem of paramount importance for phenomena ranging from pipe flow and oil recovery to the convection of magma currents in the Earth's mantle, and its study constitutes a classical area of research in fluid dynamics. In 1923, before concentrating on the development of quantum mechanics, Werner Heisenberg dedicated his doctoral dissertation to the "Stability and turbulence of fluid flows" [49]. When studying such a stability problem, the effect of viscosity was initially overlooked under the assumption that, even if a viscous effect was present, it would constitute a source of stabilization since it would contribute to energy dissipation. However, even if it is true that viscous dissipation tends to stabilize the flow, the presence of viscous stratification can have a non trivial effect, resulting in a net destabilization [50], and should not be neglected in general. Nevertheless, the original inviscid stability theory can provide insight on some general aspects and stability criteria, as well as on the importance of viscosity stratification itself. In the following, we will briefly discuss the linear stability of viscous parallel fluid

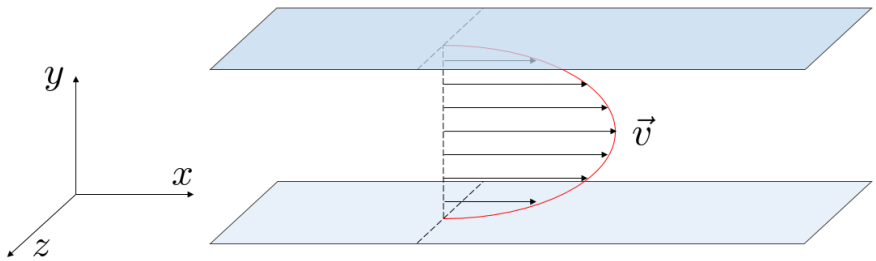

Figure 5.1: Scheme of the general flow under consideration. In particular, we are interested in a quasi-parallel flow, in which the velocity component along y is small, such as in the case of a flow between two parallel plates. The experimental case under study will be that of a coflow in a rectangular duct, limited along z as well.

flows, recalling the principal equations and results. The fundamental equation of inviscid instability theory (Rayleigh's equation) will be obtained as a limiting case of the more general viscous description, in order to elucidate the effect of viscosity stratification [51].

5.1.1 Viscous stability theory of parallel flows

In order to describe the instability of a fluid flow is in general sufficient to consider a two-dimensional flow, as a consequence of Squire's theorem (which will be discussed below). Nevertheless, we will start by considering a general three-dimensional single flow with the aim of elucidating the main properties of viscous instability. As will be detailed in Sec. 5.1.3, the stability analysis of single fluid flow constitutes the building block for parallel two-fluid flow stability as well, and is thus interesting for describing our experimental case of two fluids flowing parallel one to the other. In the following, we will build on the analysis in Ref. [51], to which the reader is referred for details.

Let us consider a fluid moving in a cartesian reference frame with $\vec{v} = u\hat{\mathbf{i}} + v\hat{\mathbf{j}} + w\hat{\mathbf{k}}$. x, y and z are the streamwise, wall-normal and spanwise directions respectively, as sketched in Fig. 5.1. In order to non-dimensionalize the system of equations, we rescale all spatial coordinates with a characteristic length L, and all velocity components (u, v, w) with a characteristic velocity $\bar{U}$ (e.g. the velocity of the unperturbed base flow, see below). The non-dimensional momentum equation can be written as [51]:

$$\frac{\partial u}{\partial t} + u\frac{\partial u}{\partial x} + v\frac{\partial u}{\partial y} + w\frac{\partial u}{\partial z} = -\frac{\partial p}{\partial x} + \frac{1}{Re}\nabla^2 u\,, \tag{5.1}$$

$$\frac{\partial v}{\partial t} + u\frac{\partial v}{\partial x} + v\frac{\partial v}{\partial y} + w\frac{\partial v}{\partial z} = -\frac{\partial p}{\partial y} + \frac{1}{Re}\nabla^2 v\,, \tag{5.2}$$

$$\frac{\partial w}{\partial t} + u\frac{\partial w}{\partial x} + v\frac{\partial w}{\partial y} + w\frac{\partial w}{\partial z} = -\frac{\partial p}{\partial z} + \frac{1}{Re}\nabla^2 w\,. \tag{5.3}$$

Furthermore, for an incompressible fluid we get the continuity equation

$$\frac{\partial u}{\partial x} + \frac{\partial v}{\partial y} + \frac{\partial w}{\partial z} = 0\,. \tag{5.4}$$

In order to characterize the flow instability, we split all quantities in a steady part and a small perturbation, such as

$$u(x,y,z,t) = U(x,y,z) + \epsilon\hat{u}(x,y,z,t)\,. \tag{5.5}$$

Here U is the steady component describing the base flow, $\hat{u}$ is the perturbation and ϵ a parameter that ensures the perturbation term to be small. Analogous equations can be written for v, w and p, so that the base velocity profile has components U, V and W. Furthermore, since we are interested in quasi-parallel flow, we take for the base velocity components $U = U(y)$, $V \approx 0$, $W = W(y)$. The component V could in principle be non null, as in the case of a boundary layer, but it grows weakly with y. Substituting Eq. 5.5 in the system (5.1-5.4), subtracting the equation for the unperturbed base flow and neglecting terms of second order in the perturbation quantities, we obtain the linearized disturbance equations. One gets at order $\mathcal{O}(\epsilon)$:

$$\frac{\partial\hat{u}}{\partial t} + U\frac{\partial\hat{u}}{\partial x} + W\frac{\partial\hat{u}}{\partial z} + \hat{v}\frac{\partial U}{\partial y} = -\frac{\partial\hat{p}}{\partial x} + \frac{1}{Re}\nabla^2\hat{u}\,, \tag{5.6}$$

$$\frac{\partial\hat{v}}{\partial t} + U\frac{\partial\hat{v}}{\partial x} + W\frac{\partial\hat{v}}{\partial z} = -\frac{\partial\hat{p}}{\partial y} + \frac{1}{Re}\nabla^2\hat{v}\,, \tag{5.7}$$

$$\frac{\partial\hat{w}}{\partial t} + U\frac{\partial\hat{w}}{\partial x} + W\frac{\partial\hat{w}}{\partial z} + \hat{v}\frac{\partial W}{\partial y} = -\frac{\partial\hat{p}}{\partial z} + \frac{1}{Re}\nabla^2\hat{w}\,, \tag{5.8}$$

$$\frac{\partial\hat{u}}{\partial x} + \frac{\partial\hat{v}}{\partial y} + \frac{\partial\hat{w}}{\partial z} = 0\,. \tag{5.9}$$

Equations (5.6-5.9) are then generally solved by means of normal mode analysis. The perturbation can be decomposed in Fourier modes, for which each quantity can be written as

$$\{\hat{u},\hat{v},\hat{w},\hat{p}\}^T = \iint \{f(y),\phi(y),h(y),\Pi(y)\}^T e^{i(\alpha x+\beta z-\omega t)}d\alpha d\beta\,. \tag{5.10}$$

Here ^{T} denotes the transpose vector, and $f(y)$, $\phi(y)$, $h(y)$ and $\Pi(y)$ express the y-dependence of the respective perturbation quantity. Depending on the kind of analysis that one wants to perform, the wave vectors α, β and the frequency ω can be taken to be either real or complex quantities. In temporal stability analysis, for instance, the wave vectors are real while the frequency is complex, so that its imaginary part ω_i is the growth rate of the individual mode considered, which will be unstable if $\omega_i > 0$. On the other hand, in spatial stability analysis α and β are complex while ω is real, and in spatio-temporal analysis all these quantities are complex. Insertion of Eq. 5.10 in (5.6-5.9) yields 4 coupled equations for the amplitudes f, ϕ, h, Π:

$$i\{\alpha U + \beta W - \omega\}f + U'\phi = -i\alpha\Pi + \frac{1}{Re}\{f'' - (\alpha^2+\beta^2)f\}\,, \tag{5.11}$$

$$i\{\alpha U + \beta W - \omega\}\phi = -\Pi' + \frac{1}{Re}\{\phi'' - (\alpha^2+\beta^2)\phi\}\,, \tag{5.12}$$

$$i\{\alpha U + \beta W - \omega\}h + W'\phi = -i\beta\Pi + \frac{1}{Re}\{h'' - (\alpha^2 + \beta^2)h\}\,, \tag{5.13}$$

$$i\{\alpha f + \beta h\} + \phi' = 0\,, \tag{5.14}$$

where for brevity the prime denotes differentiation along y. By multiplying Eq. 5.11 and 5.13 by α and β, respectively, combining the results with Eq. 5.14 and differentiating with respect to y, and finally introducing Eq. 5.12, one finds:

$$\phi^{iv} - 2\{\alpha^2+\beta^2\}\phi'' + \{\alpha^2+\beta^2\}^2\phi = iRe\{(\alpha U + \beta W - \omega)[\phi'' - (\alpha^2+\beta^2)\phi] - (\alpha U'' + \beta W'')\phi\}\,. \tag{5.15}$$

Equation 5.15 is the celebrated Orr-Sommerfeld equation [51], and is the building block of stability analysis. Together with the boundary conditions, it constitutes an eigenvalue problem for the disturbance: the solution of this problem yields the dispersion relation for the normal modes of the disturbance, relating α, β, ω, and Re. Given the complexity of Eq. 5.15, this is generally done numerically [52, 53].

In order to maintain generality, in formulating Eq. 5.15 we considered up to here a three-dimensional fluid flow with a three-dimensional disturbance. In practice, when looking for the critical Re for instability it is sufficient to consider two-dimensional disturbances by virtue of Squire's theorem [51]:

> *Squire's theorem for an inviscid fluid:* To each unstable three-dimensional disturbance there corresponds a more unstable two-dimensional one.

Even though it was originally stated for inviscid flow, this theorem holds in general also in the viscous case [53]. Considering a two-dimensional flow and a two-dimensional disturbance means setting $W = 0$, $\beta = 0$ in Eq. 5.15, which yields:

$$\phi^{iv} - 2\alpha^2\phi'' + \alpha^4\phi = iRe\{(\alpha U - \omega)[\phi'' - \alpha^2\phi] - \alpha U''\phi\}\,. \tag{5.16}$$

This simpler two-dimensional formulation of the Orr-Sommerfeld equation is equivalent to the three-dimensional one Eq. 5.15, in the case of parallel flow in one direction, for which $W = 0$. The equivalence can be seen using Squire's transformation [54]:

$$\tilde{\alpha}^2 = \alpha^2 + \beta^2\,, \qquad \omega\tilde{\alpha} = \tilde{\omega}\alpha\,, \qquad \tilde{Re}\tilde{\alpha} = Re\alpha\,. \tag{5.17}$$

As a consequence, a three-dimensional disturbance can be described as an equivalent bidimensional one, with a direction ψ in the xz plane (the direction of $\tilde{\alpha}$, see Fig. 5.2) determined by the respective magnitude of the wave vectors α and β; $\tilde{\omega}$ and $\tilde{Re}$ are then just adjusted accordingly. Furthermore, it is easy to verify that $|\tilde{\alpha}| > |\alpha|$, which means $\tilde{Re} = Re\frac{\alpha}{\tilde{\alpha}} < Re$. This constitutes a proof of Squire's theorem, since the two-dimensional disturbance will become unstable at lower Reynolds number than its three-dimensional counterpart. Consequently, the common procedure when analysing the instability of a flow is to consider only two-dimensional disturbances. To this end, Eq. 5.16 is solved numerically [52, 53].

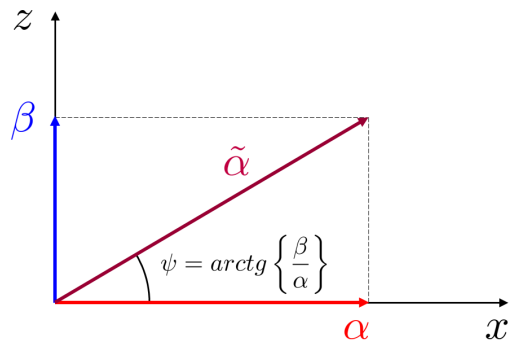

Figure 5.2: Direction of the equivalent bidimensional perturbation given by Squire's transformation. The angle ψ in the xz plane is determined by the magnitude of α and β.

5.1.2 Inviscid stability theory and role of viscosity stratification

In the previous section we derived the main equation describing flow instability in the viscous case, namely the Orr-Sommerfeld equation. Nevertheless, a brief discussion of the inviscid stability theory can give some insight on the role of viscosity, and in particular of viscosity stratification. Indeed, inviscid theory allows defining general criteria for instability which qualitatively apply also to the viscous case [50].

In the inviscid case, Eq. 5.16 becomes Rayleigh's equation:

$$(U - c)(\phi'' - \alpha^2\phi) - U''\phi = 0\,, \tag{5.18}$$

where $c = \frac{\omega}{\alpha}$ is the phase velocity of the perturbation wave. Inspection of Eq. 5.18 provides some interesting considerations. First, it is worth noting that while U is a real quantity, the phase velocity is in general complex, its imaginary part c_i being related to the growth rate of the disturbance, at least in temporal stability analysis. Nevertheless, in the case of neutral stability, $c_i = 0$, Eq. 5.18 becomes degenerate at the position in the flow field for which the velocity of the base flow equals the phase velocity of the perturbation, that is where $U = c$. Note that beyond this position the coefficients of Rayleigh's equation change sign. This position is named the *critical layer*. As will be discussed for a parallel coflow (see Sec. 5.1.3 below), it is the position at which the main part of the production of kinetic energy of the disturbance takes place.

Furthermore, from Rayleigh's equation one can obtain some general criteria for stability [51]. By multiplying Eq. 5.18 by ϕ^* and integrating along y, one obtains:

$$\int_{-\infty}^{+\infty} \phi^* \left[\phi'' - \alpha^2\phi + \frac{U''}{U - c}\phi\right] dy = 0\,. \tag{5.19}$$

Here we assume $c_i > 0$ so that Eq. 5.19 is non-singular. Integrating the first term by parts, and taking the disturbance to decay to zero at infinity so that its energy is finite, one finds

$$-\int_{-\infty}^{+\infty} \left[|\phi'|^2 + \alpha^2|\phi|^2\right] dy - \int_{-\infty}^{+\infty} \frac{U''(U - c)^*}{|U - c|^2}|\phi|^2 dy = 0\,. \tag{5.20}$$

Of the two integrals in Eq. 5.20, only the second has a complex part, yielding:

$$c_i \int_{-\infty}^{+\infty} \frac{U'}{|U-c|^2} |\phi|^2 dy = 0\,, \tag{5.21}$$

which is possible only if U'' changes sign in the domain of integration, that is if U has an inflection point. This is indeed a proof of a famous theorem by Rayleigh:

> *Rayleigh's inflection point theorem:* A *necessary* condition for instability is that the base velocity profile should have an inflection point.

Consideration of the real part of Eq. 5.20 provides a second theorem which is even more stringent (and whose derivation will not be reported here for brevity):

> *Fjørtoft's theorem:* A *necessary* condition for instability is that $U''\,[U - U(z_s)] < 0$ somewhere in the field of flow, where z_s is a point at which $U'' = 0$.

Both theorems provide only necessary conditions for instability, and not sufficient ones, although Tollmien argued that these conditions are sufficient for the cases of symmetric profiles in a channel and non-monotone ones of boundary layer type [51]. However, they provide a valuable tool to understand the role of viscous stratification. Indeed, if viscosity changes in the field of flow, it may introduce in the base velocity profile an important inflection point that is necessary for instability (see for instance Fig. 5.4 below). For such a reason in real systems viscosity stratification is an efficient way to enhance disturbance growth, while its absence typically results in stable flows at low Reynolds numbers.

5.1.3 Coflow instability and interfacial tension

Equation 5.15 was derived for a single fluid flow. Nevertheless, it constitutes the foundation of stability analysis also in the case of parallel coflow, namely the stratified flow of two fluids in a single channel. The study of this instability mode, completely originated by viscosity stratification, was initiated as early as 1967, when Yih showed that, when surface tension effects are neglected, plane Poiseille and plane Couette flows can be unstable to long-wavelength disturbances for however small Reynolds number [55]. In Yih's formulation, the two fluids were considered immiscible, and the interface was well-defined (Fig. 5.3). In such a configuration it is sufficient to consider the Orr-Sommerfeld equation in both layers together with the boundary conditions at the channel walls and at the interface, where continuity of velocity and stresses are required. Yih's results were later expanded by Yiantsios and Higgins [52], who showed that in presence of capillary effects at the interface the flow is not always unstable, and a stability region exists depending on the surface tension between the two fluids, the viscosity ratio between the two fluids, the position of the interface and the wave vector. The study of the edge of this stability region seems thus a promising strategy to measure indirectly the presence of an interfacial tension between the two fluids in the channel.

If the two fluids are miscible and there is no well-defined interface, it is not possible to write the Orr-Sommerfeld equation in the two layers separately. On the contrary, it becomes necessary to describe the system as a single fluid with variable viscosity $\eta = \eta(y)$.

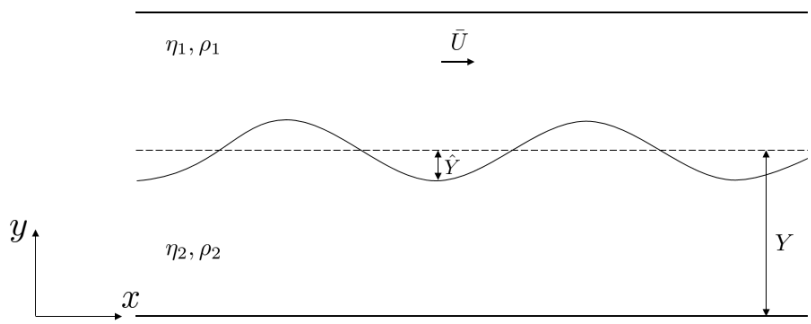

Figure 5.3: Scheme of the coflow instability. Y is the position of the unperturbed interface.

With the same procedure as in Sec. 5.1.1, dividing the viscosity in a base flow component and a perturbation one ($\bar{\eta}$ and $\hat{\eta}$, respectively), the Orr-Sommerfeld equation becomes [50]:

$$\begin{aligned} i\alpha Re\{[\phi'' - (\alpha^2+\beta^2)\phi](U-c) - U''\phi\} = \\ \bar{\eta}[\phi^{iv} - 2(\alpha^2+\beta^2)\phi'' + (\alpha^2+\beta^2)^2\phi] + 2\bar{\eta}'[\phi''' - (\alpha^2+\beta^2)\phi'] + \\ + \bar{\eta}''[\phi'' + (\alpha^2+\beta^2)\phi] - i\alpha U'[\hat{\eta}'' + \hat{\eta}(\alpha^2+\beta^2)] - 2i\alpha U''\hat{\eta}' - i\alpha U'''\hat{\eta}\,. \end{aligned} \tag{5.22}$$

Since the viscosity is not homogeneous, a second equation needs to be considered in order to completely describe the fluid motion. A common choice is Squire's equation for the vorticity θ [50]:

$$\theta(U-c) + \frac{\beta}{\alpha}U'\phi = \frac{1}{i\alpha Re}\{\bar{\eta}[\theta'' - (\alpha^2+\beta^2)\theta] + \bar{\eta}'\theta' + i\beta U'\hat{\eta}' + i\beta U''\hat{\eta}\}\,. \tag{5.23}$$

As for the case of the Orr-Sommerfeld equation in single fluid flow, equations (5.22-5.23) are generally solved numerically [53].

It is worth discussing one further consideration on the role of interfacial tension effects on the instability of parallel flow. Following Govindarajan and Sahu [50], one can write for the disturbance kinetic energy $\mathcal{E}$:

$$\frac{\partial \mathcal{E}}{\partial t} = \mathcal{P} - \mathcal{D} + \mathcal{T} + \mathcal{S}\,. \tag{5.24}$$

Here $\mathcal{P} = -\langle \hat{u}\hat{v}\rangle U'$ and $\mathcal{D} = \frac{1}{Re}\langle |\nabla\hat{u}|^2 + |\nabla\hat{v}|^2 + |\nabla\hat{w}|^2\rangle$ are the production and viscous dissipation of disturbance kinetic energy, while $\mathcal{T} = \nabla\cdot\left[-\frac{\langle\hat{u}\hat{p}\rangle}{\rho} + 2\frac{\hat{\eta}}{Re}\nabla\mathcal{E}\right]$ and $\mathcal{S} = \frac{\Gamma}{\rho L\bar{U}^2}\left\langle\left[\hat{v}\left(\hat{Y}_{xx} + \hat{Y}_{zz}\right)\right]_{y=Y}\right\rangle$ are the stress transport and surface tension effects, respectively. L and $\bar{U}$ are again characteristic length scale and velocity, Y is the position of the interface (and $\hat{Y}$ its perturbation). Equation 5.24 suggests a second possible way to take into account interfacial tension effects: Γ enters in the energy balance for the disturbance, altering the growth rate of the modes. By characterising the latter, one could in principle

measure the effect of the interfacial tension. Furthermore, while the energy production occurs mainly at the interface, the major part of viscous dissipation takes place close to the walls of the channel, where the non-slip boundary conditions impose zero velocity [53]. As a consequence, the energy balance of the disturbance depends on the position of the interface in the channel, a consideration that will be important in Sec. 5.3.

In the light of all previous considerations, it is worth underlining one further detail on the interest of parallel flow for studying experimentally the coflow instability. As we have already stated, the production of disturbance kinetic energy takes place mainly at the interface. This can be qualitatively understood for the case of two fluids having very different viscosities, for which the base velocity profile changes almost abruptly at the interface, and the most viscous fluid can be approximated as passive [52]. As a consequence, the critical layer is confined close to the interface itself, where the velocity of the base flow spans a wide range of values in a small region of space. This leads to a non trivial consideration when performing experiments: the stability of the flow is characterised by looking at the interface itself, which is easily observed due to the contrast in refractive index between the two fluids. Therefore, the interface is at the same time the place where the disturbance is generated and the quantity to be measured. On the experimental side, exploiting viscosity-stratified parallel flow is thus a natural and unique way to study this shear flow instability. The shape of the base velocity profile close to the interface has then a paramount importance for the production of disturbance kinetic energy, and its calculation will be detailed in the next section.

5.1.4 Base velocity profile (parallel Poiseille flow)

In deriving the Orr-Sommerfeld equation we considered the base velocity profile $\vec{V} = U\hat{\mathbf{i}} + V\hat{\mathbf{j}} + W\hat{\mathbf{k}}$ to be known. However, its shape, and in particular the presence of inflection points, is of paramount importance in determining the stability of the flow. Nevertheless, to our knowledge, no previous work shows the explicit expression of the three-dimensional velocity profile in the case of a parallel two-fluid flow. Therefore, in the following we will derive an expression for the shape of the base velocity profile in the case of parallel channel flow, relevant for our experiments. This will allow us to calculate $\vec{V}$ from our experimental parameters, such as the flow rate and the viscosities of the two fluids. Following the procedure of Ref. [56], we consider a reference frame with the origin in the lower left-hand corner of the channel cross section. The fluids flow in the positive direction of the streamwise coordinate x, and the channel covers the z direction in a range $0 < z < a$ and the vertical direction y in a range $0 < y < b$, with $a \neq b$ in general. As sketched in Fig. 5.4, $y = Y$ represents the vertical position of the interface between the two fluids. With this choice of the reference frame, the base profile flow will be of type $\vec{V} = U(y, z)\hat{\imath}$.

For the sake of simplicity, we consider the interface to be infinitely sharp by considering the fluids to be immiscible, following Yih's approximation [55]. Therefore, we write $U(y, z)$ as a piecewise solution to Navier-Stokes' equations in the two fluid layers:

$$U(y,z) = \begin{cases} U_1(y,z) & \text{for } 0 < y < Y,\ 0 < z < a \\ U_2(y,z) & \text{for } Y < y < b,\ 0 < z < a\,. \end{cases} \tag{5.25}$$

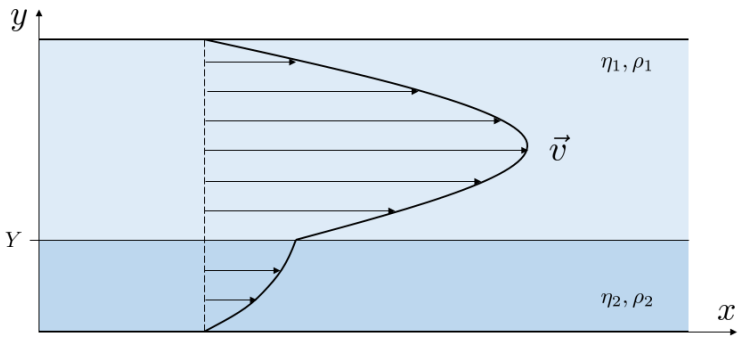

Figure 5.4: Scheme of the base velocity profile in parallel Poiseille flow: the two fluids flow in the regions $0 < y < Y$ and $Y < y < b$ respectively. In this representation, $\eta_2 > \eta_1$.

Assuming the fluids to be incompressible, in each layer $U_i(y, z)$ will satisfy the streamwise component of the Navier-Stokes equations:

$$\eta_i \nabla^2 U_i(y, z) = \frac{\partial p}{\partial x}\,, \tag{5.26}$$

where η_i is the dynamic viscosity. Imposing no-slip boundary conditions at the left and right boundaries of the channel ($U_i(y, 0) = U_i(y, a) = 0$), the solution to Eq. 5.26 is known to take the Fourier form [56]:

$$U_i(y, z) = \frac{\partial p}{\partial x}\left\{\frac{z(z-a)}{2\eta_i} + \sum_{m=1}^{\infty} \sin\left(\frac{m\pi z}{a}\right)\left[A_{i,m}\cosh\left(\frac{m\pi y}{a}\right) + B_{i,m}\sinh\left(\frac{m\pi y}{a}\right)\right]\right\}. \tag{5.27}$$

The coefficients $A_{i,m}$, $B_{i,m}$ are found by imposing the boundary conditions for the flow, namely no-slip conditions at the channel walls:

$$U_i(0, z) = U_i(b, z) = 0 \tag{5.28}$$

and the continuity of velocity and shear stress across the interface, i.e.:

$$U_1(Y, z) = U_2(Y, z)\,, \tag{5.29}$$

$$\eta_1 \frac{\partial U_1(y, z)}{\partial y} = \eta_2 \frac{\partial U_2(y, z)}{\partial y}\,. \tag{5.30}$$

It is worth noting that since the shear stress is continuous across the interface, the derivative of the base velocity profile is not. Inserting Eqs. (5.28-5.30) in 5.27, one finds for the coefficients $A_{i,m}$, $B_{i,m}$:

$$A_{1,m} = \frac{K_m}{\eta_1}\,, \tag{5.31}$$

$$B_{1,m} = \frac{K_m}{\eta_1 C_m}\left\{2\eta_1 - S\cosh\left(\frac{bm\pi}{a}\right) + D\left[\cosh\left(\frac{(b-2Y)m\pi}{a}\right) - 2\cosh\left(\frac{(b-Y)m\pi}{a}\right)\right]\right\}, \tag{5.32}$$

$$A_{2,m} = \frac{K_m}{\eta_2 C_m}\left\{2\left[\eta_2 + D\cosh\left(\frac{Ym\pi}{a}\right)\right]\sinh\left(\frac{bm\pi}{a}\right) - D\sinh\left(\frac{2Ym\pi}{a}\right)\right\}, \tag{5.33}$$

$$B_{2,m} = \frac{K_m}{\eta_2 C_m}\left\{S - 2\cosh\left(\frac{bm\pi}{a}\right)\left[\eta_2 + D\cosh\left(\frac{Ym\pi}{a}\right)\right] + D\cosh\left(\frac{2Ym\pi}{a}\right)\right\}, \tag{5.34}$$

with $S = \eta_1 + \eta_2$ and $D = \eta_1 - \eta_2$ the sum and the difference of the two viscosities, respectively. The coefficients K_m and C_m are given by

$$K_m = \frac{2a^2\left[1-(-1)^m\right]}{m^3\pi^3}, \tag{5.35}$$

$$C_m = S\sinh\left(\frac{bm\pi}{a}\right) + D\sinh\left(\frac{(b-2Y)m\pi}{a}\right). \tag{5.36}$$

The interface position Y can be measured experimentally, so that the velocity profile can be computed numerically. In order to do so, it is necessary to compute the pressure gradient $\frac{\partial p}{\partial x}$ as well, which is not known a priori: the experimental parameter are actually the flow rates of the fluids in the channel, Q_1 and Q_2. However, the latter can be related to the pressure gradient, once the interface position is known. The total flow rate $Q = Q_1 + Q_2$ in the channel is simply the integral of the velocity profile:

$$Q = \int_0^b \int_0^a U(y,z)dydz = \frac{\partial p}{\partial x}\int_0^b \int_0^a \tilde{U}(y,z)dydz, \tag{5.37}$$

where we define $\tilde{U}(y,z) = {}^{U(y,z)}/_{\frac{\partial p}{\partial x}}$. Therefore, instead of computing $U(y,z)$ one can compute $\tilde{U}(y,z)$ first and integrate the latter in order to obtain the value of the pressure gradient from the flow rate Q. Moreover, the same procedure can be performed separately for the two fluids, since we deal with stationary flows and hence the same pressure gradient appears in the two $U_i(y,z)$ and the total flow rate is simply the sum of the two individual flow rates of the fluids. One then finds:

$$Q_1 = \int_0^Y \int_0^a U_1(y,z)dydz = \frac{\partial p}{\partial x}\int_0^Y \int_0^a \tilde{U}_1(y,z)dydz, \tag{5.38}$$

$$Q_2 = \int_Y^b \int_0^a U_2(y,z)dydz = \frac{\partial p}{\partial x}\int_Y^b \int_0^a \tilde{U}_2(y,z)dydz. \tag{5.39}$$

Equation 5.37 and Eqs. (5.38-5.39) allow one to compute the pressure gradient in two independent ways and thus to verify the accuracy of the analysis of the experimental data. As an example, Fig. 5.5 shows the base velocity profile for a parallel flow of water and triethylene glycol in a squared channel, calculated with Eq. 5.27. The interface between the two fluids corresponds to the rapid change in slope of the velocity profile. Such calculated velocity profiles allow us computing the value of all flow-related quantities in our experimental conditions, such as $U'(y = Y)$ and Re, whose importance will be discussed in Sec. 5.3.

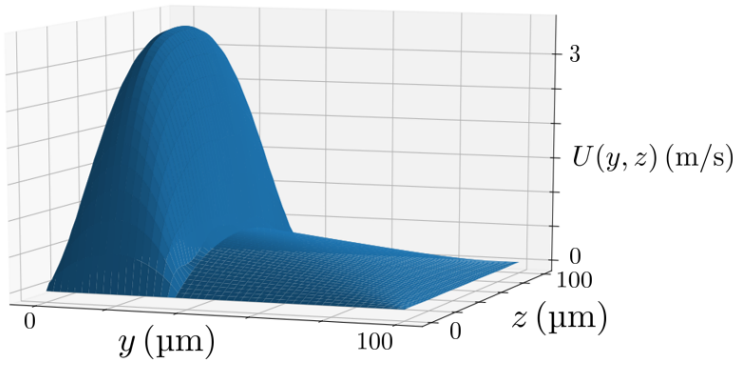

Figure 5.5: Example of a base velocity profile, calculated from Eq 5.27, for the case of parallel flow of water and triethylene glycol (TEG), in a squared channel with sides $h = w = 100\,\mu\text{m}$. The rapid change of velocity at the interface, where the profile has also an inflection point, is clearly visible.

5.2 Materials and methods: microfluidics setup

Experiments on the instability of viscosity-stratified flows were performed in polydimethylsiloxane (PDMS) microchannels. Since PDMS offers an easy fabrication and is optically transparent, it is widely used for micofluidics applications. The channels are formed in a mold obtained on a silicon wafer by means of photolithography. A liquid mixture of PDMS and crosslinker is poured on the mold and cured overnight at 70°C. Then, the solid PDMS is peeled from the mold and covalently attached to a microscope slide by means of plasma oxidation [57]. In order to inject and discharge the fluids, teflon microtubes (Scientific commodities Inc.) were plugged in the inlets and outlets by punching small holes in the PDMS, which constitutes the side and upper boundaries of the microchannels. The whole system is visualized by means of optical microscopy.

We use Y-junction channels, as shown in Fig. 5.6. The channels are constituted by a rectangular main duct of height a and width b, and two inlets having the same height and half of the width of the main duct, and forming an angle of 43.6° between them. The two fluids flow parallel to each other and the interface is vertical, so that it can be easily visualized under a microscope thanks to the difference in refractive index. Furthermore, this configuration allows ruling out the effect of gravity, at least in the first portion of the channel, before the two fluids reorient themselves due to their different densities. The two fluids are pushed in the channel by means of two individual Harvard Apparatus syringe pumps working at constant flow rates Q_1 and Q_2, respectively. The use of two separate pumps allows one to separately impose the flow rate of the two fluids, and thus to characterise the coflow instability at different values of Q_1, Q_2 and Reynolds number. After starting the injection or changing the flow rate, we wait several minutes for the system to reach a stationary state before acquiring data, in order to avoiding transient effects due to the compliance of the injection apparatus and of the teflon tubing.

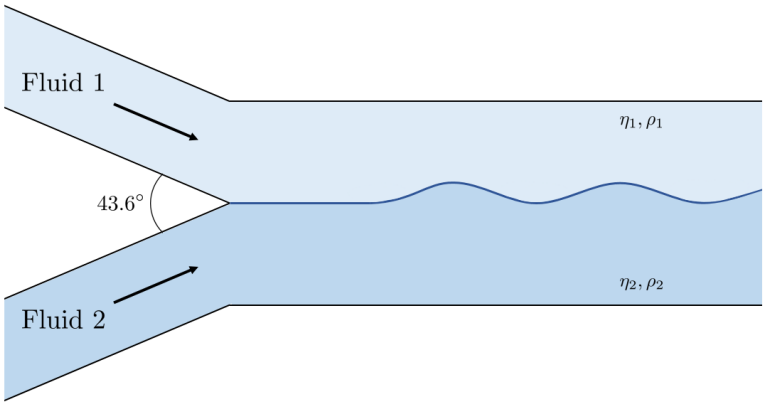

Figure 5.6: Scheme of the Y-junction channels. The two fluids are injected from two inlets at the left and ejected through one single outlet.

To visualize the instability, we use an inverted optical microscope (Leica DM IRB) equipped with a high-speed CCD camera (Phantom Miro M310). To record the videos we typically use a frame rate of 300 frames per second. Figure 5.7 shows a picture of the complete setup.

5.2.1 Numerical calculation of the base velocity profile

The velocity profile of the base flow defined in Sec. 5.1.4 is calculated numerically using a Python script, available at [46]. Inspection of Eq. 5.27 and of the coefficients $A_{i,m}$, $B_{i,m}$ highlights the presence of hyperbolic functions that rapidly diverge at high aspect ratios of the channel, $\frac{b}{a}$. As a consequence, care must be taken when computing the shape of the base velocity profile. First, we exploit arbitrary-precision floating point arithmetic in order to prevent overflow, using the Python library *mpmath*. Second, we cross-check the accuracy of the calculation by means of the following argument. As already noted by Yiantsios and Higgins [52], when one of the two fluids is much more viscous than the other, the former can be taken as being almost passive, and the flow may be approximated as a single fluid flow of the less viscous fluid. This is equivalent to considering the less viscous fluid as flowing in an equivalent channel of reduced cross-section, of height a and width Y, the distance between the interface and the channel wall. This is an excellent approximation, for instance, in the case of glycerol flowing parallel to water. Interestingly, the equivalent single fluid flow problem has fewer problems of convergence, since it takes place in a "channel" of smaller aspect ratio. Therefore, we verified the accuracy of the numerical calculation of the base velocity profile in the channel by calculating the velocity profile of the equivalent single fluid flow.

5.2.2 Determination of disturbance wavelength and phase velocity

In order to experimentally characterise the instability, we impose the flow rates Q_1 and Q_2 of the fluids and film the interface by means of a high speed camera. Even if we aim

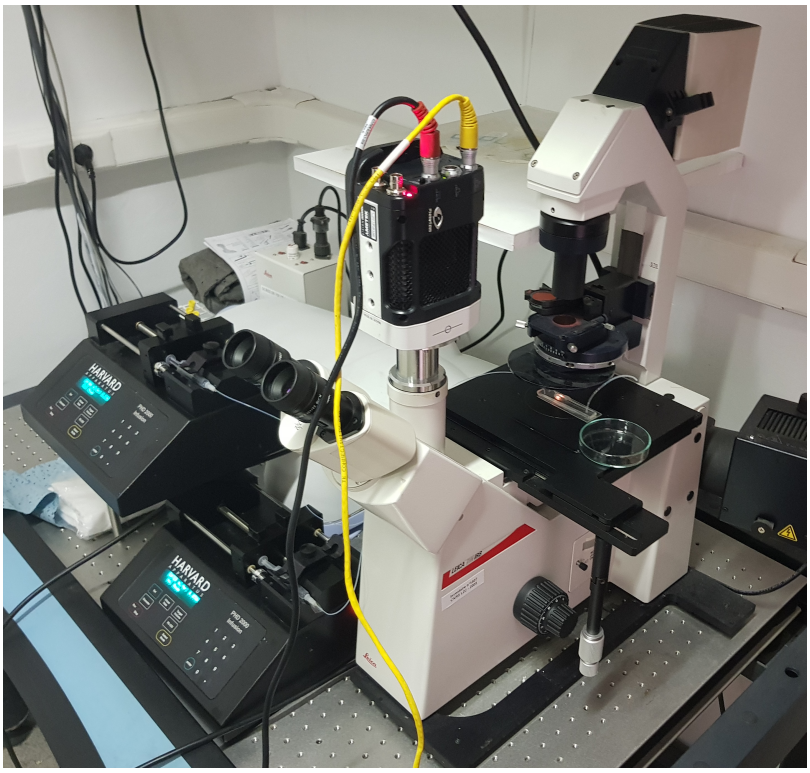

Figure 5.7: Picture of the setup used for the measurements of the coflow instability. The two fluids are pushed in the channel by two independent syringe pumps, and the channel is imaged on an inverted microscope equipped with a fast acquisition camera.

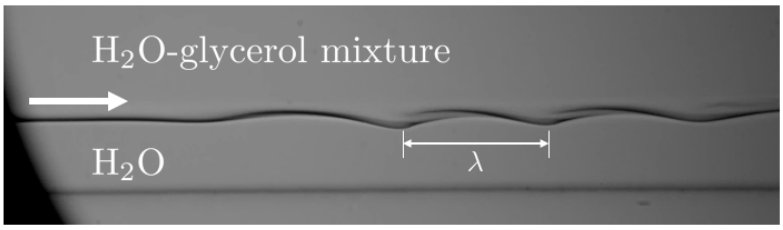

Figure 5.8: Image of the coflow instability at the interface between water, flowing at 250 µL/ min, and a mixture of water and glycerol with glycerol concentration 93% wt/wt, flowing at 15 µL/ min. Both fluids flow from left to right of the image.

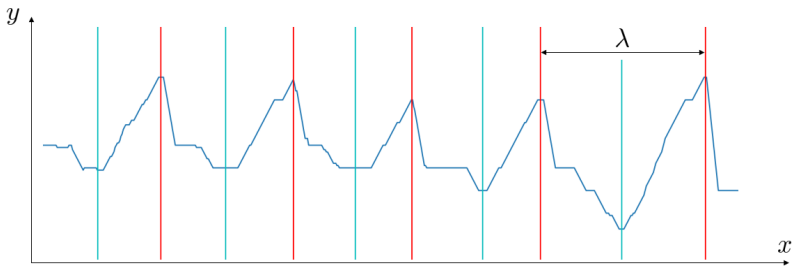

Figure 5.9: Profile of the instability for the case of water flowing at 60 µL/ min parallel to glycerol, flowing at 3 µL/ min. The positions of the peaks and valleys detected by the image analysis code are showed in red and cyan, respectively.

at studying the stationary state, filming the instability for several seconds allows us to characterize any time-changing behaviour of the waves. As an example, Fig. 5.8 shows one frame of the videos that we obtain in this way, for the case of parallel flow of water ($Q_{H_2O} = 250$ µL/ min) and a mixture of water and glycerol with a glycerol mass fraction of 93% ($Q_{mixt} = 15$ µL/ min). From the videos we extract the wavelength and phase velocity of the waves, as well as the distance between the interface and the channel wall, by means of a Python script, available at [46]. As seen in Fig. 5.8, the interface can be clearly identified thanks to the difference in refractive index between the two fluids. This allows one reconstructing the shape of the wave front in each frame by tracking the vertical position y of the minimum intensity point at each horizontal coordinate x, thus obtaining a curve in the xy plane which closely represents the contour of the deformed interface. Figure 5.9 shows an example of such a curve. For the case of a wave which is short enough for several wavelengths to fit in the field of view, the wavelength and amplitude of the instability can be extracted by measuring the distance between adjacent local maxima and minima of the signal in the horizontal and vertical direction, respectively. As an example and to show the accuracy of this image analysis routine, the positions of peaks and valleys of the disturbance are represented in Fig. 5.9 as red and cyan line, respectively. The phase velocity of the wave is obtained by tracking the position of either the maxima or the minima from one frame to the following one, and measuring the distance that they travelled, the frame rate being known. Uncertainties on wavelength, amplitude and phase velocity are obtained from the respective time variations over the duration of the videos.

In some cases, as will be further discussed in Sec. 5.3, the interface develops a disturbance of long wavelength, and a single oscillation appears in the field of view. In such a case we cannot measure the disturbance wavelength from the distance between successive extrema and we have to use a different procedure. The phase velocity can still be obtained in the usual way. Then, the wavelength can be calculated by comparing the position of one extremum (e.g. a minimum) at time t_1 with the one of the following one, taken at a later time t_2. At t_2 the first minimum will not be visible any more, which makes impossible to directly measure the distance between it and the second one. Nevertheless, the position of the first minimum can be estimated from its position at time t_1, the elapsed time

$\Delta t = t_2 - t_1$ and the phase velocity of the wave.

5.3 Results and discussion

To set the scene of the general phenomenology of coflow instabilities, Fig. 5.10 shows three images for the case of water flowing parallel to glycerol. Both fluids flow from right to left, with glycerol occupying the upper part of the channel. In all Panels glycerol flows at 12 µL/min, while the flow rate of water increases from Panel A to Panel C: 65 µL/min (A), 200 µL/min (B), 350 µL/min (C). Remarkably, the wavelength of the instability does not depend monotonically on the flow rate of water. On the contrary, it is evident from Fig. 5.10 that the wavelength increases at first, with larger wavelengths developing as the flow rate is increased from small to intermediate ones, while at higher flow rates the waves become shorter. The dependence of the wavelength of the instability on the flow rate of water Q_{H_2O} for the images of Fig. 5.10 with $Q_{gly} = 12$ µL/min is reported in Fig. 5.11. The presence of a maximum at a non-zero value of Q_{H_2O} is evident.

Remarkably, the same phenomenology is observed when the flow rate of glycerol is varied, as reported in Fig. 5.12. Here individual curves represent different values of glycerol flow rate: for each line, Q_{gly} is kept fixed while Q_{H_2O} is varied. As Q_{gly} increases, the maximum in wavelength becomes more evident, shifting to higher water flow rates as well. It is worth noting the order of magnitude of the wavelength of the instability: at high glycerol flow rates the waves reach almost 2 mm in wavelength, in a channel of 1 mm in width, and 100 µm in height. Being the phenomenology so general, it is interesting to investigate the origin of the two opposite trends seen at small and large flow rates, which give rise to the maximum in wavelength λ.

In order to investigate the two regimes of λ versus Q_{H_2O}, we start by characterizing the dispersion relation of the instability from the measured wavelength and phase velocity of the waves. Figure 5.13a shows the values of ω versus wave vector k for all data in Fig. 5.12. Interestingly, two different branches can be observed in the dispersion relation. Figure 5.13b shows for clarity only one series of data, the one corresponding to the experiments reported in Fig. 5.11 with $Q_{gly} = 12$ µL/min. The two branches in $\omega(k)$ are clearly distinguishable. In particular, the lower, horizontal branch corresponds to the experiments at small water flow rate, below the maximum in λ. The upper branch corresponds to larger flow rates, above the maximum wavelength. The markedly different shape of $\omega(k)$ at small and large Q_{H_2O} strongly supports the conclusion that two different phenomena are at play, giving rise to the non-monotonic behaviour of $\lambda(Q_{H_2O})$.

As a first attempt to interpret the experimental data, one could therefore think that the two wavelength regimes correspond to two distinct instabilities and are induced by two different excitation modes, such as the viscosity-stratification instability mode studied by Yih, and Tollmien-Schlichting modes. However, the latter develop at high Reynolds numbers, generally above 10000 [52,53]. We can obtain the value of Re in our experiments by solving numerically the velocity profile in the channel as described in Sec. 5.1.4. The position of the interface in the channel is measured experimentally, and knowing the two flow rates allows one to compute the velocity of the fluids. In order to asses whether or not one of the two regimes in λ could be induced by Tollmien-Schlichting waves, we compute

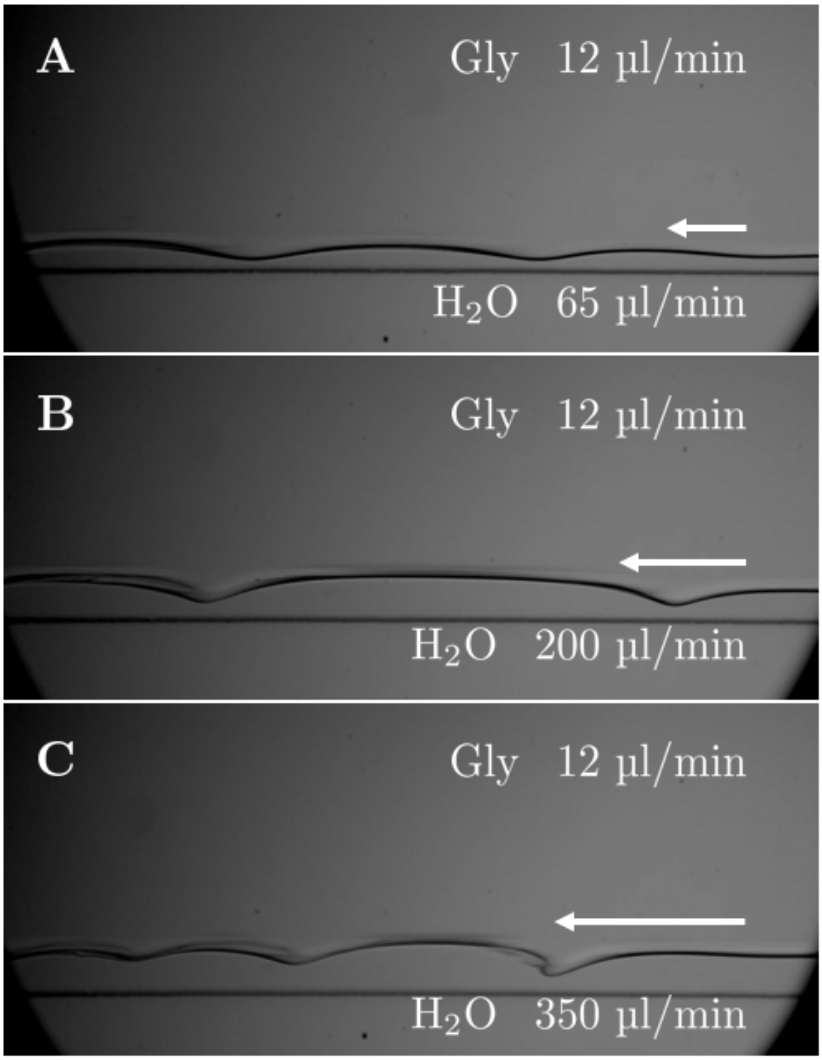

Figure 5.10: Experimental images of the coflow instability between water and glycerol. Both fluids flow from right to left, with glycerol flowing at $Q_{gly} = 12\,\mu\text{L/min}$ in the upper part of the channel. The flow rate of water is $65\,\mu\text{L/min}$ in panel A, $200\,\mu\text{L/min}$ in panel B, and $350\,\mu\text{L/min}$ in panel C, respectively.

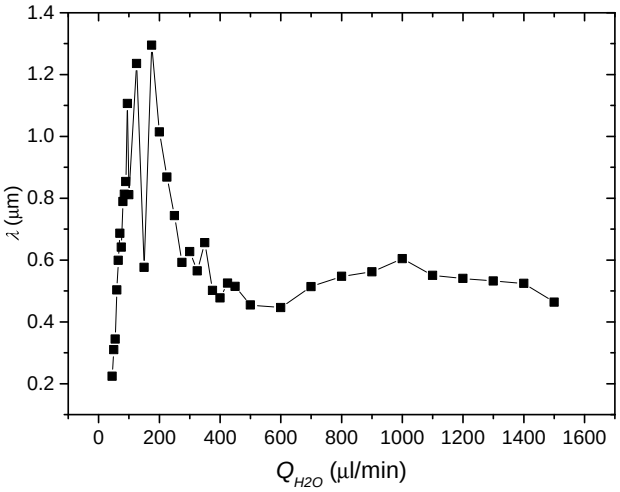

Figure 5.11: Wavelength of the instability as a function of the flow rate of water, for water flowing parallel to glycerol in a 1 mm width channel. The flow rate of glycerol is $Q_{gly} = 12\,\mu\text{L/min}$.

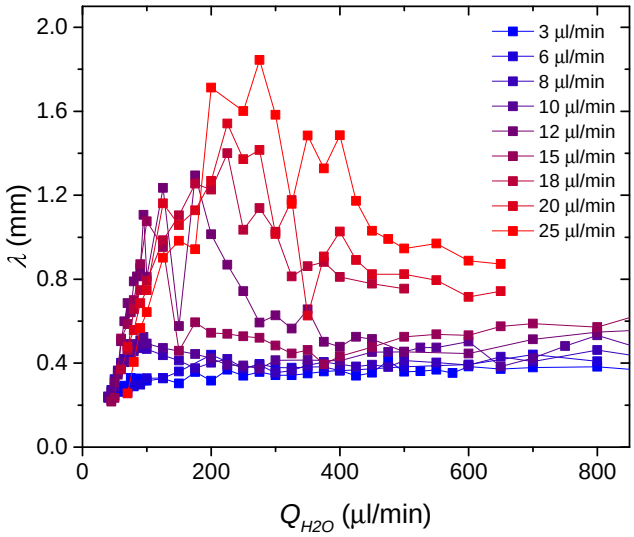

Figure 5.12: Wavelength of the instability as a function of the flow rate of water, for water flowing parallel to glycerol in a 1 mm width channel, at varying glycerol flow rates. For each measurement, Q_{gly} is kept fixed while Q_{H_2O} is varied.

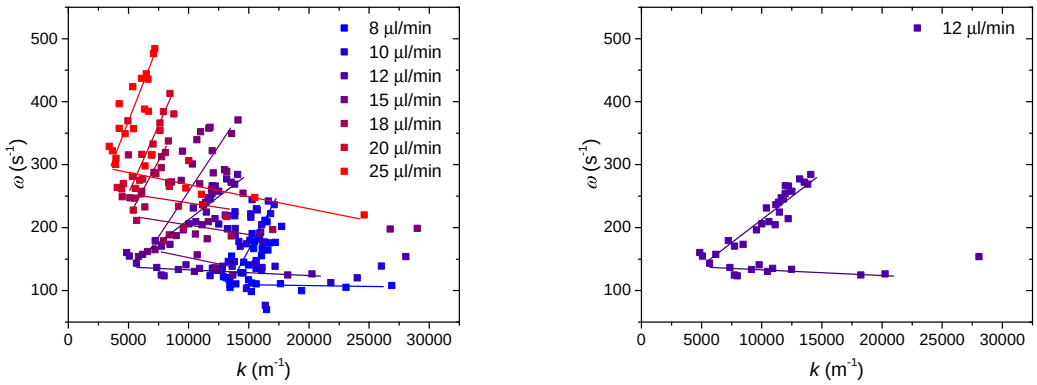

(a) (b)

Figure 5.13: (a) Dispersion relation of the coflow instability between water and glycerol at varying Q_{gly}. Straight lines are a guide for the eye to highlight the two branches of $\omega(k)$. (b) Data for $\omega(k)$ for $Q_{gly} = 12\,\mu\text{L/min}$.

the value of Re with the maximum velocity in the channel. Since water flows always much faster than glycerol, we calculate Re using the water viscosity and density and taking as a characteristic length scale the distance between the interface and the channel wall, which is the width of the equivalent channel in which water flows. Figure 5.14 shows the values of the Reynolds number thus obtained for all the experiments of Fig. 5.12, as a function of Q_{H_2O}. As expected, the Reynolds number is proportional to the imposed water flow rate, and the black line is a linear fit of the experimental data. Notably, Fig. 5.14 rules out the possibility that what is observed are Tollmien-Schlichting waves: the maximum value of Re reached in all the experiments is lower than 300. The origin of the two different regimes must thus be different.

In order to understand the behaviour of the wavelength of the coflow instability it is instructive to plot λ as a function of the position of the interface, expressed by the distance h between the interface and the closest channel wall, on the water side. The results are shown in Fig. 5.15 for various Q_{gly}. One key difference is evident with respect to Fig. 5.12. When the distance h between the interface and the channel wall is chosen as the independent variable, the largest wavelength is observed always at the same value of h, regardless of Q_{gly}. In other words, the change between the two regimes occurs at one specific distance from the wall. This allows interpreting the behaviour of $\lambda(h)$ in the following way. When Q_{gly} is maintained fixed and Q_{H_2O} is reduced, starting from a large value, the wavelength of the instability increases at first, as lower energy modes are excited, up to a value of h where the interplay between the interface and the channel wall becomes significant. Then, at all glycerol flow rates, λ starts decreasing. The regime at low to moderate flow rates can thus be interpreted as due to a confinement effect, where the finite size of the microfluidic channel is important. Indeed, when the interface is close to the wall, the viscous dissipation

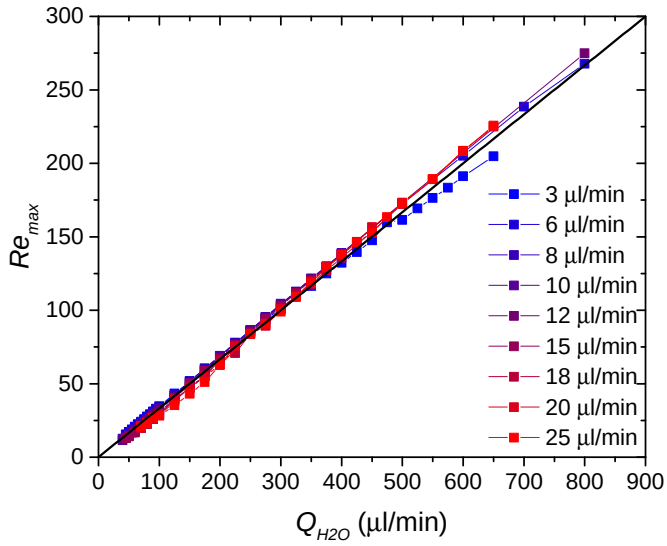

Figure 5.14: Maximum Reynolds number as a function of Q_{H_2O} for all experiments of Fig. 5.12, computed from the velocity profiles of the fluids in the channel. The black line is a linear fit of the experimental data.

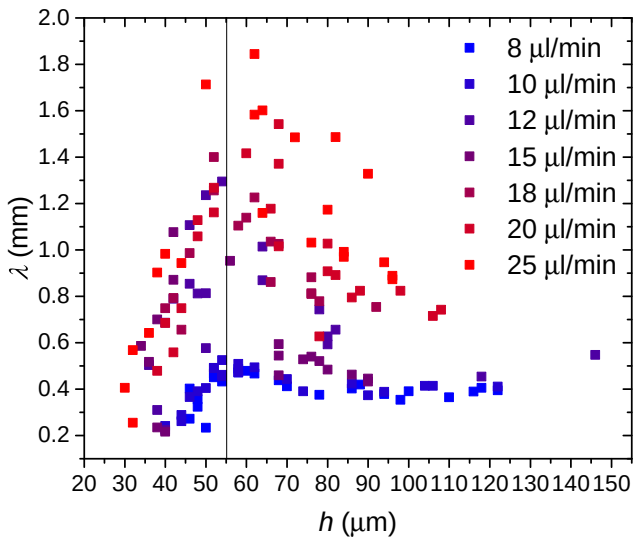

Figure 5.15: Instability wavelength as a function of the distance h between the interface and the closest channel wall (on the water side), at varying glycerol flow rates.

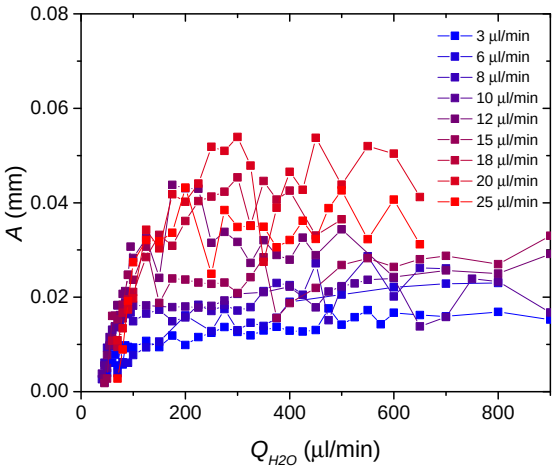

Figure 5.16: Amplitude of the instability as a function of the water flow rate, at varying flow rate of glycerol.

term in the balance for the energy of the disturbance becomes important (Eq. 5.24), with most of the dissipation happening close to the walls [50]. Therefore, it becomes harder to excite high-amplitude waves, and the instability is damped. To further illustrate this point it is instructive to observe the amplitude A of the instability as well, which is reported in Fig. 5.16 as a function of the water flow rate and at varying Q_{gly}. Indeed, at large water flow rates Q_{H_2O} the amplitude is either constant or slowly increases. By contrast, when the flow rate is reduced and the interface gets close to the channel wall the instability amplitude drastically decreases, as viscous dissipation makes it harder to induce large bulges. In particular, the flow rate at which A starts decreasing is the same at which the maximum of the wavelength is found in Fig. 5.12. It is worth discussing one additional consideration on the instability amplitude A. As it can be seen already from Fig. 5.10, immediately after the onset of the instability the waves reach a constant amplitude, which is maintained as they flow downstream, or even decreased due to dissipation. This is a strong hint for the non-linearity of this instability. Indeed, in the linear instability theory the waves should grow exponentially with time as they move, with the growth rate setting the time constant of their increase. On the other hand, large waves can undergo non linear phenomena, and additional terms are required to capture their behaviour. The amplitude of the disturbance is then described by the Landau equation [40]:

$$\frac{d|A|^2}{dt} = 2\sigma|A|^2 - l|A|^4 \,, \tag{5.40}$$

where σ is the growth rate of the perturbation and l is the Landau constant. The first term on the right-hand side is the usual linear perturbation theory, with the amplitude A growing exponentially over time, while the second one introduces the first order of non-linearity. The Landau constant can in general be either positive or negative. The observation that in

our experiments the amplitude does not grow exponentially brings to the conclusion that a formal non-linear description will be needed to properly describe the coflow instability. However, one could still rely on the linear theory to describe the onset of the instability.

We have discussed above from Fig. 5.15 that the decrease of λ at small flow rates can be described as due to a confinement effect, considering the viscous dissipation of the disturbance kinetic energy due to the interaction with the channel wall. One question that we have not yet addressed is: why does the wavelength increase, at a given h, when Q_{gly} is increased? One could expect that higher flow rates, which imply a more energetic base flow, would excite more energetic instability modes with shorter wavelength. However, the situation is more complex, since with increasing Q_{gly} the instability amplitude and phase velocity increase as well. For this reason, it is worth discussing the growth in λ in order to obtain some insight on the instability mechanism. In particular, it is instructive to compare the experimental data with the quantities characterising the base velocity profile calculated according to Sec. 5.1.4, in order to investigate the interplay between the base unperturbed flow and and the disturbance. Before doing so it is necessary to discuss the precision of the numerical computation.

Once the viscosities of the fluids are fixed, the characteristic quantities of the flow profile are the two flow rates, the position of the interface and the pressure gradient in the streamwise direction in the channel. Out of the four, only two are needed to fully compute the flow, as the other two are calculated accordingly (see Sec. 5.1.4). Since experimentally one imposes the flow rates of the fluids, these are the ones that we choose to fix for the computation. The position of the interface is known from the experiments as well, and can be used to cross check the precision of the computation. In detail, the interface position Y can be obtained numerically as the one for which the pressure gradient is homogeneous throughout the whole channel, given the flow rates. Comparing the obtained value of Y with the one which is measured experimentally allows evaluating the precision of the agreement between the experiments and the numerical solution for the base profile: it is worth noting that since the velocity profile is expressed as a Fourier series, higher order terms will always be discarded for computational efficiency, as we typically retain between 5 to 7 harmonics. Furthermore, the experiments are affected by noise and measurement uncertainties stemming from several sources. The viscosity of the fluids has been measured performing steady rate rheology experiments using a stress-controlled AR 2000 rheometer, and temperature was controlled during experiments with a temperature-controlled air flow. On the other hand, the imposed flow rates are affected by the stability of the syringe pumps. Finally, the PDMS with which the microfluidic channels are made is likely to slightly deform under the action of the pressure induced by the flow. Comparing the value of Y obtained from the experiments to the one from the numerical calculation of the base flow allows evaluating the compound noise from all such sources. As an example, Fig. 5.17a reports this comparison for the case of water flowing parallel to glycerol with $Q_{gly} = 15\,\mu\text{L/min}$, as a function of Q_{H_2O}. We evaluate the overall error from all sources of noise in the experiments and numerical solutions to be less than 10%. Similarly, one can evaluate the uncertainty on the computed quantities describing the base velocity profile by using Y as a parameter for the numerical solution (together with one of the two flow rates, such as

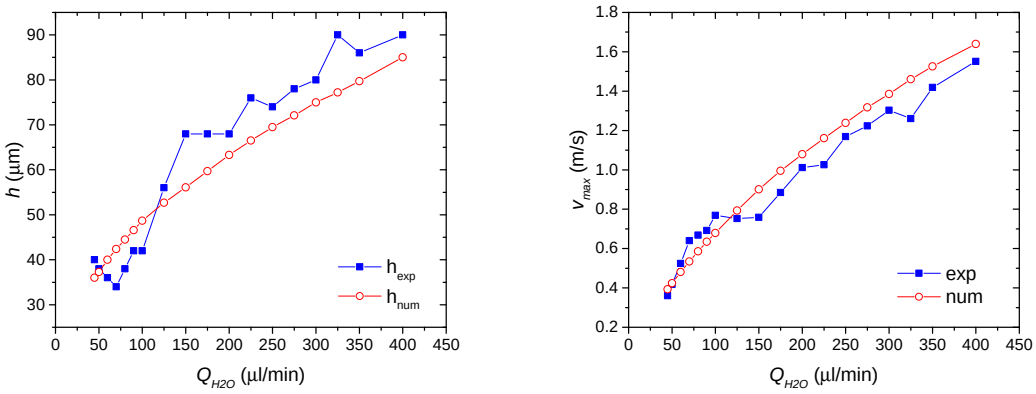

(a) (b)

Figure 5.17: (a) Comparison between the experimental value of the interface position Y (blue filled symbols) and the ones obtained from the numerical solution of the base profile (red open symbols) as a function of Q_{H_2O}, for water flowing parallel to glycerol with $Q_{gly} = 15\,\mu\text{L/min}$. (b) Comparison between the obtained values for the maximum velocity in the channel obtained with the experimental and numerical values of Panel (a), reported in blue filled symbols and red open symbols respectively, as a function of Q_{H_2O}, $Q_{gly} = 15\,\mu\text{L/min}$.

Q_{H_2O}) and by comparing the results obtained using either the experimental value of Y or the one retrieved from the numerical solution, namely the blue filled symbols and the red empty ones in Fig. 5.17a. Using these two values for Y will give slightly different results for the other quantities describing the flow, which thus allow evaluating the uncertainty. Figure 5.17b presents the results of such a comparison for the maximum velocity in the channel as a function of Q_{H_2O}, with $Q_{gly} = 15\,\mu\text{L/min}$. Here again the red empty symbols correspond to the value of Y obtained from the numerical solution, while the blue filled symbols to the experimental value. The uncertainty on the quantities describing the base flow can again be estimated to be less than 10%.

Having assessed the precision of the numerical calculation, the characteristics of the base velocity profile can be used to get insight on the behaviour of the instability. We have already discussed that the viscous dissipation of the disturbance kinetic energy plays a major role in determining the instability wavelength at low Q_{H_2O}, where the interplay between the interface and the channel wall leads to a confinement effect. However, the budget of the disturbance kinetic energy of Eq. 5.24 is strongly affected not only by the dissipation part, but also by the energy production term, $\mathcal{P} = -\langle \hat{u}\hat{v} \rangle U'$. This term represents the energy transfer from the base flow to the disturbance, and U' is the derivative of the base velocity profile in the direction perpendicular to the interface. The shape of the latter is thus of paramount importance in determining the kinetic energy of the instability. Furthermore, while the viscous dissipation takes place mainly close to the walls, the production of kinetic energy happens mainly at the interface between the two fluids.

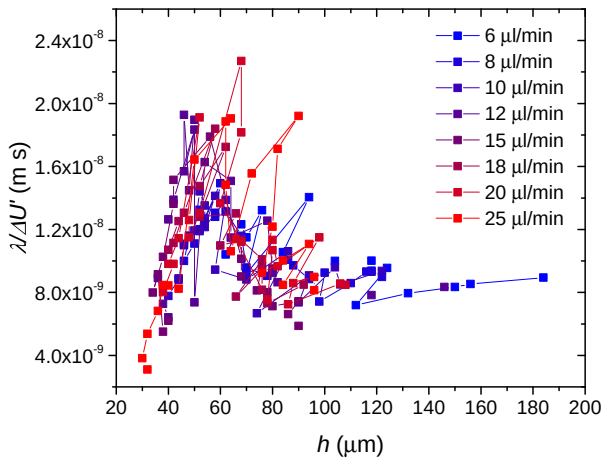

Figure 5.18: Instability wavelength rescaled by the jump $\Delta U'$ in velocity derivative across the interface, as a function of the distance h between the interface and the channel wall.

Indeed, we recall that this is the region where the critical layer of the flow is confined. This can be understood also by considering that at the interface the base velocity profile is steep, with a shear rate jump determined by the viscosity ratio of the two fluids, leading to a large U'.

The derivative of the base velocity profile in the direction perpendicular to the interface seems thus an important parameter affecting the balance of energy production and dissipation for the disturbance. Furthermore, this derivative greatly changes when the flow rates are varied, and its relation with the experimental observations for the disturbance wavelength is consequently interesting. It is worth highlighting that when the interface is considered as infinitely sharp, as in our numerical solutions, U is everywhere continuous, but U' is discontinuous at the interface. Therefore, we consider the difference in the velocity derivative across the interface, $\Delta U'$. This is basically given by the derivative U' on the water side (or, in general, the one of the fastest fluid) reduced by a factor given by the viscosity ratio:

$$\Delta U' = U'_{H_2O}\left(1 - \frac{\eta_{H_2O}}{\eta_{gly}}\right) . \tag{5.41}$$

In particular, $\Delta U'$ increases with the imposed flow rates, and so does the production of kinetic energy of the disturbance. As depicted in Fig. 5.18, all data collapse remarkably well on a single mastercurve, when for each experiment reported in Fig. 5.15 the wavelength is rescaled by the corresponding value of $\Delta U'$. Consequently, when trying to understand the instability of viscosity stratified coflow, one needs not only to consider the viscous energy dissipation, which can induce confinement effects related to the finite channel size, but also the rate of kinetic energy production, strongly related to the shape of the velocity profile of the base flow.

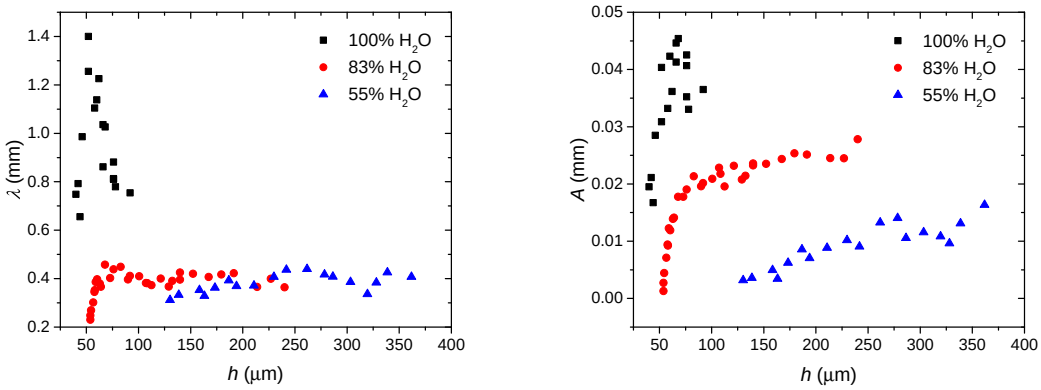

(a) (b)

Figure 5.19: Wavelength (a) and amplitude (b) of the instability as a function of the distance between the interface and the channel wall for different mixtures of water and glycerol flowing parallel to glycerol at $Q_{gly} = 18\,\mu\text{L/min}$.

Both energy production and dissipation depend strongly on the viscosity ratio between the two fluids. As a perspective on further analysis, Fig. 5.19a and 5.19b report the wavelength and amplitude of the instability when one of the two fluids is replaced, so that in all experiments glycerol is in coflow with a mixture of water and glycerol. Black symbols correspond to pure water, while red and blue symbols correspond to mixtures with water mass fraction of 83% and 55%, respectively. Consequently, the viscosity of the mixture increases from 1 mPa s (pure water), to 2.0 mPa s ($\varphi_{H_2O} = 0.83$), to 6.2 mPa s ($\varphi_{H_2O} = 0.55$). The flow rate of glycerol is $Q_{gly} = 18\,\mu\text{L/min}$ for all experiments. Figures 5.19a and 5.19b show that both the wavelength and the amplitude of the instability are strongly reduced when the viscosity ratio η_{mix}/η_{gly} increases, with the maximum in λ becoming barely visible at $\eta_{mix} = 2.0\,\text{mPa s}$ and absent at $\eta_{mix} = 6.2\,\text{mPa s}$. Finally, it is worth noting that the distance h between the interface and the channel wall at which the onset of the instability occurs increases with the viscosity ratio. This is in agreement with the work by Yiantsios and Higgins [52], which found such viscosity stratified flows to be stable up to when the ratio of the distances between the interface and the channel walls on the two sides equals the viscosity ratio of the two fluids.

Figures 5.18, 5.19a and 5.19b give a flavour of the importance of both viscous dissipation and production rate of the disturbance kinetic energy for the stability of viscosity stratified flow. We plan to do further analysis and experiments in the future, to better understand and clarify this topic, which still requires both theoretical and experimental efforts.

Chapter 6

General conclusions and perspectives

6.1 Conclusions

In this thesis we tackled the challenging task of investigating the effective interfacial tension between molecular miscible fluids. In such systems, diffusion constitutes a major impediment when performing experiments. Furthermore, one expects the magnitude of capillary phenomena between miscible fluids to be extremely low, making conventional techniques such as the Langmuir trough or the pendant drop method not suitable [7, 33, 34]. To overcome such difficulties, in this thesis we have first proposed a novel experimental method based on spinning drop tensiometry. This allowed us measuring the EIT at short times, soon after the two fluids are brought into contact. Furthermore, we have explored a second route to probe interfacial stresses in miscible fluids based on the study of the stability of viscosity-stratified coflows.

Conventional SDT experiments rely on the observation of the equilibrium shapes that the drops assume when spinning in a denser background fluid. However, such experiments are not suitable for investigating miscible drops, for which the equilibrium state would be a homogeneous mixture in the SDT capillary. A second possibility which was theoretically discussed in literature [39, 41, 43] consists in rapidly changing the capillary angular velocity and measuring the elongation (or retraction) dynamics of the drop while they attain the new equilibrium state dictated by the final rotational speed. Though presented in literature, little experimental work has been dedicated to this different approach, which was not characterised in depth even in the case of immiscible fluids. Nevertheless, such kind of dynamical SDT measurements can be used for miscible fluids as well. Therefore, we investigated the dynamics of spinning drops when they are subject to a sudden rotation speed jump [11]. Aiming at characterizing miscible fluids, we started from the prototypical case of drops spinning in an immiscible environment, for which the interfacial tension is a well defined thermodynamic quantity. Immiscible drops showed an exponential decay towards their equilibrium shape, with a characteristic time entirely determined by the viscosities of the two fluids, the drop size and the interfacial tension. This exponential relaxation is in

excellent agreement with the one predicted by Stone and Bush [43].

Remarkably, a completely different elongation dynamics is found for miscible drops with a small difference in concentration with respect to the background fluid, such as for a drop of a water-glycerol mixture with 5% water mass fraction spinning in a reservoir of pure glycerol. Indeed, such drops never attain a stationary state, and their elongation dynamics are well captured by a power law, $l(t) \sim t^{0.4}$. Although no theoretical work discussed the elongation dynamics of miscible spinning drops, this evolution is in very good agreement with the one predicted by Lister and Stone [58] for immiscible drops when the interfacial tension is neglected. This result shows that, for small concentration differences between the drop and the background fluids, Korteweg stresses, if they exist, are too small to be measured [11].

Remarkably, spinning drops do not always maintain a simple ellipsoidal shape. For sufficiently low interfacial tension they deform radially developing a "dumbbell" (or dog-bone) shape, consisting in a thin central body connecting two larger heads [45]. We investigated the origin of such shapes, showing that the recirculating motion of the background fluid during rotation induces an unbalanced normal stress on the drop. This stress, being larger at the drop center than at the heads, causes the dog-bone shape. We investigated the time evolution of such shape, demonstrating that it can be used to measure the interfacial tension at the boundary between the drop and the background fluids. By developing a simple model in which we balance the normal stress imposed on the drop surface, the shear stress opposing the deformation and a Laplace-like term containing the surface tension, we exploited the deformation dynamics of miscible drops to measure the EIT between water and glycerol [30]. In particular, we found an EIT of $250 \pm 50\,\mathrm{nN/m}$ for pure water in contact with pure glycerol, a value orders of magnitude lower than the experimental limits of more conventional tensiometry techniques and in excellent agreement with the phase field model proposed in [7]. Therefore, our work proposes a method for measuring extremely low values of interfacial tensions, particularly suited to measure the EIT between miscible fluids [30].

Despite the fact that spinning drop tensiometry was initially conceived for liquid drops, it has been used to measure the properties of viscoelastic solid systems, such as the elasticity of thin capsules [59] and the viscoelastic properties of polymer melts [39, 41]. To complete our work on spinning drop tensiometry, we employed SDT to measure the elastic modulus and interfacial tension of soft elastic beads. Conventional techniques rely on the measurement of the elasto-capillary length, namely the ratio of the interfacial energy per unit area to the elastic modulus. Therefore, these techniques do not allow to decouple the bulk and surface contributions. On the other hand, SDT provides a way to access independently both the shear modulus and the surface energy of soft solids, allowing for the simultaneous measurement of the two quantities as shown in [31].

Finally, we have investigated the stability of viscosity-stratified coflows as a second route to study the EIT and, more generally, miscible interfaces. As we have discussed in Chapter 1, the controversy of literature data on the EIT [27–29] stems from the plethora of experimental techniques that have been used and the different results that they yielded. Consequently, it is not clear under which conditions Korteweg stresses behave alike an equilibrium interfacial tension. These remarks show that it is not sufficient to investigate

this topic by means of SDT only. Even though further experiments and analysis are required to unravel the influence of the interfacial tension on such unstable flows, we presented in Sec. 5.3 the preliminary study of the coflow instability. Two different regimes are observed, as the instability wavelength varies non monotonically with respect to the flow rates. At small to moderate flow rates, the interplay between the interface and the channel walls leads to a confinement effect preventing the excitation of waves of large amplitude and wavelength. At higher values of the flow rate, the amplitude of the disturbance reaches a steady value. We showed that in order to understand the stability of viscosity-stratified flows one needs to take into account both kinetic energy dissipation and energy production, considering the shape of the base flow velocity profile. More work will be carried out to better understand this instability and the possibility of exploiting it as a technique to measure the EIT.

6.2 Perspectives

In this work, we showed that a positive EIT exists at short times when two miscible molecular fluids are brought into contact, before they mix. Nevertheless, one important aspect on the intimate nature of Korteweg stresses still needs to be discussed. In all our experiments, we measured the effect of interfacial stresses by perturbing the interface, either stretching it by means of the forced elongation of a droplet or by means of a growing disturbance of the interface. Following Zeldovich's work [60], one can indeed expect that perturbing the interface in such a way should lead to a net force opposing the deformation, arising from the steepening of the concentration gradient at the interface induced by the deformation itself, *while the interface is stretched*. This is precisely what we measure as an effective interfacial tension. Several questions that remain unanswered: what happens if one does not perturb the interface? Are the tensions characterising deformed and undeformed miscible interfaces the same? If a surface that is already deformed in a non-equilibrium state is left free to evolve, do Korteweg stresses behave as an equilibrium interfacial tension would do, and bring the system back to its original state? These questions are non-trivial, since for miscible fluids even the original undeformed state of the interface is a non-equilibrium state, the equilibrium state being represented by a homogeneous mixture of the fluids. Specifically, Zeldovich demonstrated that when stretching the interface between two miscible fluids one does modify the surface free energy, since the mass conservation of the mixed layer forces the concentration gradient to become steeper as the surface area increases. Therefore, any deformation is opposed by a net force arising from Korteweg stresses, and it is this hypothesis that we verified with our experiments. But in the case of no deformation taking place, is there any net force of this kind?

Put in concrete terms, imagine to have stretched a drop miscible with its environment, as in the case of our spinning drop experiments, and to suddenly stop the rotation. The question that we are asking is: does the drop *retract*, and if so, will the EIT be the same that we measured in [30] under drop elongation? Similar drop retraction experiments were performed for the case of near-critical mixtures [10], for which residual attraction between the molecules of the two phases may still play an important role in determining the retraction, but to the best of our knowledge no experiments showed retraction in the case of molecular miscible liquids, the ones performed by Pojman and coworkers being

hampered by experimental issues [61].

To try to answer this questions it is worth starting from a theoretical discussion. Formally speaking, as we have introduced in Chapter 1, there is a subtle difference between *surface tension* Γ and *surface free energy* F_s, which was originally investigated by Shuttleworth in 1950 for the case of solids [4]. Following his work, surface energy corresponds to the work necessary to form a unit surface by a process of division, such as the cleavage of a solid. On the other hand, surface tension has a mechanical definition, in the sense that it is the tangential stress applied on the surface, or the force per unit length, when one wants to deform the surface by stretching it. The relation between the two is given by [4]:

$$\Gamma = F_s + A\left(\frac{\partial F_s}{\partial A}\right) . \tag{6.1}$$

As we anticipated in Chapter 1, the difference between surface energy F_s and tension Γ can be understood considering the case of crystals. On the one hand, when a surface is stretched, the distance between the atoms changes (at least at low temperatures, when atom motility can be neglected). On the other hand, this does not happen when a new interface is created in a state of mechanical equilibrium. Therefore, the surface energy depends on the deformation state of the crystal, and thus it differs from the surface tension. The same holds for a viscoelastic system subject to deformations occurring much faster than the time needed by internal stresses to relax: surface energy and tension become equal only after a complete rearrangement of the molecules at the interface has occurred. By contrast, at the interface between two simple immiscible viscous liquids the two quantities coincide [62], and this is the reason for the confusion on the subject. The formal difference between surface tension and energy becomes important for all non-equilibrium surfaces, such as the case of the interface between miscible fluids. In this work, we have proven that when such a miscible interface is deformed Korteweg stresses act as an effective interfacial tension, opposing the deformation. Nevertheless, in order to better understand the nature of Korteweg stresses, it is worth considering the EIT in the light of the dependence of the interfacial free energy F_s on the deformation, following Zeldovich's approach [60].

Let us consider a flat interface in the xy plane between two fully miscible liquids, such as water and glycerol. After a time t_0 diffusion will have brought the mixed layer to a thickness δ in the z direction, so that the mass of mixture is $M = \rho A\delta$, where A is the surface area and ρ the average density of the mixture. We denote by φ the concentration of one of the two fluids, which varies across the interface (φ_1 and φ_2 are the concentrations in the bulk of the two fluids, see Fig. 6.1). In order to compute the surface free energy F_s, one has to integrate across the mixed layer the free energy density difference f_s. The latter is defined as the difference between the actual free energy per unit volume of the system and that which the system would have if the properties of the two phases were continuous throughout the interface [6]:

$$f_s = \Delta f(\varphi) + \frac{k(\varphi)}{2}(\nabla\varphi)^2 , \tag{6.2}$$

where $k(\varphi)$ is the Korteweg parameter, and $\Delta f(\varphi)$ is the free energy density difference between a mixture of two fluids with local concentration φ and a system in which the two

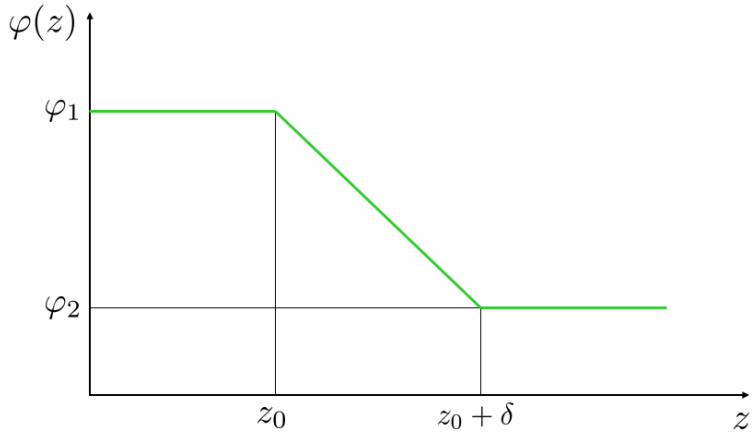

Figure 6.1: Spatial dependence of the concentration profile across the interface. The concentration profile is approximated as linear across the interfacial layer, which spans from z_0 to $z_0 + \delta$.

fluids are separate and no interface is present. In order to obtain the free energy per unit area associated with the interface, Eq. 6.2 has to be integrated across the mixed layer. Approximating for simplicity the concentration profile as linear across the interface, as depicted in Fig. 6.1, one has:

$$F_s = \int_{z_0}^{z_0+\delta} \left[\Delta f(\varphi) + \frac{k(\varphi)(\Delta\varphi)^2}{2\delta^2} \right] dz \,, \tag{6.3}$$

where $\Delta\varphi = \varphi_1 - \varphi_2$. Equation 6.3 corresponds to the first term in Eq. 6.1, and for immiscible fluids it would be simply equal to the interfacial tension.

It is worth noting that for the case of fully miscible liquids the first integrand in Eq. 6.3 is negative: the fluids mix, and the equilibrium state is a homogeneous mixture of the liquids, which means that a configuration with a mixed layer is less energetic than the one with two unmixed fluids and, as a consequence, $\Delta f(\varphi) < 0$. In particular, assuming the mixture to be symmetric, one can write $\Delta f(\varphi) = C\varphi(1-\varphi)$, with C a negative constant (see Fig. 6.2). Equation 6.3 can still in principle take both negative and positive sign depending on the steepness of the concentration gradient and on the relative magnitude of the Korteweg parameter $k(\varphi)$ and of $\Delta f(\varphi)$. However, considering that very steep gradients are smeared out by diffusion over very short timescales, one can expect Eq. 6.3 to have a negative sign in almost all practical situation for miscible fluids, and the square gradient term to be a second order correction to $\Delta f(\varphi)$ (this may not be true for different cases, such as critical mixtures or colloidal suspensions, where sharp interfaces can be maintained for longer times due to a slower diffusion). Therefore, for simple miscible liquids considering the interfacial free energy alone would not lead to a measurable interfacial tension in most practical cases, and would lead the fluids to simply diffuse over time in absence of any capillary effect.

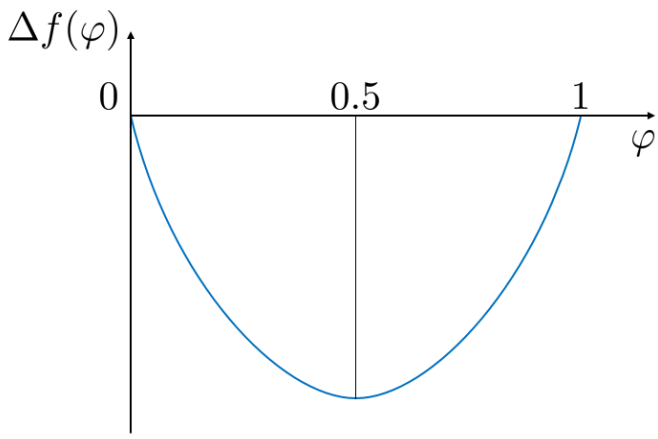

Figure 6.2: Concentration dependence of the first term in the interfacial free energy, $\Delta f(\varphi)$. Assuming the mixture to be symmetric, $\Delta f(\varphi)$ has a minimum at $\varphi = 0.5$, and can be written as $\Delta f(\varphi) = C\varphi(1-\varphi)$, with C negative constant.

Nevertheless, a careful inspection of the terms in Eq. 6.3 unveils a dependence of the surface free energy on the surface area, which can become important when the interface is stretched and explain the presence of capillary phenomena in miscible interfaces. In order to understand this it is necessary to consider what happens in a system in such circumstances. If the interface stretching takes place so fast that over the course of the deformation one can neglect diffusion, the system can be considered as "frozen" with respect to the latter, and the mass M and the volume of the mixed layer will be conserved while the interface is stretched. This means that any deformation of the interface fast enough to neglect diffusion will imply also a change in the interface thickness δ and consequently in the square gradient term in the surface free energy. In particular, enlarging the interface will induce the concentration gradient to become steeper, as depicted in Fig. 6.3. Therefore, it is worth considering the surface dependence of Eq. 6.3 with care.

We compute the surface dependence of Eq. 6.3 assuming the mixture to be symmetric (so that $\Delta f(\varphi)$ has the shape represented in Fig. 6.2), and approximating the concentration profile as linear across the interface, as depicted in Fig. 6.1. Since over the interface thickness δ we have $d\varphi = -\frac{\Delta\varphi}{\delta}dz$, we change integration variable and integrate over $d\varphi$. The integrand $\Delta f(\varphi)$ in Eq. 6.3 yields a contribution:

$$F_{\Delta f} = \int_{z_0}^{z_0+\delta} \Delta f(\varphi)dz = \int_{\varphi_2}^{\varphi_1} \frac{\delta}{\Delta\varphi} C\varphi(1-\varphi)d\varphi = \frac{\delta C}{\Delta\varphi}\left[\frac{\varphi^2}{2} - \frac{\varphi^3}{3}\right]_{\varphi_2}^{\varphi_1} = C^*\delta\,. \tag{6.4}$$

Here C^* is a constant which depends on C and on the values of φ_1 and φ_2, which are determined by the concentrations in the bulk of the fluids and do not change over the course of the deformation. C^* has the same sign as C, and for completely miscible fluids (for which C is negative) Eq. 6.4 yields the expected results that the thicker is the interface layer, the lower is the free energy of the system.

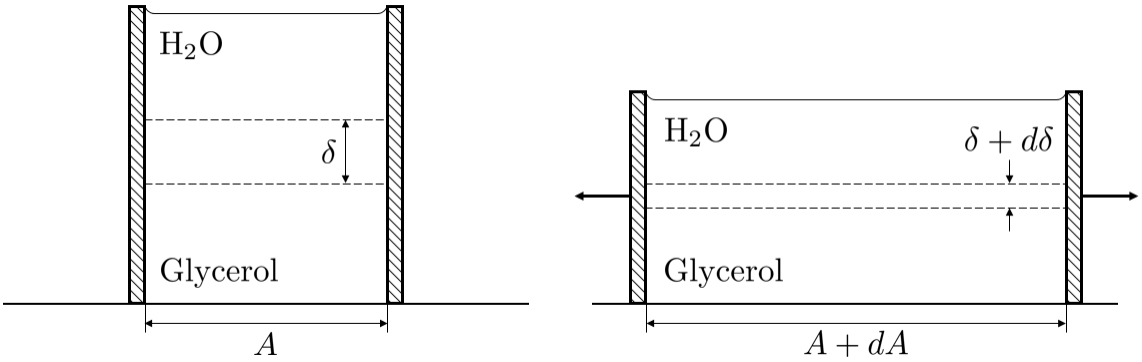

Figure 6.3: Ideal representation of a stretching of the interfacial mixed layer between two fully miscible liquids, such as water and glycerol, when diffusion can be neglected. A change in surface area induces a variation in thickness due to the mass conservation of the mixed layer.

Then, for the second integrand in Eq. 6.3, neglecting the dependence of k on φ [10,63], one finds that the presence of Korteweg stresses yields a contribution F_K:

$$F_K = \frac{k(\Delta\varphi)^2}{2\delta} \,. \tag{6.5}$$

Equations 6.4 and 6.5 together constitute the surface free energy term in Eq. 6.1. Considering their surface dependence is then necessary in order to compute the interfacial tension from Eq. 6.1.

The mass conservation in the mixed layer imposes $M = \rho\delta A = const$. Considering the average density ρ in the mixed layer not to change with the deformation, Eq. 6.4 and 6.5 can be rewritten as:

$$F_{\Delta f} = C^* \frac{M}{\rho A} \,, \tag{6.6}$$

$$F_K = \frac{k(\Delta\varphi)^2}{2M} \rho A \,, \tag{6.7}$$

respectively. At time t_0, let the interface be stretched so that its surface becomes $A + dA$. Both Eq. 6.6 and 6.7 depend on the surface area and need to be accounted for when computing the interfacial tension Γ. In particular, introducing all the contributions to the interfacial free energy in Eq. 6.1, one finds for the effective interfacial tension between miscible fluids:

$$\Gamma_e = C^*\delta + \frac{k(\Delta\varphi)^2}{2\delta} - C^* \frac{M}{\rho A} + \frac{k(\Delta\varphi)^2}{2M} \rho A = \frac{k(\Delta\varphi)^2}{\delta} \,. \tag{6.8}$$

Interestingly, this is the same result that one would find assuming the surface free energy not to depend on the area and differentiating the total free energy of the system over the interface area assuming local equilibrium [6, 10]. Nevertheless, in order to obtain Eq. 6.8

we did not make any assumption of quasi-equilibrium and took into account the surface dependence of the free energy, which makes the derivation described here more general.

Equation 6.8 is particularly interesting in the light of Eq. 6.1: in order to compute the effective interfacial tension Γ_e arising from Korteweg stresses is in fact necessary to consider a term $\frac{\partial F_s}{\partial A}$. This means that an EIT is fundamentally different from an equilibrium interfacial tension Γ, and contrasting results can be obtained when the tension is measured in presence or in absence of a deformation dA. Even if the surface free energy for simple miscible fluids will be almost always negative, a positive contribution can arise from the term $\frac{\partial F_s}{\partial A}$ causing a net force opposing the deformation. The fact that one would find different results when measuring an EIT in different ways is an expression of the out-of-equilibrium character of Korteweg stresses. When considering the intimate nature of the EIT, it is not sufficient to consider the energy associated to the interfacial layer: the dependence of the latter on the surface area is necessary in order to understand its effect as a capillary phenomenon.

According to the above arguments, a drop retraction experiment as the one described above would yield the same EIT measured in [30] while the drop was stretched since, during the retraction, the surface area and the interfacial layer thickness δ would change. It is worth noting that this result was obtained neglecting diffusion, whose interplay with the drop retraction may still be important in a real experiment. Nevertheless, this constitutes a possible theoretical answer to the question at the beginning of the present section: would a drop miscible with its environment retract, in absence of an external forcing? To verify experimentally this hypothesis is a challenging task. In the configuration that we proposed above of stretching a miscible drop in an SDT experiment and then suddenly stopping the rotation, a fundamental issue would hamper the realization of the experiment. Indeed, if we were to perform this experiment on Earth, buoyancy would quickly push the drop out of the axis of the capillary of the spinning drop tensiometer once the rotation is stopped, preventing the observation of any retraction.

For this reason, we recently proposed to perform this experiment in microgravity conditions on board of a parabolic flight. Among the different ways to perform microgravity experiments (other possibilities are free fall experiments on sounding rockets, and experiments performed onboard the International Space Station), parabolic flights are the most accessible and simple, allowing the experimenters to directly manipulate the setup during flight, and thus they offer a unique possibility for an experimental environment that would be impossible to replicate on Earth. During a parabolic flight, the pilot performs a series of parabolic maneuvers, resulting in a succession of hypergravity and microgravity phases. Figure 6.4 represents the various phases of a parabolic flight, as well as a scheme of the experimental protocol that we propose. The capillary will be initially spun, forcing the drop to elongate. In this phase, the centripetal acceleration is much larger than the gravitational one. Once the zero-g phase of the parabola is reached, the rotation will be switched off ($\omega = 0$): if the EIT behaves alike an equilibrium interfacial tension, the drop will retract. The microgravity phase lasts about 22 s, which allows for a quantitative measure of the EIT from the rate of retraction, following the results in [11]. Then, the capillary will be either replaced with a new one or set in rotation again, in order to exploit a new parabola

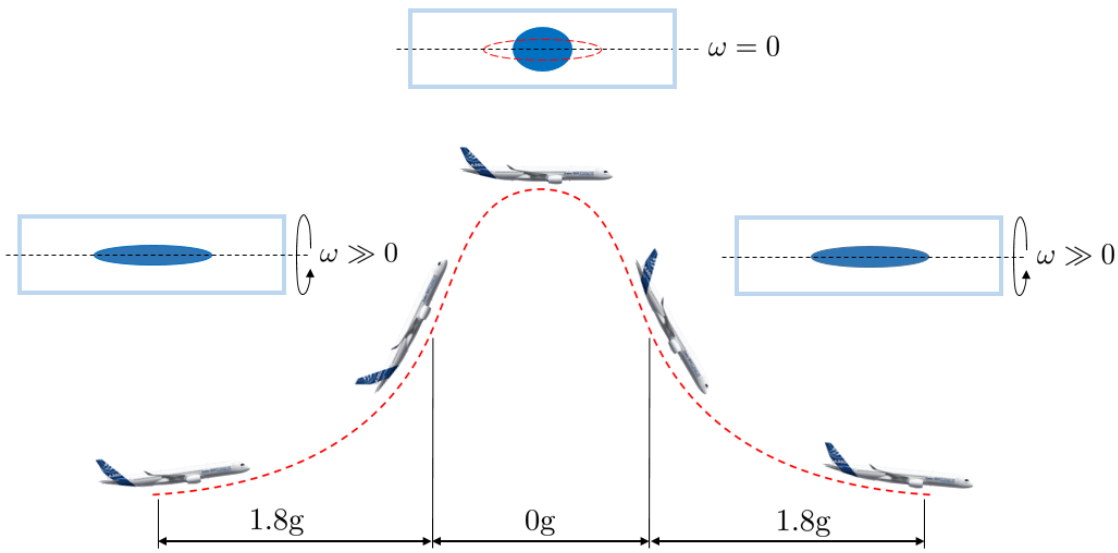

Figure 6.4: Scheme of the parabolic flight maneuver. The capillary will be spun during the hypergravity phase, and the rotation will be arrested during the microgravity phase to measure an eventual drop retraction.

at a different elongation state (and time elapsed since the injection of the drop, hence a different interfacial concentration gradient due to diffusion). Over the many parabolas of a flight campaign, we will test several samples, notably the water-glycerol mixtures and triethylene glycol investigated in [11,30], tuning the value of the expected EIT by changing the water content of the mixtures. Another important experimental parameter is the time elapsed between the injection of the drop and the stop of the rotation, which determines the thickness of the interfacial mixed layer due to diffusion.

These experiments were funded and accepted for a CNES (Centre National d'études spatiales) parabolic flight campaign. They will be performed on board of an Airbus A310 adapted for microgravity experiments in the Bordeaux-Mérignac airport between September 28th and October 9th 2020. Their results will allow to shed light on the intimate nature of Korteweg stresses, highlighting whether or not they behave as an equilibrium interfacial tension.

Bibliography

[1] D. J. Korteweg. Sur la forme que prennent les équations du mouvement des fluides si l'on tient compte des forces capillaires causées par des variations de densité considérables mais continues et sur la théorie de la capillarité dans l'hypothèse d'une variation continue de la densité. *Archives Néerlandaises*, 2(6):1–27, 1901.

[2] C. D. Han. *Multiphase flow in polymer processing.* Elsevier, 1981.

[3] G. Morra and D. A. Yuen. Role of Korteweg stresses in geodynamics. *Geophysical Research Letters*, 35(7), 2008.

[4] R. Shuttleworth. The surface tension of solids. *Proceedings of the Physical Society, Section A*, 63:444–457, 1950.

[5] N. Cabeo. *Philosophia magnetica*, volume II. 1629.

[6] J. W. Cahn and J. E. Hilliard. Free energy of a nonuniform system. I. Interfacial free energy. *The Journal of Chemical Physics*, 28(2):11, 1958.

[7] D. Truzzolillo, S. Mora, C. Dupas, and L. Cipelletti. Nonequilibrium interfacial tension in simple and complex fluids. *Physical Review X*, 6:041057, 2016.

[8] L. K. Antanovskii. Microscale theory of surface tension. *Physical Review E*, 54(6):6285–6290, 1996.

[9] C.-Y. Chen and E. Meiburg. Miscible displacements in capillary tubes: influence of Korteweg stresses and divergence effects. *Physics of Fluids*, 14(7):2052, 2002.

[10] J. A. Pojman, C. Whitmore, M. L. Turco Liveri, R. Lombardo, J. Marszalek, R. Parker and B. Zoltowski. Evidence for the existence of an effective interfacial tension between miscible fluids: isobutyric acid-water and 1-butanol-water in a spinning-drop tensiometer. *Langmuir*, 22(6):2569–2577, 2006.

[11] A. Carbonaro, L. Cipelletti and D. Truzzolillo. Spinning drop dynamics in miscible and immiscible environments. *Langmuir*, 35(35):11330–11339, 2019.

[12] A. Vorobev, T. Zagvozkin and T. Lyubimova. Shapes of a rising miscible droplet. *Physics of Fluids*, 32(1):012112, 2020.

[13] P. Cicuta, A. Vailati and M. Giglio. Capillary-to-bulk crossover of nonequilibrium fluctuations in the free diffusion of a near-critical binary liquid mixture. *Applied Optics*, 40(24):4140, 2001.

[14] S. May and J. Maher. Capillary-wave relaxation for a meniscus between miscible liquids. *Physical Review Letters*, 67(15):2013–2016, 1991.

[15] V. Shevtsova, Y. A. Gaponenko, V. Yasnou, A. Mialdun and A. Nepomnyashchy. Two-scale wave patterns on a periodically excited miscible liquid-liquid interface. *Journal of Fluid Mechanics*, 795:409–422, 2016.

[16] D. Truzzolillo and L. Cipelletti. Off-equilibrium surface tension in miscible fluids. *Soft Matter*, 13(1):13–21, 2017.

[17] B. Zoltowski, Y. Chekanov, J. Masere, J. A. Pojman and V. Volpert. Evidence for the existence of an effective interfacial tension between miscible fluids. 2. Dodecyl acrylate-poly(dodecyl acrylate) in a spinning drop tensiometer. *Langmuir*, 23(10):5522–5531, 2007.

[18] G. Viner, T. La Monica, R. Lombardo and J. A. Pojman. Effect of pseudo-gravitational acceleration on the dissolution rate of miscible drops. *Chaos: An Interdisciplinary Journal of Nonlinear Science*, 27(10):104603, 2017.

[19] S. Bamberger, G. V. F. Seaman, K. A. Sharp and D. E. Brooks. The effects of salts on the interfacial tension of aqueous dextran poly(ethylene glycol) phase systems. *Journal of Colloid and Interface Science*, 99(1):194–200, 1984.

[20] Y. Liu, R. Lipowsky and R. Dimova. Concentration dependence of the interfacial tension for aqueous two-phase polymer solutions of dextran and polyethylene glycol. *Langmuir*, 28(8):3831–3839, 2012.

[21] D. Truzzolillo and L. Cipelletti. Hydrodynamic instabilities in miscible fluids. *Journal of Physics: Condensed Matter*, 30(3):033001, 2018.

[22] Lord Rayleigh. On the instability of jets. *Proceedings of the London Mathematical Society*, 10:4–13, 1878.

[23] S. Tomotika. On the instability of a cylindrical thread of a viscous liquid surrounded by another viscous fluid. *Proceedings of the Royal Society of London. Series A - Mathematical and Physical Sciences*, 150(870):322–337, 1935.

[24] S. V. Diwakar, F. Zoueshtiagh, S. Amiroudine and R. Narayanan. The Faraday instability in miscible fluid systems. *Physics of Fluids*, 27(8):084111, 2015.

[25] F. Zoueshtiagh, S. Amiroudine and R. Narayanan. Experimental and numerical study of miscible Faraday instability. *Journal of Fluid Mechanics*, 628:43–55, 2009.

[26] L. Paterson. Fingering with miscible fluids in a Hele Shaw cell. *Physics of Fluids*, 28(1):26–30, 1985.

[27] I. Bischofberger, R. Ramachandran and S. R. Nagel. Fingering versus stability in the limit of zero interfacial tension. *Nature Communications*, 5(1), 2014.

[28] P. Petitjeans. Une tension de surface pour le fluides miscibles. *Comptes rendus de l'Académie des Sciences*, 673–679, 1996.

[29] M. Legendre, P. Petitjeans, and P. Kurowski. Instabilités à l'interface entre fluides miscibles par forçage oscillant horizontal. *Comptes Rendus Mécanique*, 331(9):617–622, 2003.

[30] A. Carbonaro, L. Cipelletti and D. Truzzolillo. Ultralow effective interfacial tension between miscible molecular fluids. *Physical Review Fluids*, 5:074001, 2020.

[31] A. Carbonaro, K.-N. Chagua-Encarnacion, C.-A. Charles, T. Phou, C. Ligoure, S. Mora and D. Truzzolillo. Spinning elastic beads: a route for simultaneous measurements of the shear modulus and the interfacial energy of soft materials. *Soft Matter*, DOI:10.1039/d0sm01024c, 2020.

[32] E. Ramé. The interpretation of dynamic contact angles measured by the Wilhelmy plate method. *Journal of Colloid and Interface Science*, 185:245–251, 1997.

[33] B. S. Murray and P. V. Nelson. A novel Langmuir trough for equilibrium and dynamic measurements on air-water and oil-water monolayers. *Langmuir*, 12(25):5973–5976, 1996.

[34] J. D. Berry, M. J. Neeson, R. R. Dagastine, D. Y. C. Chan and R. F. Tabor. Measurement of surface and interfacial tension using pendant drop tensiometry. *Journal of Colloid and Interface Science*, 454:226–237, 2015.

[35] B. Widom. Line tension and the shape of a sessile drop. *The Journal of Physical Chemistry*, 99(9):2803–2806, 1995.

[36] B. Vonnegut. Rotating bubble method for the determination of surface and interfacial tensions. *Review of Scientific Instruments*, 13(1):6–9, 1942.

[37] I. Y. Z. Zia H. M. Princen, and S. G. Mason. Measurement of interfacial tension from the shape of a rotating drop. *Journal of Colloid and Interface Science*, 23(1):99–107, 1967.

[38] S. Torza. The rotating-bubble apparatus. *Review of Scientific Instruments*, 46(6):778–783, 1975.

[39] D. D. Joseph, M. S. Arney, G. Gillberg, H. H. Hu, D. Hultman, C. Verdier and T. M. Vinagre. A spinning drop tensioextensometer. *Journal of Rheology*, 36(4), 1992.

[40] L. D. Landau and E. M. Lifshitz. *Course of theoretical physics, Volume 6 - Fluid Mechanics*. Pergamon Press, 1987.

[41] H. T. Patterson, K. H. Hu and T. H. Grindstaff. Measurement of interfacial and surface tensions in polymer systems. *Journal of Polymer Science Part C: Polymer Symposia*, 34(1):31–43, 2007.

[42] H. H. Hu and D. D. Joseph. Evolution of a liquid drop in a spinning drop tensiometer. *Journal of Colloid and Interface Science*, 162:331–339, 1994.

[43] H. A. Stone and J. W. M. Bush. Time-dependent drop deformation in rotating viscous fluid. *Quarterly of Applied Mathematics*, 54(3):551–556, 1996.

[44] P. K. Currie and J. Van Nieuwkoop. Buoyancy effects in the spinning-drop interfacial tensiometer. *Journal of Colloid and Interface Science*, 87(2):301–316, 1982.

[45] C. D. Manning and L. E. Scriven. On interfacial tension measurement with a spinning drop in gyrostatic equilibrium. *Review of Scientific Instruments*, 48(12):1699–1705, 1977.

[46] A. Carbonaro. miscibleFluidsEIT: v1.0.0. https://doi.org/10.5281/zenodo.4001559, 2020.

[47] A. Carbonaro, L. Cipelletti and D. Truzzolillo. Supplemental material to Ultralow effective interfacial tension between miscible molecular fluids. *Physical Review Fluids*, 5:074001, 2020.

[48] A. Quarteroni. *Numerical models for differential problems*, volume 16 of *MS&A*. Springer International Publishing, 2017.

[49] W. Heisenberg. Über stabilität und turbulenz von flüssigkeitsströmen. *Annalen der Physik*, 74(15), 1924.

[50] R. Govindarajan and K. C. Sahu. Instabilities in viscosity-stratified flow. *Annual Review of Fluid Mechanics*, 46(1):331–353, 2014.

[51] P. G. Drazin and W. H. Reid. *Hydrodynamic stability.* Cambridge University Press, 2004.

[52] S. G. Yiantsios and B. G. Higgins. Linear stability of plane Poiseuille flow of two superposed fluids. *Physics of Fluids*, 31(11):3225, 1988.

[53] K. C. Sahu and R. Govindarajan. Linear stability analysis and direct numerical simulation of two layer channel flow. *Journal of Fluid Mechanics*, 798:889–909, 2016.

[54] H. B. Squire. On the stability of three-dimensional disturbances of viscous flow between parallel walls. *Proceedings of the Royal Society A: Mathematical, Physical and Engineering Sciences*, 142(621-8):129–155, 1933.

[55] C.-S. Yih. Instability due to viscosity stratification. *Journal of Fluid Mechanics*, 27(2):337–352, 1967.

[56] P. J. Stiles and D. F. Fletcher. Hydrodynamic control of the interface between two liquids flowing through a horizontal or vertical microchannel. *Lab on a Chip*, 4(2):121, 2004.

[57] J. Friend and L. Yeo. Fabrication of microfluidic devices using polydimethylsiloxane. *Biomicrofluidics*, 4(2):026502, 2010.

[58] J. R. Lister and H. A. Stone. Time-dependent viscous deformation of a drop in a rapidly rotating denser fluid. *Journal of Fluid Mechanics*, 317:275–299, 1996.

[59] G. Pieper, H. Rehage and D. Barthès-Biesel. Deformation of a capsule in a spinning drop apparatus. *Journal of Colloid and Interface Science*, 202(2):293–300, 1998.

[60] Y. B. Zeldovich. About surface tension of a boundary between two mutually soluble liquids. *Zhurnal fizicheskoi Khimii (in Russian)*, 23(8):931–935, 1949.

[61] J. A. Pojman, N. Bessonov, V. Volpert and M. S. Paley. Miscible Fluids in Microgravity (MFMG): A zero-upmass investigation on the International Space Station. *Microgravity - Science and Technology*, 19(1):33–41, 2007.

[62] A. Dupré. *Théorie méchanique de la chaleur*. Gauthier-Villars, Paris, 1869.

[63] D. Truzzolillo, S. Mora, C. Dupas and L. Cipelletti. Off-equilibrium surface tension in colloidal suspensions. *Physical Review Letters*, 112(12), 2014.

Résumé de la thèse

La tension interfaciale entre liquides immiscibles est une quantité thermodynamique bien définie, importante pour une grande varieté de phénomènes, des boules de savon jusqu'à la récupération du pétrole et la vie biologique.

En revanche, l'existence même d'une tension d'interface entre liquides miscibles n'est pas encore établie. En 1901, le physicien et mathématicien néerlandais Diederik Korteweg proposa que les gradients en concentration ou en densité hors équilibre qui peuvent exister à l'interface entre deux liquides miscibles avant qu'ils soient complètement melangés, peuvent agir comme une tension interfaciale effective (EIT, *effective interfacial tension*). L'existence même de cette tension effective est actuellement débattue, et plusieurs travaux théoriques et expérimentaux ont étés dédies à ce sujet [7–15]. Dans cette thèse nous proposons un travail expérimental visant à comprendre et mesurer l'EIT entre liquides moléculaires miscibles.

Dans les années, plusieurs techniques ont été développées pour mesurer une tension d'interface, comme la plaque de Wilhelmy [32], la cuve de Langmuir [33] ou l'analyse de la forme des gouttes pendants [34]. Toutes ces techniques diffèrent par leur sensibilité, par la présence ou l'absence d'un champ externe imposé, et leur pertinence pour des systèmes spécifiques, tels que les interfaces liquide-vapeur, liquide-solide ou liquide-liquide. En particulier pour l'étude de ces dernieres, une technique spécifique qui permet de mesurer des valeurs très basses de Γ (10^{-3} - 10^{-2} mN/m [19, 20]) grâce à un contrôle fin du forçage imposé est la tensiométrie à goutte tournante (SDT, *spinning drop tensiometry*).

Les expériences conventionnelles de SDT reposent sur l'observation des formes d'équilibre prises par des gouttes tournantes dans un fluide porteur plus dense. Cependant, ces expériences ne sont pas adaptées pour étudier des gouttes miscibles, pour lesquelles l'état d'équilibre serait un mélange homogène dans le capillaire du SDT. Une deuxième possibilité qui a été discutée théoriquement dans la littérature [39, 41, 43] consiste à changer rapidement la vitesse angulaire du capillaire et à mesurer l'allongement (ou la rétraction) dynamique des gouttes pendant qu'elles atteignent le nouvel état d'équilibre dicté par la vitesse de rotation finale. Peu de travaux expérimentaux ont été consacrés à cette approche différente, qui n'a pas été caractérisée en profondeur, même dans le cas des fluides non miscibles. Néanmoins, ce type de mesures dynamiques de SDT peut également être utilisé pour les fluides miscibles. Nous avons donc étudié la dynamique d'allongement des gouttes lorsqu'elles sont soumises à un saut brusque de vitesse de rotation [11]. Afin de caractériser les fluides miscibles, nous sommes partis du cas prototypique de la rotation des gouttes dans un environnement non miscible, pour lequel la tension interfaciale est une

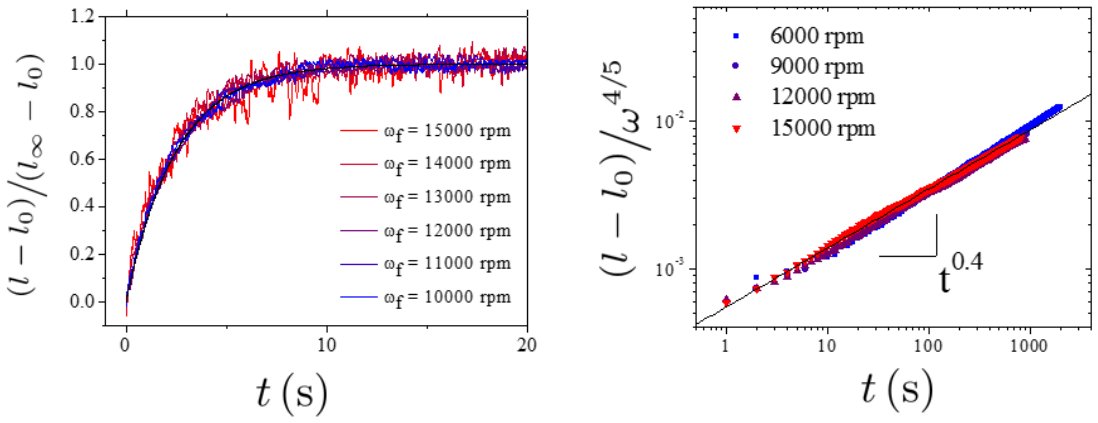

(a) (b)

Figure 6.5: (a) Relaxation exponentielle de gouttes tournantes dans un liquid non miscible après un saut de vitesse de rotation. (b) Dynamique d'allongement en loi de puissance de gouttes miscibles ayant une faible différence en concentration par rapport au fluide porteur, notamment une goutte d'un mélange eau-glycérol avec une fraction de masse d'eau de 5% tournant dans un réservoir de glycérol pur.

quantité thermodynamique bien définie. Les gouttes immiscibles ont montré une relaxation exponentielle vers leur forme d'équilibre, avec un temps caractéristique entièrement déterminé par les viscosités des deux fluides, la taille de la goutte et la tension interfaciale. Cette relaxation exponentielle, reporté dans la Fig. 6.5a, est en excellent accord avec celle prédite par Stone et Bush [43].

D'autre part, on constate une dynamique d'allongement complétement différente pour les gouttes miscibles ayant une faible différence en concentration par rapport au fluide porteur, comme pour une goutte d'un mélange eau-glycérol avec une fraction de masse d'eau de 5% tournant dans un réservoir de glycérol pur. Des telles gouttes n'atteignent jamais un état stationnaire, et leur dynamique d'allongement est bien reproduite par une loi de puissance, $l(t) \sim t^{0.4}$ (Fig. 6.5b). Même si aucun travail théorique n'a discuté la dynamique d'allongement des gouttes tournantes miscibles, cette évolution est en très bon accord avec celle prédite par Lister et Stone [58] pour des gouttes immiscibles lorsque la tension interfaciale est négligée. Ce résultat montre que, pour de faibles différences de concentration entre la goutte et le fluide porteur, aucun stress de Korteweg ne peut être mesuré [11].

De façon remarquable, les gouttes tournantes ne conservent pas toujours une forme ellipsoïdale simple. Pour une tension interfaciale suffisamment faible, elles se déforment radialement en développant une forme *"dumbbell"* (ou à os de chien), consistant en un corps central mince reliant deux têtes plus grandes [45]. La Figure 6.6a fournit des exemples de gouttes en forme *"dumbbell"*. Les gouttes dans les panneaux A et C sont composées d'un

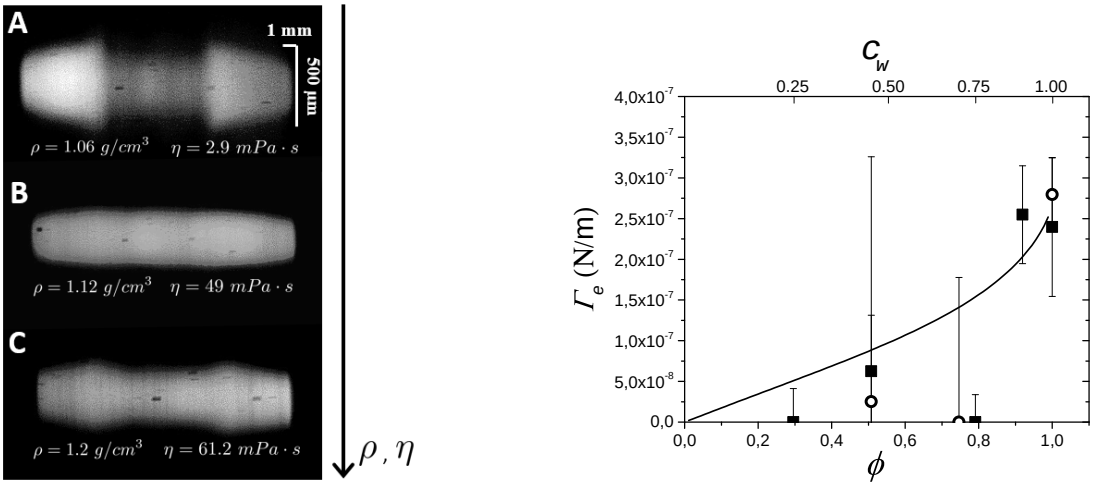

(a) (b)

Figure 6.6: (a) Gouttes de 75% H_2O - 25% glycérol (Panneau A), triéthylène glycol (Panneau B) et 20% H_2O - 80 %glycérol (Panneau C), tournantes dans un reservoir de glycérol pur. Noter les différents facteurs d'agrandissement dans les directions horizontale et verticale. (b) Tension interfaciale effective entre mélanges d'eau et glycérol et glycérol pur par contre la concentration d'eau dans le mélange. La ligne noire est calculée suivant le le modèle de champ de phase proposé dans [7].

mélange d'eau et de glycérol, avec des fractions massiques d'eau $c_w = 0,75$ et $c_w = 0,2$, respectivement. La goutte dans le panneau B, en revanche, est composée de triéthylène glycol (TEG). Toutes les gouttes tournent dans du glycérol pur, avec lequel elles sont entièrement miscibles. La Figure 6.6a montre également que cette forme *"dumbbell"* ne dépend pas seulement de la densité et du contraste de viscosité entre la goutte et le fluide porteur. Si tel était le cas, la goutte du TEG dans le panneau B aurait en effet une forme intermédiaire entre les gouttes dans les panneaux A et C constituées de mélanges d'eau et de glycérol, puisqu'elle a une densité et une viscosité intermdiaires. Ce n'est clairement pas le cas. Donc, la Fig. 6.6a ne peut pas être expliquée entièrement par des phénomènes hydrodynamiques. Le développement d'une forme de os de chien doit donc dépendre de la structure moléculaire des fluides, et par conséquence des contraintes interfaciales résultant de différentes interactions moléculaires. L'étude de l'origine et de la dynamique temporelle de ces formes apparaît naturellement comme une stratégie valable pour étudier la tension interfaciale effective entre la goutte et le fluide porteur. Celle-ci est la stratégie que nous avons adoptée dans la deuxième partie de nos travaux, dans le Chapitre 3.

Nous avons étudié l'origine de telles formes, en montrant que le mouvement de recirculation du fluide porteur pendant la rotation induit une contrainte normale déséquilibrée sur la goutte. Cette contrainte, plus grand au centre de la goutte qu'à la tête, est à l'origine de la forme de l'os du chien. Nous avons étudié l'évolution temporelle de cette forme, en démontrant qu'elle peut être utilisée pour mesurer la tension interfaciale à l'interface entre

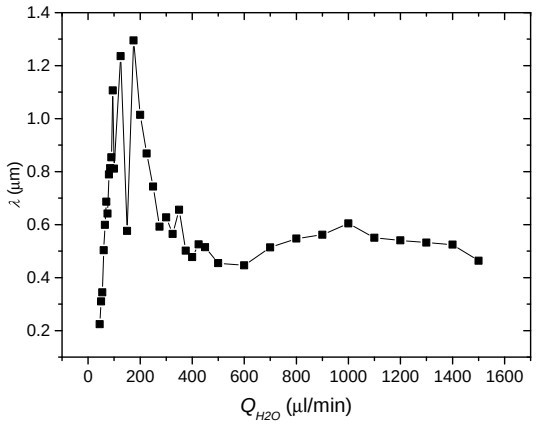

Figure 6.7: Longueur d'onde de l'instabilité d'écoulement parallèle en fonction du débit de l'eau, pour l'eau s'écoulant parallèlement au glycérol dans un canal de 1 mm de largeur. Le débit du glycérol est $Q_{gly} = 12\,\mu\text{L/min}$.

la goutte et le fluide porteur. En développant un modèle simple dans lequel nous équilibrons la contrainte normale imposée sur la surface de la goutte, la contrainte de cisaillement qui s'oppose à la déformation et un terme de type Laplace contenant la tension de surface, nous avons exploité la dynamique de déformation des gouttes miscibles pour mesurer l'EIT entre l'eau et le glycérol comme modèle pour les liquides miscibles simples [30]. En particulier, nous avons trouvé une valeur de EIT de $250 \pm 50\,\text{nN/m}$ pour l'eau pure en contact avec le glycérol pur (Fig. 6.6b), bien inférieur aux limites expérimentales des techniques de tensiométrie plus conventionnelles, et en excellent accord avec le modèle de champ de phase proposé par Truzzolillo et collaborateurs [7]. Par conséquent, nos travaux proposent une méthode de mesure des valeurs extrêmement faibles des tensions interfacelles, particuliérement adaptée pour mesurer l'EIT entre les fluides miscibles [30].

Bien que la tensiométrie à goutte tournante ait été initialement conçue pour les gouttes liquides, cette technique a été utilisée pour mesurer aussi les propriétés d'autres systèmes, tels que l'élasticité des capsules minces [59] et les propriétés viscoélastiques des polymères [39, 41]. Nous avons donc pu employer l'SDT pour mesurer le module élastique et la tension interfaciale des sphères élastiques souples. Les techniques classiques reposent sur la mesure de la longueur élasto-capillaire, c'est à dire le rapport entre l'énergie interfaciale par unité de surface et le module élastique. Par conséquent, ces techniques ne permettent pas de découpler les apports en volume et en surface à la deformation. D'autre part, l'SDT fournit un moyen d'accéder de manière indépendante à la fois au module de cisaillement et à l'énergie de surface des solides mous, en permettant donc une mesure simultanée des deux paramètres [31].

Enfin, comme nous avons discuté dans le Chapitre 1, la controverse des données de littérature sur l'EIT [27–29] découle de la plèthore de diverses techniques expérimentales appliquées et des résultats différents qu'elles donnent, et il n'est pas clair dans quelles

conditions les stress de Korteweg se comportent comme une tension interfaciale d'équilibre. Par conséquent, il ne suffit pas d'étudier ce sujet seulement au moyen de la SDT. Ainsi, nous avons introduit l'étude de l'instabilité des écoulements stratifiés en viscosité comme seconde façon de caractériser l'EIT. Même si d'autres expériences et analyses sont nécessaires pour démêler l'influence de la tension interfaciale sur ces flux instables, nous avons présenté dans la Sec. 5.3 l'étude préliminaire de l'instabilité d'écoulement parallèle. Deux régimes différents sont observés, car la longueur d'onde d'instabilité varie d'une façon non monotone par rapport aux débits. À des débits faibles ou modérés, l'interaction entre l'interface et les parois du canal entraîne un effet de confinement empêchant l'excitation des ondes de grande amplitude et longueur donde. Aux débits plus élevés, l'amplitude de la perturbation atteint une valeur constante et des effets non linéaires doivent être pris en compte. Nous avons montré que pour comprendre la stabilité des flux stratifiés en viscosité, il faut tenir compte à la fois de la dissipation d'énergie cinétique et de sa production, notamment en tenant compte de la forme du profil de vitesse d'écoulement de base. Des autres etudes seront effectués pour mieux comprendre cette instabilité et la possibilité de l'exploiter comme technique de mesure de l'EIT.

En conclusion, nous avons proposé une nouvelle méthode pour mesurer les tensions interfaciales extrêmement faibles et en particulier l'EIT, en ouvrent la voie à une compréhension approfondie des contraintes Korteweg et des phénomènes capillaires dans les fluides miscibles.

In this work we tackle the challenging task of investigating the effective interfacial tension (EIT) between molecular miscible fluids. We first investigate the dynamics of spinning drops when they are subject to a sudden rotation speed jump. Immiscible drops show an exponential decay towards their equilibrium shape, with a characteristic time entirely determined by the viscosities of the two fluids, the drop size and the interfacial tension. Contrarily, a completely different elongation dynamics is found for miscible drops with a small difference in concentration with respect to the background fluid: in this case the dynamics are well captured by a power law. Moreover, for sufficiently low interfacial tension drops deform radially developing a “dumbbell" shape, consisting in a thin central body connecting two larger heads. We investigate the origin of such shapes, and demonstrate that they can be used to measure the interfacial tension at the boundary between the drop and the background fluids. By developing a simple model in which we balance the normal stress imposed on the drop surface, the shear stress opposing the deformation and a Laplace-like term containing the surface tension, we exploit the deformation dynamics of miscible drops to measure the EIT between water and glycerol as a model for simple miscible liquids. In particular, we find an EIT of 250±50 nN/m for pure water in contact with pure glycerol, a value orders of magnitude lower than the experimental limits of more conventional tensiometry techniques. In this thesis we also explore for the first time the systematic use of spinning drop tensiometry to measure the elastic modulus and interfacial tension of soft elastic beads, showing that this technique allows for the simultaneous measurement of the two quantities. Finally, we investigate the stability of viscosity-stratified coflows as a second route to study the EIT. Two different regimes are observed, as the instability wavelength varies non monotonically with respect to the flow rates. At small to moderate flow rates, the interplay between the interface and the channel walls leads to a confinement effect preventing the excitation of big waves. At higher values of flow rate, the amplitude of the disturbance reaches a steady value. We show that, to understand the stability of viscosity-stratified flows one needs to take into account both kinetic energy dissipation and production, notably considering the shape of the base flow velocity profile.

Dans cette thèse nous proposons un travail expérimental visant à comprendre et mesurer la tension interfaciale effective (EIT) entre liquides moléculaires miscibles. Nous étudions d’abord la dynamique des gouttes en rotation lorsqu’elles sont soumises à un saut brusque de vitesse de rotation. Les gouttes immiscibles présentent une décroissance exponentielle vers leur forme d’équilibre, avec un temps caractéristique entièrement déterminé par les viscosités des deux fluides, la taille de la goutte et la tension interfaciale. Au contraire, une dynamique d’allongement complètement différente caractérise les gouttes miscibles avec une petite différence de concentration par rapport au fluide porteur: dans ce cas, la dynamique est bien saisie par une loi de puissance. De plus, pour une tension interfaciale suffisamment faible, les gouttes se déforment radialement en développant une forme "dumbbell", consistant en un corps central mince reliant deux têtes plus grandes. Nous étudions l’origine de ces formes et démontrons qu’elles peuvent être utilisées pour mesurer la tension interfaciale à la frontière entre la goutte et le fluide porteur. En développant un modèle simple dans lequel nous équilibrons la contrainte normale imposée sur la surface de la goutte, la contrainte de cisaillement opposée à la déformation et un terme de type Laplace contenant la tension de surface, nous exploitons la dynamique de déformation des gouttes miscibles pour mesurer l’EIT entre l’eau et le glycérol comme modèle pour les liquides miscibles simples. En particulier, nous trouvons une EIT de 250±50 nN/m pour l’eau pure en contact avec le glycérol pur, un ordre de grandeur inférieur aux limites expérimentales des techniques de tensiométrie plus conventionnelles. Dans cette thèse, nous explorons également pour la première fois l’utilisation systématique de la tensiométrie à goutte tournante pour mesurer le module élastique et la tension interfaciale des billes élastiques souples, montrant que cette technique permet la mesure simultanée des deux quantités. Enfin, nous étudions la stabilité des "coflows" stratifiés en viscosité comme deuxième voie d’étude de l’EIT. Deux régimes différents sont observés, car la longueur d’onde d’instabilité varie d’une façon non monotone par rapport aux débits. À des débits faibles où modérés, l’interaction entre l’interface et les parois du canal entraîne un effet de confinement empêchant l’excitation des ondes de grande amplitude. À des valeurs de débit plus élevées, l’amplitude de la perturbation atteint une valeur constante. Nous montrons que, pour comprendre la stabilité des flux stratifiés en viscosité, il faut tenir compte à la fois de la dissipation et de la production d’énergie cinétique, notamment en considérant la forme du profil de vitesse d’écoulement de base.